TUDelft

Delft University of Technology

Application of Metal-Organic Frameworks in the Production of Radionuclides

Ma, C.

DOI
10.4233/uuid:1daaaf5f-18a4-4ab5-b067-f68a4d0ab330

Publication date
2022

Document Version
Final published version

Citation (APA)
Ma, C. (2022). *Application of Metal-Organic Frameworks in the Production of Radionuclides*. [Dissertation (TU Delft), Delft University of Technology]. https://doi.org/10.4233/uuid:1daaaf5f-18a4-4ab5-b067-f68a4d0ab330

Important note
To cite this publication, please use the final published version (if applicable).
Please check the document version above.

Application of Metal-Organic Frameworks in the Production of Radionuclides

Dissertation

For the purpose of obtaining the degree of doctor
at Technology University of Delft
by the authority of the Rector Magnificus prof. dr. ir. T.H.J.J. van der Hagen
chair of the Board for Doctorates
to be defended publicly on Thursday 20th of October 2022 at 10:00 am

by

Chao Ma

Master of Engineering in Materials Science, Zhengzhou University, China
Born in Sanmenxia City, China

This dissertation has been approved by the promotors:

Composition of the doctoral committee:

Rector Magnificus	Chairman
Dr. ir. A. G. Denkova	Delft University of Technology, promotor
Prof. dr. H. T. Wolterbeek	Delft University of Technology, promotor
Dr. P. Serra Crespo	Delft University of Technology, copromotor

Independent members:

Dr. K. Djanashvili	Delft University of Technology, the Netherlands
Dr. ir. M. Rohde	Delft University of Technology, the Netherlands
Prof. dr. ir. J.R. van Ommen	Delft University of Technology, the Netherlands
Prof. dr. A. Türler	University of Bern, Switzerland
Prof. dr. ir. J. L. Kloosterman	Delft University of Technology, the Netherland, reserve

Printed in the Netherlands

Dedicated to my family

CONTENTS

Introduction

1

1.1 Radionuclides in Nuclear Medicine

Radionuclides play an important role in nuclear medicine for disease diagnosis and treatment [1, 2]. Radionuclides that emit alpha, beta minus particles or Auger electrons are suitable for therapeutic application and are typically coupled to a targeting vector to ensure that they are delivered specifically to disease sites. Many examples of therapeutic radionuclides for internal radiotherapy can be given such as: ^{32}P, ^{64}Cu, ^{67}Ga, ^{86}Y, ^{89}Sr, ^{90}Y, ^{103}Pd, ^{111}In, ^{125}I, ^{131}I, ^{169}Yb, ^{177}Lu, ^{188}Re, ^{211}At, ^{225}Ac and so on [3-6]. In contrast, for diagnostic applications, radionuclides that emit gamma-rays or positrons are commonly selected for imaging to find the location of a lesion or assess the disease progress. There are mainly two imaging modalities including position emission tomography (PET) and single-photon emission computed tomography (SPECT) [7]. In PET (Fig. 1.1 (a)) [8], radionuclides (^{11}C, ^{13}N, ^{15}O, ^{18}F, ^{68}Ga, ^{82}Rb) that emit positrons are used for diagnostics. The emitted positrons interact with electrons, resulting in annihilation and generating a pair of 511 keV gamma photons, which will move in the opposite direction and can be captured by detectors used in PET. In SPECT (Fig. 1.1 (b)) [9], radiopharmaceuticals based on gamma-emitting isotopes (^{67}Ga, ^{99m}Tc, ^{111}In, ^{123}I, ^{201}Tl) are administered to cancer patients and the emitted gamma-ray can be detected by gamma cameras.

Fig. 1.1. Medical diagnostic tests using (a) positron emission tomography (PET) and single-photon emission computed tomography facilities (SPECT)

Nowadays, different kinds of radionuclides are produced using nuclear reactors, generators and accelerators [1]. For an application in diagnostics and radionuclide therapy, the volume of injected radiopharmaceuticals is limited and its activity dose is always controlled in 1 ml solution. Furthermore, the production of radionuclides with high specific activity is usually

essential. Although many of the production routes are well established, there are new ones being developed to solve issues of availability or specific activity. This dissertation focuses on the production of ^{99m}Tc and ^{51}Cr using novel materials, i.e., metal-organic framework (MOFs) materials.

1.2 Properties of ^{99m}Tc and ^{51}Cr

1.2.1. Properties of ^{99m}Tc and ^{99}Mo/^{99m}Tc generator

^{99m}Tc is one of the most important radionuclides as it is used in more than 80% of diagnostic nuclear imaging procedures accounting for the diagnosis of 30~40 million patients every year [10]. The wide applicability of this radioisotope is due to its favorable nuclear and chemical characteristics:[11-14]

(a) The half-life (6 h) ensures that there is enough time to complete testing minimizing the patient's exposure to radiation.

(b) ^{99m}Tc emitting low energy gamma-ray (140 KeV) can be easily detected.

(c) SPECT using ^{99m}Tc results in good spatial resolution and high detection efficiency. The low gamma energy can be easily shielded to protect patients.

(d) ^{99m}Tc possesses several chemical valence states that allow for the formation of diverse compounds, increasing application possibilities.

(e) There exists a ^{99}Mo/^{99m}Tc generator that provides onsite and on-demand ^{99m}Tc.

In the past few decades, many ^{99m}Tc radiopharmaceuticals have been developed and applied in various diagnostic tests (Table 1.1). Therefore, a stable and convent supply of ^{99m}Tc is critical to guarantee the diagnosis of SPECT imaging. ^{99m}Tc is currently supplied by ^{99}Mo/^{99m}Tc generators in hospitals. The decay scheme of ^{99}Mo mother nuclide is exhibited in Fig. 1.2. About 88% ^{99}Mo decays to the metastable ^{99m}Tc with a half-life of 6.01 h and around 12% ^{99}Mo decays to ling-lived ^{99}Tc by emitting a beta minus particle. ^{99m}Tc decays to ^{99}Tc ($t_{1/2}$=21100 years) by isomeric transition emitting 140.5 keV gamma in the process. Finally, ^{99}Tc decays to stable ^{99}Ru through beta minus decay. In the ^{99}Mo/^{99m}Tc generator system, the daughter radionuclide (^{99m}Tc) can be formed at a certain rate, which is determined by the relative half-life relationship between parent and daughter radionuclides. When the decay rate of the mother radionuclide (^{99}Mo) is equal to the production rate of the daughter

radionuclide (^{99m}Tc), transient equilibrium is reached. The following equation can be used to calculate the number of atoms of daughter radionuclides formed at any time of the decay.

$$N_2 = \frac{\lambda_1}{\lambda_2 - \lambda_1} N_1^0 \left(e^{-\lambda_1 t} - e^{-\lambda_2 t}\right) + N_2^0 e^{-\lambda_2 t} \tag{1}$$

Where N_1^0 and N_2^0 represent the number of atoms of parent and daughter radionuclides when t=0, respectively. N_2 is the number of atoms of daughter at time 't'. λ_1 and λ_2 are the decay constant of parent and daughter, respectively.

Table 1.1. Technetium-based radiopharmaceuticals and their application [15].

| Commercial name	Imaging procedure
^{99m}Tc-medronate (MDP)	Bone scan
^{99m}Tc-albumin Aggregated (MAA)	Lung perfusion
^{99m}Tc-pentetate (DTPA)	Kidney scan and function
^{99m}Tc-sestamibi	Cardiac perfusion
^{99m}Tc-exametazime	Brain perfusion
^{99m}Tc-mebrofenin	Fall bladder function
^{99m}Tc-etidronate	Bone scan
^{99m}Tc-disofenin	Fall bladder function
^{99m}Tc-succimer (DMSA)	Kidney scan and function
^{99m}Tc-tetrofosmin	Cardiac perfusion
^{99m}Tc-bicisate	Brain perfusion
^{99m}Tc-red blood cell	Blood pool imaging
^{99m}Tc-lidofenin	Gall bladder function
^{99m}Tc-mertiatide (MAG3)	Kidney scan and function
^{99m}Tc-oxidronate (HDP)	Bone scan
^{99m}Tc-sodium pertechnetate	Thyroid, salivary gland, Meckel's scan
^{99m}Tc-sulfur colloid	Liver scan, sentinel lymph node localization
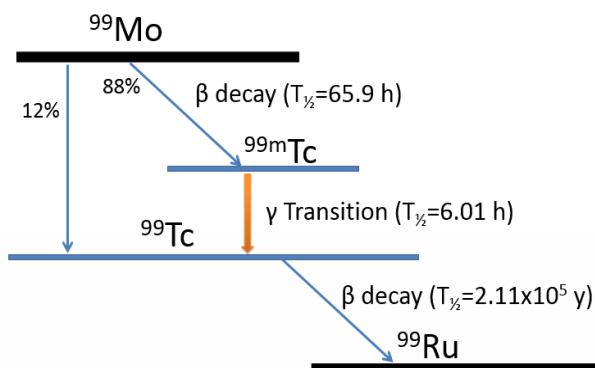
Fig. 1.2. The decay scheme of Mo-99 to stable Ru-99

1.2.2 Properties of ^{51}Cr and Szilard-Chalmers effect

Chromium-51 (^{51}Cr) is an attractive medical radioisotope as it can combine with hemoglobin, forming a stable compound [16]. It is commonly used for radiolabeling of red blood cells in order to determine the mass and volume of blood in patients [17, 18]. Additionally, this radionuclide is suitable for radiolabeling of platelets to determine their survival time and for detecting bleeding in gastrointestinal diseases [19]. Fig. 1.3 shows the ^{51}Cr decay scheme. ^{51}Cr has a half-life of 27.7 days. 90% of ^{51}Cr can decay directly to the ground state of ^{51}V by electron capture. The other 10% of ^{51}Cr decays to an excited state by electron capture and then further to the ground state emitting a gamma-ray of 320 keV.
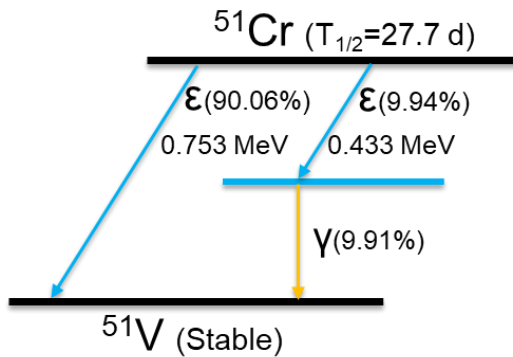
^{51}**Cr** ($T_{1/2}$=27.7 d)

ε(90.06%) ε(9.94%)
0.753 MeV   0.433 MeV

γ(9.91%)

^{51}**V** (Stable)

Fig. 1.3. The decay scheme of ^{51}Cr to stable ^{51}V

To meet the requirements for applications in nuclear medicine, ^{51}Cr having specific activity of 50 Ci/g is needed [20]. ^{51}Cr can be produced by neutron activation in nuclear reactors. However, the natural abundance of ^{50}Cr is only about 4.4% and its neutron capture cross-section is 16 barns. To produce ^{51}Cr with high specific activity, ^{50}Cr enriched targets can be irradiated by neutrons, but this direct production method can only provide a low enrichment factor (~23), which means that the percentage of chromium in the irradiation targets is 23 times higher than that of using natural chromium target [21].

The so-called Szilard-Chalmers effect is an alternative method to produce high-specific activity radionuclides. In 1934, L. Szilard and T. Chalmers reported that ^{125}I could be enriched based on chemical effects and nuclear transformation [22]. The recoil energy received by an atom emitting prompt gammas upon neutron capture can be high enough to break the chemical bond between the produced radionuclide and the stable irradiated isotope.

In such cases, the target radionuclide can be separated from the stable isotope, resulting in radionuclides of high specific activity. The recoil energy of the produced radionuclide can be determined by the following equation:

$$E_r = 537 * \frac{E_\gamma{}^2}{M}$$

Where E_r is the recoil energy in eV and E_γ is the average energy of the prompt gamma rays in MeV. M is the mass of the recoiling atom in amu. The desired radionuclide can be separated and enriched when its recoil energy is notably higher than the energy of the chemical bonds which it was originally bonded to.

1.3 Current production of ^{99}Mo/^{99m}Tc and ^{51}Cr

1.3.1   Current production of ^{99}Mo and ^{99m}Tc

To guarantee a stable supply of ^{99m}Tc for the global market, the production of ^{99}Mo, the mother nuclide, is extremely important. In 2015, it was estimated by Nuclear Energy Agency (NEA) that the worldwide demand for ^{99}Mo was about 9000 Ci/week. The demand for ^{99}Mo appears to increase at a rate of 0.5 % and 5 % per year for mature markets and developing markets, respectively [23]. Nowadays, there are mainly three production pathways, including fission of uranium (^{235}U), accelerator routes using photon reactions on ^{100}Mo and neutron activation of ^{98}Mo. Their pros and cons are discussed below.

Fission

In 2017, the majority of ^{99}Mo used in nuclear medicine was produced by the fission of high enriched uranium (HEU, ^{235}U content>20 %) producing ^{99}Mo of very high specific activity. The ^{99}Mo supplied for the global market was mainly produced by the HFR, Netherlands (stated in 1961, 6200 Ci/week), BR-2, Belgium (started in 1961, 7800 Ci/week), SAFARI, South Africa (started in 1965, 3000 Ci/week), Maria, Poland (started in 1974, 2700 Ci/week), LVR-15, Czech Republic (started in 1989, 3000 Ci/week) and OPAL, Australia (started in 2007, 2150 Ci/week) [26]. There are also some other reactors that can produce smaller amounts of ^{99}Mo, such as RBT-6/RBT-10a and WWR-c in Russia and RA-3 in Argentina. However, there are several disadvantages of this route. First, many of the large reactors are more than 40 years old and need to be maintained regularly. Unscheduled shutdowns of the

old reactors have become more frequent and tend to take longer to be back in operation, which caused ^{99}Mo supply shortage. For example, the HFR reactor was shut down due to leaking in the cooling system and the NRU (National Research Universal, Canada) reactor was shut down for 1 year in 2009 due to a vessel leak [24]. Second, the production yield of ^{99}Mo is only about 6.1% while most of the other radionuclides are simply nuclear waste. Furthermore, this production process is not sustainable as the targets cannot be recycled. Third, the ^{99}Mo production using HEU is considered a potential nuclear proliferation risk. Nowadays, to sustain long-term development, most reactors have achieved a transition to utilize low energy uranium for ^{99}Mo production (LEU, ^{235}U content≤20 %) [25], as shown in Fig. 1.4.
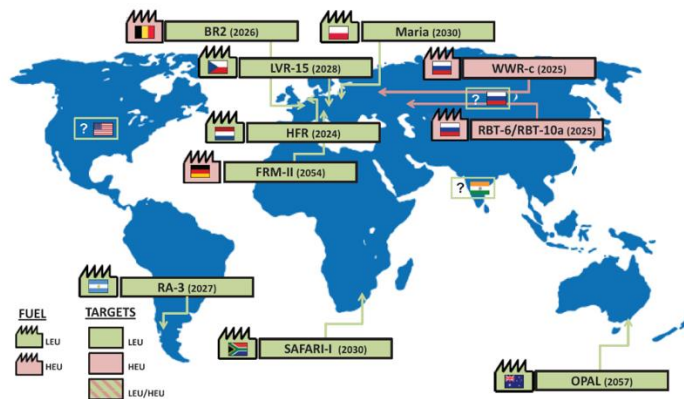
Fig. 1.4. Speculative map of the ^{99}Mo supply in 2020. Russia's reactors will continue using HEU, but other reactors begin to produce ^{99}Mo using non-HEU sources [26].

Accelerator/ Cyclotron

Other alternative methods to produce ^{99}Mo and ^{99m}Tc are using linear accelerators or cyclotrons. For the cyclotron accelerator, charged particles are accelerated by an alternating voltage with high frequency in two semicircular electrodes. In a linear accelerator, electrons are accelerated using a high amplitude AC voltage in a straight line. Different targets can be bombarded using specific particles to produce ^{99}Mo or ^{99m}Tc. Nowadays, more and more facilities are built to produce ^{99}Mo as summarized in Fig. 1.5. Many of these routes generate much less nuclear waste. However, many of these production routes require large investments because of the expensive facilities and limited efficiency during production. For all these routes, the photon reaction of ^{100}Mo is the most promising but results in low specific activity

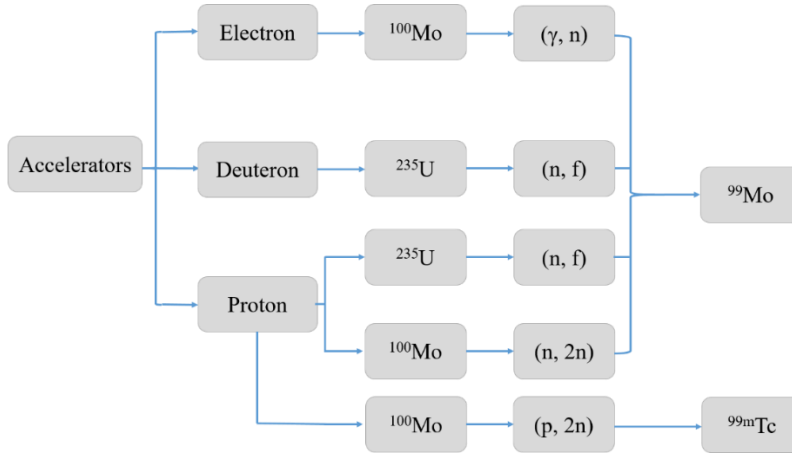^{99}Mo (maximum of 100 Ci/g).

Fig. 1.5. Reaction diagram for the production of ^{99}Mo and ^{99m}Tc based on accelerator-driven processes (electron, deuteron and proton can be used as projectiles for different nuclear reactions) [27]

Neutron activation

Another route to produce ^{99}Mo is the neutron activation of ^{98}Mo written as ^{98}Mo(n, γ)^{99}Mo. For this production process, enriched ^{98}Mo (>99%) should be selected as the irradiation target and bombarded by thermal or epithermal neutron flux to generate radioactive ^{99}Mo accompanied by the emission of prompt gammas. This production route has several distinctive advantages: (1) The production does not need to use ^{235}U targets; (2) It will not generate additional nuclear waste; (3) A recyclable system can be built to reuse the non-radioactive molybdenum; (4) More than 200 reactors worldwide can be used to produce ^{99}Mo, which eliminates the geographic restriction; (5) The separation system is more straightforward compared with the fission produced ^{99}Mo.

However, when the enriched ^{98}Mo target is irradiated for 8 days in a reactor with the thermal neutron flux of 1×10^{14} n·cm^{-2}·s^{-1}, the specific activity of neutron-produced ^{99}Mo is much lower (4 orders of magnitude) than that of fission ^{99}Mo. The activity of neutron-produced ^{99}Mo is determined by the neutron flux, reaction cross-section and the mass of the targets. The production equation is depicted as:

$$A_{Mo-99} = \varphi \sigma N_{Mo-98}(1 - e^{-\lambda t})$$

Where φ is neutron flux (n·cm^{-2}·s^{-1}), σ is cross-section (barn), N_{Mo-98} is the amount of irradiated ^{98}Mo and λ is the decay constant of ^{99}Mo. The specific activity of produced molybdenum can be determined by:

$$A_{sa}=A_{Mo-99}/m$$

In the thermal region, the cross-section of ^{98}Mo is 0.13 barn, while the maximum cross-section of ^{98}Mo is 0.7 barn resonance in the epithermal region. But the integrated cross-section is relatively low in the epithermal region. Therefore, the neutron-produced ^{99}Mo has a relatively low specific activity, which makes that ^{99}Mo produced by neutron activation cannot be implemented in current commercial generators.

1.3.2 Current ^{51}Cr production

Over the past few decades, two methods referring to ^{51}Cr production for nuclear medicine have been reported. Two main production methods are used to supply commercially ^{51}Cr. One route is the direct neutron irradiation using an enriched chromium target to produce ^{51}Cr, i.e. ^{50}Cr(n, γ)^{51}Cr reaction. The other one is based on the Szilard-Chalmers effect and applied when using different compounds of chromium. If the same mass sample, neutron flux and irradiation time are used, the alternative production route of the Szilard-Chalmers reaction can obtain higher enrichment factor. For example, potassium chromate as a target was irradiated for 66 h and H_2SO_4 as an extraction agent was employed by Harbottle et al. resulting in the ^{51}Cr with a specific activity of 40 mCi/mg and an enrichment factor of 680 [28]. Vimalnath et al. investigated the large-scale production of ^{51}Cr using the Szilard-Chalmers effect and the same target, and managed to obtain specific activity of 150 mCi/mg after 7 days of irradiation [29]. These papers proved that high specific activity of ^{51}Cr could be achieved using potassium chromate as the radiation target based on the Szilard-Chalmers effect. However, the extraction procedures they used were very complex and introduced other impurities. Therefore, we propose a new production route using chromium-based metal-organic frameworks as radiation targets to produce ^{51}Cr with high specific activity based on the Szilard-Chalmers effect. More details about metal-organic frameworks are discussed in section 1.4.

1.4 Metal-Organic Frameworks

Metal-organic frameworks (MOFs) are an emerging class of ordered porous materials, which consist of metal nodes/clusters and organic linkers connected by coordination bonds, as shown in Fig. 1.6 (a). Over 90000 MOFs with different topologies and compositions have been researched in the past few decades. MOFs have become one of the most attractive and compelling materials, and have great potential in many applications, including catalysis, drug delivery, sensing, fuel cells, adsorption and separation [30-41], because of their high surface area, tunable pore size, easy functionality and fantastic coordination (Fig. 1.6 (b)). These properties provide outstanding adsorption and separation performance, including adsorption capacity, adsorption kinetics, selectivity and stability [33, 42-45]. However, most MOFs have worse stability compared with traditional adsorbent materials such as activated carbon, mesoporous silica, graphene and nano metal oxides [46-49]. Therefore, several MOF candidates, which have excellent chemical, thermal and radiation stability, are selected and their potential used for radioisotope production is investigated in this research.

1.4.1 Application of MOFs for the ^{99}Mo/^{99m}Tc generator

As mentioned before, the most promising alternative ^{99}Mo production methods (^{98}Mo(n, γ)^{99}Mo and ^{100}Mo(γ, n)^{99}Mo) produce ^{99}Mo with low specific activity ranging from 1 to 10 Ci/g, which is much lower than the one produced by fission ^{99}Mo (~50000Ci/g, The OPAL reactor) [50]. To prepare a ^{99}Mo/^{99m}Tc generator having the same total activity (1~4 Ci) as a commercial generator, adsorbents with higher adsorption capacity should be developed so that low specific activity of ^{99}Mo can be utilized in nuclear medicine.

In the past few decades, many kinds of adsorbents were investigated for ^{99}Mo/^{99m}Tc separation. Those adsorbents can be classified into three categories: bulk metal oxides, gels and nanomaterials. Their molybdenum adsorption capacity was certainly improved compared with that of commercial alumina used in clinical generators (2~20 mg/g), as shown in Table 1.2. To improve molybdenum adsorption capacity, nanomaterial-based and functional adsorbents with high surface area and big pore sizes were developed. Although some adsorbents showed good adsorption properties, the required adsorption capacity still has not been achieved so far. Therefore, the utilization of MOFs as molybdenum adsorbents for the ^{99}Mo/^{99m}Tc generator was explored due to their extremely high surface area, tunable porosity
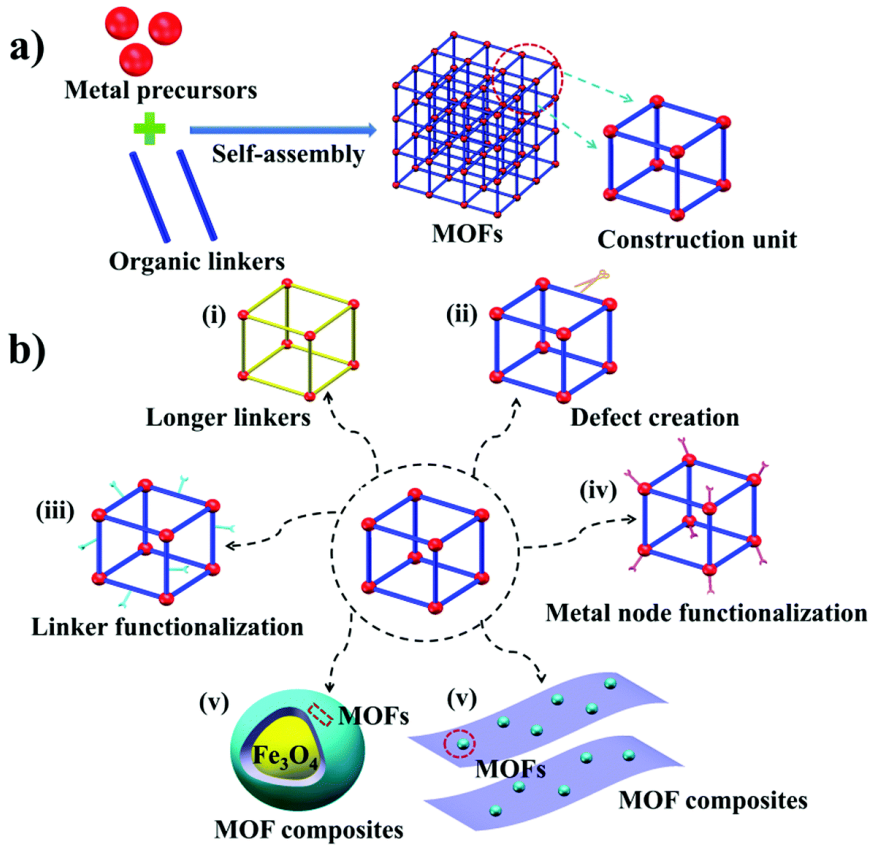
and easy functionalization.

Fig. 1.6. Schematic representation of MOFs. (a) MOFs are constructed by metal clusters and organic linkers (b) strategies for modification of MOFs and composites. (i) MOFs having longer linkers; (ii) MOFs with defects; (iii and iv) functionalized MOFs; (v) MOFs with core-shell structure or layered structure [44].

Table 1.2. Summary of the molybdenum adsorption capacity of different adsorbents.

Adsorbents	Mo adsorption capacity (mg/g)	Surface area (m²/g)	Ref.
TUD-1	112	402	[51]
Hydrous MnO_2	50	--	[52]
TiO_2	100	30	[53]
Hydrous TiO_2	230	--	[54]
Al-dropped mesoporous SiO_2	16.8	463	[55]
Gibbsite-Al_2O_3	67.5	--	[55]
Sulfated Al_2O_3	392	--	[56]
Activated alumina	23.5	--	[57]
Meso-Al_2O_3	225	230	[58]
Mesoporous Al_2O_3	31	--	[59]
Mesoporous Al_2O_3	250	542	[60]
Mesoporous γ-Al_2O_3	56.2	251	[61]
Nanocrystalline γ-Al_2O_3	200	252	[62]
$Al^{99}Mo$ gel	364	--	[63]
t-ZrO_2	250	340	[64]
PZC	285	--	[65]
Zirconium polymers PZC	200	--	[66]
Zirconium-based material	177	--	[67]
Hydrotalcite	140	--	[68]
Al_2O_3-sulfated-zirconia	270	--	[69]
Poly nano-cerium chloride	195	--	[70]
Cerium molybdate gel	53	--	[71]
ZrMoSi gel	2.88	--	[72]
Silica–zirconia inorganic polymer	450	140	[73]

1.4.2   Application of MOFs for ^{51}Cr production

Applications such as red blood cell labeling, spleen scintigraphy and diagnosis of gastrointestinal bleeding require ^{51}Cr with high specific activity (50 Ci/g) [74, 75]. Several papers studied the preparation of high specific activity ^{51}Cr by the Szilard-Chalmers effect but utilized complex separation methods (cation exchange or chemical co-precipitation). In this study, chromium-based MOFs were researched to prepare ^{51}Cr with high specific activity using an uncomplicated solid-liquid separation method. MIL-100 (100) and MIL-101 (Cr) (MIL stands for Material of Institute Lavoisier) are two typical MOFs and have great potential for applications including removal of toxic substances, nuclear waste treatment, gas storage and drug delivery due to their high pore volume and excellent chemical stability [76-

78]. MIL-100 (Cr) is built by tri-carboxylate linkers and trimers of chromium (III) oxide octahedra, forming two types of mesoporous cages with a diameter of 25 Å and 29 Å, as shown in Fig. 1.7. While MIL-101 (Cr) consists of the chromium trimers and di-carboxylate linkers exhibiting mesoporous cages with bigger sizes (29 Å and 34 Å). However, their radiation stability and their use in radionuclide production have not been reported so far. Therefore, their radiation stability was also investigated in addition to studying their potential in radionuclides production.
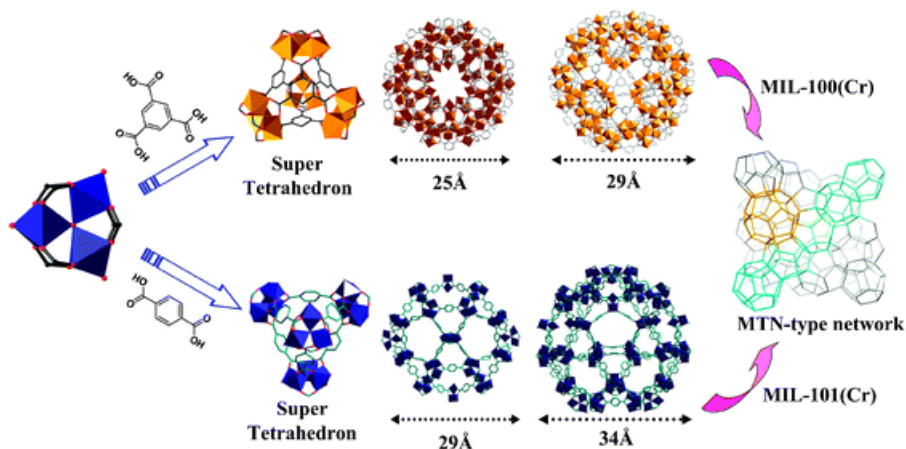
Fig. 1.7. Structural composition diagram of MIL-100 (Cr) and MIL-101 (Cr) [79].

1.5 Research objectives and outline of thesis

1.5.1   Research objectives

This dissertation explored the utilization potential of MOFs in the production of radionuclides. The goals of this thesis were as follows:

- ✓ Development of high molybdenum capacity adsorbents that also have excellent ^{99m}Tc elution with low molybdenum breakthrough.
- ✓ Understanding the interaction between the adsorbed species (molybdenum oxyanions) and the adsorbent.
- ✓ Designing a radionuclide generator based on the best adsorbent found during this research and achieving a performance that can fulfill the European Pharmacopeia standards.

- ✓ Studying the radiation stability of some MOFs that were researched in this thesis.
- ✓ Producing ^{51}Cr with high specific activity using chromium-based MOFs based on the Szilard-Chalmers method.

1.5.2 Outline of thesis

This thesis focuses on ^{99m}Tc and ^{51}Cr production and can be divided into two sections. In the first section, several MOFs were investigated as potential adsorbents for ^{99}Mo/^{99m}Tc generator, and the interactions between MOFs and molybdenum species were explored. In the second section, the effects of gamma rays on the stability of MOFs were studied, which further provided guidance for the in-depth investigation of MOFs and might prove useful in many other nuclear field applications besides the production of radionuclides. Afterward, two chromium-based MOFs were irradiated to produce ^{51}Cr and the separation was conducted under different conditions.

Chapter 2 investigates the potential of UiO-66 (Zr) and its functionalized derivatives as molybdenum adsorbents for the ^{99}Mo/^{99m}Tc generator. Molybdenum adsorption experiments at different concentrations were carried out and the interactions between molybdenum species and the adsorbents were studied by X-ray photoelectron spectra and density functional theory (DFT) calculations. The UiO-66-Form MOF was then applied in column experiments and finally the elution performance of the prepared ^{99}Mo/^{99m}Tc generator was assessed.

Chapter 3 explores the potential of two mesoporous MOFs (PCN-222 and PCN-224) for their utilization in the ^{99}Mo/^{99m}Tc generator. Based on Chapter 2, we found that MOFs with larger pore sizes could promote the adsorption of large molybdate ions on MOFs. Therefore, the molybdenum adsorption performance of two mesoporous MOFs was studied at different pH and molybdenum concentrations. The adsorption mechanism was investigated by X-ray Photoelectron Spectra and Fourier-Transform Infrared Spectroscopy. Furthermore, two ^{99}Mo/^{99m}Tc generators fabricated with PCN-222 and PCN-224 as adsorbents were prepared and their elution performance was measured using the saline solution at different pH to assess possible clinical applications.

In **chapter 4**, UiO-66 (Ce) as molybdenum adsorbent for ^{99}Mo/^{99m}Tc generator was prepared. Based on Chapters 2 and 3, although the molybdenum adsorption capacity of MOFs was improved enormously, the separation performance was not ideal for the prepared ^{99}Mo/^{99m}Tc

generator when they were used as adsorbents in a column mode. Therefore, the adsorption performance of UiO-66 (Ce) and its interaction with molybdenum species were studied in this chapter. Additionally, a ^{99}Mo/^{99m}Tc generator was fabricated with UiO-66 (Ce) as adsorbent and its elution performance was investigated over two weeks.

Chapter 5 describes the effects of gamma doses on the structural stability of MOFs. To produce high specific activity ^{51}Cr, two chromium-based MOFs (MIL-100 (Cr) and MIL-101 (Cr)) were selected due to their outstanding chemical stability. Meanwhile, to better understand the interaction of radiation with the different MOFs, two other MOFs (MIL-100 (Fe) and AlFu MOF) were also researched which helped to determine the influence of different organic linkers and metal clusters on the radiation stability of MOFs in a systematic way. Their structural evolution was monitored by XRD, SEM, FT-IR, XPS and nitrogen adsorption.

In **Chapter 6**, MIL-100 (Cr) and MIL-101 (Cr) were selected as irradiation targets for ^{51}Cr production. ^{51}Cr with high specific activity was produced by the Szilard-Chalmers method and separated using a solid-liquid extraction method. The optimum extraction conditions including extraction time, pH of solution, chemical reagents and concentration were researched.

Chapter 7 displays the summary of this dissertation and suggestions for future research.

References

[1] S.M. Qaim, The present and future of medical radionuclide production, Radiochim. Acta, 100 (2012) 635-651.

[2] T.I. Kostelnik, C. Orvig, Radioactive Main Group and Rare Earth Metals for Imaging and Therapy, Chem. Rev., 119 (2019) 902-956.

[3] S.M. Qaim, I. Spahn, Development of novel radionuclides for medical applications, J. Labelled Comp. Radiopharm., 61 (2018) 126-140.

[4] S.M. Qaim, Nuclear data for production and medical application of radionuclides: Present status and future needs, Nucl. Med. Biol., 44 (2017) 31-49.

[5] K.P. Willowson, Production of radionuclides for clinical nuclear medicine, Eur. J. Phys., 40 (2019) 043001.

[6] Z. Talip, C. Favaretto, S. Geistlich, N.P.V. Meulen, A Step-by-Step Guide for the Novel Radiometal Production for Medical Applications: Case Studies with ^{68}Ga, [44]Sc, ^{177}Lu and [161]Tb, Molecules, 25 (2020).

[7] S.C. Srivastava, L.F. Mausner, Therapeutic Radionuclides: Production, Physical Characteristics, and Applications, Therapeutic Nuclear Medicine, Springer Berlin Heidelberg, Berlin, Heidelberg, 2013, pp. 11-50.

[8] Positron Emission Tomography (PET), https://lairdthermal.com/applications/positron-emission-tomography.

[9] The Precedence 64-slice in SPECT/CT, 2006, https://www.medgadget.com/2006/09/the_precedence.html.

[10] R. Chakravarty, J. Bahadur, S. Lohar, H.D. Sarma, D. Sen, R. Mishra, S. Chakraborty, A. Dash, Solid state synthesis of mesoporous alumina: A viable strategy for preparation of an advanced nanosorbent for [99]Mo/^{99m}Tc generator technology, Microporous Mesoporous Mater., 287 (2019) 271-279.

[11] S. Liu, Bifunctional coupling agents for radiolabeling of biomolecules and target-specific delivery of metallic radionuclides, Adv. Drug Deliv. Rev., 60 (2008) 1347-1370.

[12] W.C. Eckelman, Unparalleled contribution of technetium-99m to medicine over 5 decades, JACC Cardiovasc Imaging, 2 (2009) 364-368.

[13] G. Bandoli, F. Tisato, A. Dolmella, S. Agostini, Structural overview of technetium compounds (2000–2004), Coord. Chem. Rev., 250 (2006) 561-573.

[14] S. Chattopadhyay, L. Barua, S.S. Das, A. De, U. Kumar, A. Mitra, T. Mallick, Madhusmita, M.A. Nayer, S. Sinha, B.R. Sarkar, S. Ganguly, K. De, M.K. Das, M.G.R. Rajan, Pharmaceutical grade sodium [^{99m}Tc] pertechnetate from low specific activity [99]Mo using an automated [99]Mo/^{99m}Tc-TCM-autosolex generator, J. Radioanal. Nucl. Chem., 302 (2014) 781-790.

[15] D. Papagiannopoulou, Technetium-99m radiochemistry for pharmaceutical applications, J. Labelled Comp. Radiopharm., 60 (2017) 502-520.

[16] S.J. Gray, K.J. Sterling, The tagging of red cells and plasma proteins with radioactive chromium, 29 (1950) 1604-1613.

[17] D.M. Mock, G.L. Lankford, J.A. Widness, L.F. Burmeister, D. Kahn, R.G. Strauss, Measurement of red cell survival using biotin-labeled red cells: validation against ^{51}Cr-labeled red cells, Transfusion, 39 (1999) 156-162.

[18] A. Freud, A. Canfi, E. Ben-Hur, Validity of chromium-51 labeling of human erythrocytes as an assay for their survival after photodynamic therapy in vitro for blood sterilization, Int. J. Radiat. Biol., 63 (1993) 651-653.

[19] H.J. Eyre, P.J. Rosen, S. Perry, Relative Labeling of Leukocytes, Erythrocytes and Platelets in Human Blood by [51]Chromium, Blood, 36 (1970) 250-253.

[20] Rediscover the powder of radiometric detection, (2010).

[21] N. Shibata, K.J. Yoshihara, Preparation of Chromium-51 of a High Specific Activity by the Szilard-Chaimers Process, 32 (1959) 422-423.

[22] L. Szilard, T.A. Chalmers, Chemical separation of the radioactive element from its bombarded isotope in the Fermi effect, Nature, 134 (1934) 462-462.

[23] E. National Academies of Sciences, Medicine, Molybdenum-99 for Medical Imaging, The National Academies Press, Washington, DC, 2016.

[24] E. National Academies of Sciences, Medicine, Molybdenum-99 for medical imaging, National Academies Press, 2016.

[25] M. Ahmad, G. Vandegrift, P.J.T. Cristini, Molybdenum-99 ([99]Mo): Past, Present, and Future, 99 (2013) 99m.

[26] E. National Academies of Sciences, Medicine, Opportunities and approaches for supplying molybdenum-99 and associated medical isotopes to global markets: proceedings of a symposium, (2018).

[27] Feasibility of Producing Molybdenum-99 on a Small Scale Using Fission of Low Enriched Uranium or Neutron Activation of Natural Molybdenum, International Atomic Energy Agency, Vienna, 2015.

[28] G. Harbottle, A.G. Maddock, The Preparation of Chromium-51 of High Specific Activity, 21 (1953) 1686-1687.

[29] K.V. Vimalnath, A. Rajeswari, S. Chakraborty, A. Dash, Large scale production of ^{51}Cr for medical application in a medium flux research reactor: a comparative investigation of Szilard-Chalmers process and direct (n, γ) route, Appl. Radiat. Isot., 91 (2014) 104-108.

[30] A. Dhakshinamoorthy, H. Garcia, Catalysis by metal nanoparticles embedded on metal-organic frameworks, Chem. Soc. Rev., 41 (2012) 5262-5284.

[31] C.Y. Sun, C. Qin, X.L. Wang, Z.M. Su, Metal-organic frameworks as potential drug delivery systems, Expert Opin. Drug Deliv., 10 (2013) 89-101.

[32] J. Canivet, A. Fateeva, Y. Guo, B. Coasne, D. Farrusseng, Water adsorption in MOFs: fundamentals and applications, Chem. Soc. Rev., 43 (2014) 5594-5617.

[33] S. Dhaka, R. Kumar, A. Deep, M.B. Kurade, S.W. Ji, B.H. Jeon, Metal–organic frameworks (MOFs) for the removal of emerging contaminants from aquatic environments, Coord. Chem. Rev., 380 (2019) 330-352.

[34] I. Abánades Lázaro, R.S. Forgan, Application of zirconium MOFs in drug delivery and biomedicine, Coord. Chem. Rev., 380 (2019) 230-259.

[35] C. Wang, J. Kim, V. Malgras, J. Na, J. Lin, J. You, M. Zhang, J. Li, Y. Yamauchi, Metal-Organic Frameworks and Their Derived Materials: Emerging Catalysts for a Sulfate Radicals-Based Advanced Oxidation Process in Water Purification, Small, 15 (2019) e1900744.

[36] W.G. Cui, T.L. Hu, X.H. Bu, Metal-Organic Framework Materials for the Separation and Purification of Light Hydrocarbons, Adv. Mater., 32 (2020) e1806445.

[37] G.R. Xu, Z.H. An, K. Xu, Q. Liu, R. Das, H.L. Zhao, Metal organic framework (MOF)-based micro/nanoscaled materials for heavy metal ions removal: The cutting-edge study on designs, synthesis, and applications, Coord. Chem. Rev., 427 (2021) 213554.

[38] L.E. Kreno, K. Leong, O.K. Farha, M. Allendorf, R.P. Van Duyne, J.T. Hupp, Metal-organic framework materials as chemical sensors, Chem. Rev., 112 (2012) 1105-1125.

[39] B. Liu, Metal-organic framework-based devices: separation and sensors, J. Mater. Chem., 22 (2012) 10094-10101.

[40] H. Kitagawa, Metal-organic frameworks: Transported into fuel cells, Nat. Chem., 1 (2009) 689-690.

[41] X. Wen, Q. Zhang, J. Guan, Applications of metal-organic framework-derived materials in fuel cells and metal-air batteries, Coord. Chem. Rev., 409 (2020) 213214.

[42] S. Rojas, P. Horcajada, Metal-Organic Frameworks for the Removal of Emerging Organic Contaminants in Water, Chem. Rev., 120 (2020) 8378-8415.

[43] Z. Hu, Y. Wang, D. Zhao, The chemistry and applications of hafnium and cerium(iv) metal-organic frameworks, Chem. Soc. Rev., 50 (2021) 4629-4683.

[44] J. Li, X. Wang, G. Zhao, C. Chen, Z. Chai, A. Alsaedi, T. Hayat, X. Wang, Metal-organic framework-based materials: superior adsorbents for the capture of toxic and radioactive metal ions, Chem. Soc. Rev., 47 (2018) 2322-2356.

[45] Y. Bai, Y. Dou, L.H. Xie, W. Rutledge, J.R. Li, H.C. Zhou, Zr-based metal-organic frameworks: design, synthesis, structure, and applications, Chem. Soc. Rev., 45 (2016) 2327-2367.

[46] P. Hadi, M.H. To, C.W. Hui, C.S. Lin, G. McKay, Aqueous mercury adsorption by activated carbons, Water Res., 73 (2015) 37-55.

[47] Y. Sun, S. Yang, Y. Chen, C. Ding, W. Cheng, X. Wang, Adsorption and desorption of U(VI) on functionalized graphene oxides: a combined experimental and theoretical study, Environ. Sci. Technol., 49 (2015) 4255-4262.

[48] X. Tan, Q. Fan, X. Wang, B. Grambow, Eu(III) sorption to TiO_2 (anatase and rutile): batch, XPS, and EXAFS studies, Environ. Sci. Technol., 43 (2009) 3115-3121.

[49] P. Li, J. Wang, X. Li, W. Zhu, S. He, C. Han, Y. Luo, W. Ma, N. Liu, D.D. Dionysiou, Facile synthesis of amino-functional large-size mesoporous silica sphere and its application for Pb^{2+} removal, J. Hazard Mater., 378 (2019) 120664.

[50] V.S. Le, Tc Generator Development: Up-to-Date Tc Recovery Technologies for Increasing the Effectiveness of Mo Utilisation, Sci. Technol. Nucl., 2014 (2014) 1-41.

[51] A.G. Denkova, B.E. Terpstra, O.M. Steinbach, J.t. Dam, H.T. Wolterbeek, Adsorption of Molybdenum on Mesoporous Aluminum Oxides for Potential Application in Nuclear Medicine, Sep. Sci. Technol., 48 (2013) 1331-1338.

[52] J. Serrano Gómez, F. Granados Correa, ^{99m}Tc generator with hydrated MnO_2 as adsorbent of ^{99}Mo, J. Radioanal. Nucl. Chem., 254 (2002) 625-628.

[53] R. Chakravarty, R. Shukla, S. Gandhi, R. Ram, A. Dash, M. Venkatesh, A.K. Tyagi, Polymer embedded nanocrystalline titania sorbent for $^{99}Mo/^{99m}Tc$ generator, J. Nanosci. Nanotechnol., 8 (2008) 4447-4452.

[54] Q.M. Qazi, M. Ahmad, Preparation and evaluation of hydrous titanium oxide as a high affinity adsorbent for molybdenum (^{99}Mo) and its potential for use in ^{99m}Tc generators, in: Radiochimica Acta Int. J., 2011, pp. 231.

[55] Y. Suzuki, T. Kitagawa, Y. Namekawa, M. Matsukura, K. Nishikata, H. Mimura, K. Tsuchiya, Molybdenum Adsorption and Desorption Properties of Alumina with Different Surface Structures for $^{99}Mo/^{99m}Tc$ Generators, Trans. Mater. Res. Soc. Jpn., 43 (2018) 75-80.

[56] J.S. Lee, H.S. Han, U.J. Park, K.J. Son, H.Y. Shin, S.B. Hong, K.D. Jang, J.S. Lee, Adsorbents for radioisotopes, preparation method and radioisotope generators using the same, patent US8758714B2, (2014).

[57] V.S. Skuridin, E.S. Stasyuk, E.A. Nesterov, V.L. Sadkin, A.S. Rogov, A procedure for sorbent pretreatment for the production of high-activity [99]Mo/^{99m}Tc generators based on enriched [98]Mo, Rad. chem., 54 (2012) 391-394.

[58] R. Chakravarty, R. Ram, R. Mishra, D. Sen, S. Mazumder, M.R.A. Pillai, A. Dash, Mesoporous Alumina (MA) Based Double Column Approach for Development of a Clinical Scale [99]Mo/[99m]Tc Generator Using (n, γ)[99]Mo: An Enticing Application of Nanomaterial, Ind. Eng. Chem. Res., 52 (2013) 11673-11684.

[59] I. Saptiama, Y.V. Kaneti, Y. Suzuki, Y. Suzuki, K. Tsuchiya, T. Sakae, K. Takai, N. Fukumitsu, Z.A. Alothman, M.S.A. Hossain, K. Ariga, Y. Yamauchi, Mesoporous Alumina as an Effective Adsorbent for Molybdenum (Mo) toward Instant Production of Radioisotope for Medical Use, Bull. Chem. Soc. Jpn., 90 (2017) 1174-1179.

[60] J. Wang, R. Gao, Q. Huang, X. Yin, M. Lin, S. Cao, D. Chen, F. Fan, X. Wu, Z. Qin, Z. Guo, J. Bai, J. Chu, W. Tian, C. Tan, B. Li, N. Cheng, Z. Jia, Practicality of hierarchically macro/mesoporous gamma-Al_2O_3 as a promising sorbent in the preparation of low specific activity [99]Mo/^{99m}Tc generator, Appl. Radiat. Isot., 178 (2021) 109986.

[61] I. Saptiama, Y.V. Kaneti, Y. Suzuki, K. Tsuchiya, N. Fukumitsu, T. Sakae, J. Kim, Y.M. Kang, K. Ariga, Y. Yamauchi, Template-Free Fabrication of Mesoporous Alumina Nanospheres Using Post-Synthesis Water-Ethanol Treatment of Monodispersed Aluminium Glycerate Nanospheres for Molybdenum Adsorption, Small, 14 (2018) e1800474.

[62] R. Chakravarty, R. Ram, A. Dash, M.R. Pillai, Preparation of clinical-scale [99]Mo/^{99m}Tc column generator using neutron activated low specific activity [99]Mo and nanocrystalline gamma-Al_2O_3 as column matrix, Nucl. Med. Biol., 39 (2012) 916-922.

[63] M. Amin, M.A. El-Amir, H.E. Ramadan, H. El-Said, [99]Mo/^{99m}Tc generators based on aluminum molybdate gel matrix prepared by nano method, J. Radioanal. Nucl. Chem., 318 (2018) 915-922.

[64] R. Chakravarty, R. Shukla, R. Ram, A.K. Tyagi, A. Dash, M. Venkatesh, Practicality of Tetragonal Nano-Zirconia as a Prospective Sorbent in the Preparation of [99]Mo/[99m]Tc Generator for Biomedical Applications, Chromatographia, 72 (2010) 875-884.

[65] V.S. Le, Procedures for the production of poly-Zirconium-compound (PZC) based chromatographic Tc-99m generator to be available for clinical application, in: Fnca Workshop on the Utilization of Research Reactors, 2006.

[66] M. Tanase, K. Tatenuma, K. Ishikawa, K. Kurosawa, M. Nishino, Y. Hasegawa, A [99mTc] generator using a new inorganic polymer adsorbent for (n, γ) [99Mo], Appl. Radiat. Isot., 48 (1997) 607-611.

[67] V. Le, Procedures for the production of poly-Zirconium-compound (PZC) based chromatographic Tc-99m generator to be available for clinical application, 2004.

[68] J. Serrano, V. Bertin, S. Bulbulian, Mo-99 sorption by thermally treated hydrotalcites, (2000).

[69] J.S. Lee, H.S. Han, U.J. Park, K.J. Son, H.Y. Shin, S.B. Hong, K.D. Jang, J.S. Lee, Adsorbents for Radioisotopes, Preparation Method Thereof, and Radioisotope Generators Using the Same, US20120244055A1, 2010.

[70] M.I. Aydia, A.S. Hiekal, K.M. El-Azony, T.Y. Mohamed, I.M. Shahin, Preparation and characterization of poly nano-cerium chloride for [99Mo] production based on neutron activation reactions, Appl. Radiat. Isot., 163 (2020) 109211.

[71] H. El-Said, H. Ramadan, M. Abbas, M. El-Hashash, [99Mo]/[99mTc] radioisotope generator based on adsorption of [99Mo] (VI) on cerium (IV) molybdate column matrix, Radiochim. Acta, 106 (2018) 991-999.

[72] M. Mostafa, H.M. Saber, A.A. El-Sadek, M.Y. Nassar, A.S. Amin, Sorption of Mo(VI) on zirconium molybdosilicate gel and potential application as a [99Mo]/[99mTc] generator, Radiochem., 58 (2016) 409-414.

[73] M. Sharbatdaran, F. Farzaneh, M.M. Larijani, M.R. Davarpanah, S.A. Nosrati, Sol–gel synthesis and characterization of silica–zirconia inorganic polymer as [99Mo]/[99mTc] generator, J. Sol-Gel Sci. Technol., 74 (2015) 613-620.

[74] A.B. Willett, V.V. Grantham, Determination of hemolytic anemia through the study of [51Cr] red cell survival and splenic sequestration, J. Nucl. Med. Technol., 36 (2008) 95-98.

[75] O. Maranci, A.B. Tugrul, The Chronic Dose Assessment of Three Critical Organs for Liver Scintigraphy with Using Cr-51, Acta Phys. Pol A, 132 (2017) 476-478.

[76] T.K. Trung, N.A. Ramsahye, P. Trens, N. Tanchoux, C. Serre, F. Fajula, G. Férey, Adsorption of C5–C9 hydrocarbons in microporous MOFs MIL-100(Cr) and MIL-101(Cr): A manometric study, Microporous Mesoporous Mater., 134 (2010) 134-140.

[77] W. Strzempek, E. Menaszek, B. Gil, Fe-MIL-100 as drug delivery system for asthma and chronic obstructive pulmonary disease treatment and diagnosis, Microporous Mesoporous Mater., 280 (2019) 264-270.

[78] Y. Cai, J. Feng, X. Tan, X. Wang, Z. Lv, W. Chen, M. Fang, H. Liu, X. Wang, Efficient capture of ReO_4^- on magnetic amine-functionalized MIL-101(Cr): Revealing from selectivity to mechanism, Sci. Total Environ., 771 (2021) 144840.

[79] W. Xuan, C. Zhu, Y. Liu, Y. Cui, Mesoporous metal-organic framework materials, Chem. Soc. Rev., 41 (2012) 1677-1695.

Adsorption of molybdenum on Zr-based MOFs for potential application in the ^{99}Mo/^{99m}Tc generator

2

UiO-66

Eluted ^{99m}Tc solution
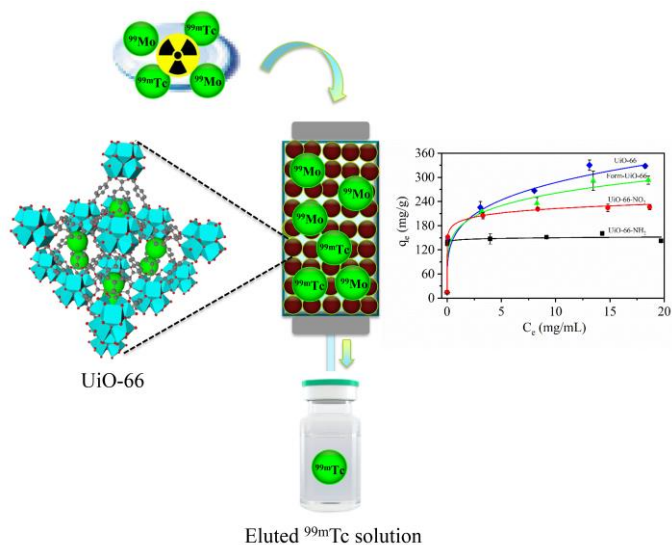
Abstract

The potential of the metal-organic framework UiO-66 and its functionalized derivatives for their utilization in the ^{99}Mo/^{99m}Tc generator was assessed. Molybdenum adsorption experiments, structure characterization, molecular simulations and column experiments with molybdenum-99 were carried out. The results showed that the maximum molybdenum adsorption capacity achieved for UiO-66 was 335 mg g^{-1}. Adsorption on the surface of the UiO-66 occurs via electrostatic interaction and DFT calculations verified the enhanced affinity between the adsorbents and the molybdenum ions by Zr-O-Mo coordination, anion-π as well as hydrogen bonds. In addition, the performance of a ^{99}Mo/^{99m}Tc generator fabricated with Form-UiO-66 was evaluated. The results showed that adsorption was comparable with the experiments using non-active molybdenum and that the ^{99m}Tc elution efficiency of around 70% could be achieved without zirconium breakthrough.

2.1 Introduction

Technetium-99m (^{99m}Tc) is the most often used radionuclide due to its application in organ perfusion, tumour imaging and bone scanning, among others, with around 40 million diagnostic procedures per year [1]. The main reasons for ^{99m}Tc ubiquitous utilization are its decay characteristics, which include the relatively low γ-ray energy, a short half-life (6.1 h), but also its rich chemistry and a wide availability via the ^{99}Mo/^{99m}Tc generator [2, 3]. Nowadays, the ^{99}Mo production is based on the fission of enriched uranium-235 target, which is irradiated in a limited number of nuclear reactors [4, 5]. On top of that, most of nuclear reactors are at end of their operational life and need regular maintenance, causing serious problems for the supply of ^{99}Mo [6]. For example, the reactors in Canada and the Netherlands shut down unexpectedly for a considerable time in 2008, resulting in a significant decrease worldwide of ^{99}Mo availability [7, 8]. In addition, a low yield of only about 6% is obtained and therefore enormous nuclear waste is produced during this process [9]. To overcome those disadvantages, several alternative production routes have been proposed. However, compared with uranium-235 fission, all the alternative routes deliver ^{99}Mo of much lower specific activity (LSA), preventing the preparation of ^{99}Mo/^{99m}Tc generators with sufficient activity [10]. In order to use such LSA ^{99}Mo, the adsorption capacity of the generators needs to be considerably increased.

The conventional bulk adsorbent utilized in the generator column is alumina (Al_2O_3) because of its high thermal stability, chemical stability, radiation stability and affinity towards molybdenum. However, alumina has a rather low molybdenum adsorption capacity ranging from 2 to 20 mg g^{-1} [11]. In an attempt to improve the adsorption capacity, a variety of materials having nano-dimensions or mesoporous structures were investigated as adsorbents due to their large pore volume and high surface area. For example, Saptiama et al. [12] reported the fabrication of mesoporous alumina spheres using post-synthesis water-ethanol treatment and reaching Mo adsorption capacity of 56.2 mg g^{-1} at pH 3. Denkova et al. [13] utilized Al-TUD-1 having high surface area and achieved a maximum adsorption capacity of 112 mg g^{-1}. Chakravarty et al. [14] synthesized nanocrystalline Al_2O_3 with average crystallite size 2~3 nm using a template method resulting in very high adsorption capacity in the order of 225±20 mg g^{-1} when applying a double column design. Although these studies are very

promising, the obtained adsorption capacities are still insufficient to be applied to LSA ^{99}Mo produced by most of the production routes, leaving a room for further improvement.

Very promising materials are the so-called metal-organic frameworks (MOFs) which have received wide attention in many applications including gas capture [15-17], catalysis [18], [19], wastewater treatment [20, 21], drug delivery [22-25], and others [26-28]. Compared with traditional porous materials, MOFs exhibit large surface area, high porosities, versatile structures and easy functionalization [29]. However, the degradation of some MOFs in water or extreme environment limits their industrial applications [30, 31]. Recently, a zirconium-based MOF, UiO-66, was researched extensively as an adsorbent due to its water stability, excellent chemical and thermal stability [32-34]. Furthermore, it demonstrated that hydroxyl groups play an important role in molybdenum adsorption based on previous reports [12, 35], which is why this material was selected in this research.

In this work, the UiO-66 and its functionalized derivatives were synthesized and characterized and their molybdenum adsorption properties were investigated at different molybdenum concentrations. To understand the interaction pathway between the adsorbent and the molybdenum species, the adsorption mechanism was researched using FT-IR, X-ray photoelectron spectra and DFT simulations. Finally, the synthesized Form-UiO-66 was used for the fabrication of ^{99}Mo/^{99m}Tc generators and its ^{99m}Tc elution performance was evaluated.

2.2 Experimental details

2.2.1   Synthesis and characterization of UiO-66 derivatives

The UiO-66 and its derivatives were synthesized using terephthalate, 2-nitroterephthalic acid and 2-aminoterephthalic acid as ligands based on previously reported methods [32, 36]. The detailed descriptions of the synthesized processes are presented in the Supporting Information (S-2).

Powder X-ray diffraction measurements were performed on a PANalytical X'Pert Pro pw3040/60 diffractometer with Cu Kα radiation operating at 45 kV and 40 mA. Nitrogen adsorption isotherms were obtained using a Micromeritics Tristar II at 77 K and the BET surface area was calculated at a relative pressure range between 0.05~0.15. Before the measurement, samples were degassed under vacuum at 200 °C for 16 h. Surface morphology

was recorded by a field emission scanning electron microscopy (SEM, JSM-7001F) and elemental composition was collected with an energy dispersive spectrometer (EDS, JEOL ISM-IT100). Fourier transform infrared spectroscopy (FT-IR) was collected over a range of 400~4000 cm^{-1} using a NICOLET 6700 and samples were dispersed in KBr and pellets with a diameter of 10 mm were made. The molybdenum concentrations before and after adsorption were measured using inductive coupled plasma optical emission spectrometry (ICP-OES, Optima 4300 DV, Perkin Elmer). 1 mg of powder sample was dispersed in 2 ml of solution with a pH range of 2-12 and the pH of the solution was adjusted using NaOH and HCl solutions. The Zeta potential of the suspension was measured using a Malvern ZetaSizer nano-ZS instrument. X-ray photoelectron spectra (XPS) of UiO-66 were performed by Thermofisher Scientific electron spectroscopy with K-alpha surfaces analysis.

2.2.2 Molybdenum adsorption

The adsorption capacity of molybdenum on Zr-based MOFs was determined by dispersing the powder in solutions of different molybdenum concentrations. The change in concentration before and after the addition of MOFs determines the amount of molybdenum adsorbed. First, a molybdenum solution (20 mg mL^{-1}) was prepared by dissolving 750 mg of MoO$_3$ into 40 mL of NaOH solution (1 M) and the pH of the solution was adjusted to 3.00 ± 0.03 by adding HCl. Then the total volume of the above solution was adjusted to 100 ml using stock solution (hydrochloric acid solution with pH 3). Finally, the prepared molybdenum solution was diluted into different concentrations ranging from 0.1 mL to 20 mL using Mili-Q water. The Mo adsorption of all the adsorbents was determined by batch equilibration experiments. An accurately weighed amount of adsorbent (circa 10 mg) was added into 1 mL Mo solution at a certain concentration and shaken at room temperature for 16 h with a speed of 1200 rpm. Adsorption isotherms were determined in a Mo concentration range from 0.1 to 20 mg mL^{-1}. The concentrations of the solution before and after absorption were measured by ICP-OES and all tests were conducted in triplicate at room temperature. The static adsorption capacity was calculated by the following equation:

$$q_e = \frac{(C_0 - C_e) \times V}{m}$$

Where C_e and C_0 were molybdenum concentrations at the equilibrium and before adsorption, respectively; V was the volume of solution (mL) and m was the weight of adsorbent (g).

Moreover, the Teflon column in ^{99}Mo/^{99m}Tc generator was prepared as shown in the schematic diagram in Figure S2.1. Then, 24 mL of ^{99}Mo solution with a concentration of 10 mg mL^{-1} was passed through the column at a flow rate of 0.05 mL min^{-1} and the dynamic adsorption capacity was calculated. After loading ^{99}Mo, the column was rinsed with 100 mL of saline solution to remove the loosely adsorbed molybdenum ions and the practical dynamic adsorption capacity was subsequently determined. Finally, the elution performance of the generator was assessed over a period of 6 days. More details about practical dynamic adsorption capacity and radiochemistry purity were described in the Supporting Information (S-3).

2.2.3 DFT

Spin-polarised DFT calculations with the PBE exchange-correlation functional [37], as implemented in the plane wave Vienna *Ab initio* Simulation Package (VASP) [38], were performed. A high energy cut-off of 520 eV along with a 3x3x3 Monkhorst-Pack k-point set was selected. Valence-core interactions were probed with the projector augmented wave (PAW) [39] approach considering 4, 1, 6, 12, and 14 valence electrons for C, H, O, Zr, and Mo respectively. In order to account for Van der Walls interactions, the zero damping DFT-D3 method of Grimme et. al. [40] was applied in all calculations. Probing the molecular and atomic interactions between the molybdenum species and the host MOF structure was achieved by determining the binding energy, calculated according to the following formula: [41, 42]

$$E_B = E_{MH} - E_M - E_H$$

where E_M is the total energy of the molybdenum species isolated in a 25x25x25 Å^3 vacuum box, E_H is the total energy of the host structure (MOF), and E_{MH} is the total energy of the adsorbed system (molybdenum species and host). Based on the definition of the binding energy provided above, a more negative value indicates stronger binding between the molybdenum species and the MOF. All the relevant structures were geometrically optimized, allowing relaxation of atomic positions, cell shape and volume during the calculation. The total energies were obtained from subsequent self-consistent calculations.

2.3 Results and Discussion

2.3.1 Structural characterization

The crystal structure of as-prepared Zr-based MOFs was examined by X-ray diffraction and the results can be found in Figure 2.1 (a). It can be observed that all synthesized samples exhibit the characteristic diffraction peaks of UiO-66, indicating that the other three derivative frameworks are isostructural with UiO-66. However, the intensities of UiO-66-NH_2 and UiO-66-NO_2 are lower, indicating less crystallinity.

Figure 2.1 (b) displays FT-IR spectroscopy of UiO-66 and its derivatives as synthesized. A broad band seen at 3421 cm^{-1} for all the materials is assigned to the stretching modes of O-H, which is attributed to the adsorbed water on the surface of the samples [43]. The band near 1583 cm^{-1} and 1397 cm^{-1} for all samples can be ascribed to the stretching vibration of C=O on the BDC and the vibration of a benzene ring, respectively [36, 44]. The small bands at 485 cm^{-1}, 665 cm^{-1} and 748 cm^{-1} represent the Zr-O and Zr-O_2 stretching vibrations [45]. For the UiO-66-NH_2, the amino group shows absorption bands at 3354 cm^{-1} and 3476 cm^{-1} because of symmetric and asymmetric N-H stretching modes [32]. The appearance of a band at 1549 cm^{-1} can be attributed to the asymmetric stretching mode of NO_2 [46]. Furthermore, the band at 1257 cm^{-1} in the UiO-66-NH_2 and UiO-66-NO_2 particles is due to the C-N stretching absorption mode, suggesting the successful introduction of -NH_2 and -NO_2 groups [47].
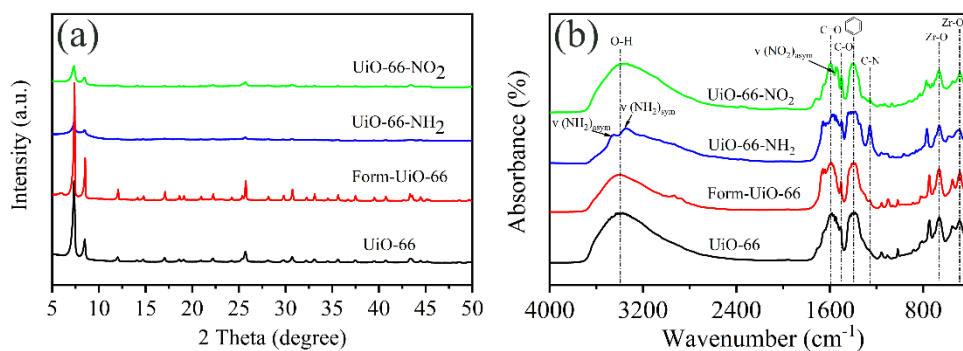

Fig. 2.1. (a) XRD patterns and (b) FT-IR spectra of UiO-66 and its derivatives before molybdenum adsorption.

Figure 2.2 (a) shows the N_2 adsorption isotherm of UiO-66, UiO-66-NH$_2$, Form-UiO-66 and UiO-66-NO$_2$ at 77 K. The surface area and pore volumes of all materials were calculated, as shown in Table S2.1. Non-functionalized UiO-66 and Form-UiO-66 have the largest surface area and pore volumes. Their specific surface areas are 1624 m^2 g^{-1} and 1653 m^2 g^{-1}, whereas the total pore volumes are 0.59 m^3 g^{-1} and 0.61 m^3 g^{-1}, respectively. Materials functionalized with amino (UiO-66-NH$_2$) and nitro groups (UiO-66-NO$_2$) have a lower surface area and pore volumes than the non-functionalized counterparts UiO-66s (as shown in Table S2.1). Besides, the UiO-66-NO$_2$ exhibited an IV-type adsorption isotherm with a hysteresis cycle. This occurrence could be caused by aggregated small nanoparticles forming large aggregates, generating voids with different sizes within the granules, which is consistent with the SEM micrographs (Figure S 2.2d).
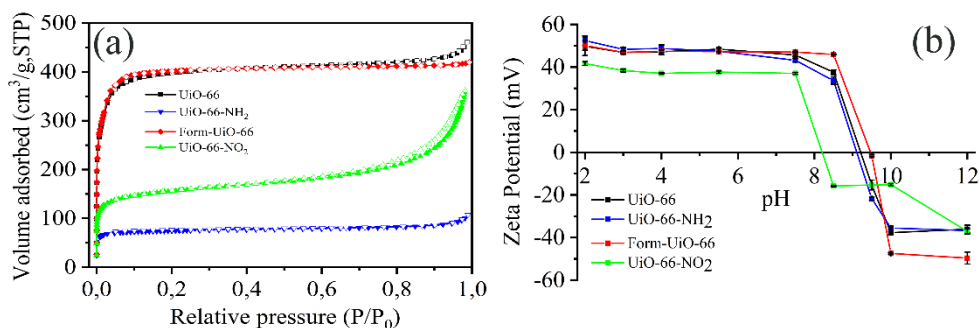

Fig. 2.2. (a) N$_2$ adsorption-desorption isotherms and (b) zeta potential of UiO-66 and its derivatives.

The pH has an essential influence on molybdenum adsorption, since it affects not only the different molybdenum species present, but also the surface charge of the adsorbents. It has been reported that at pH <2 the dominant species is $Mo_7O_{24}^{3-}$; while $Mo_7O_{24}^{6-}$ and $Mo_8O_{28}^{4-}$ exist as the main species at pH 2~5 and MoO_4^{2-} predominates pH at >6 [48]. To determine the surface charge of the adsorbents, the zeta potential of all samples was measured in the pH range of 2 to 12, as shown in Figure 2.2 (b). It can be observed that the isoelectric points (IEP) of all the samples are located between pH of 8 and 10, which is similar to alumina. When the pH is below its IEP, the material is positively charged facilitating its interaction with molybdenum species that are negatively charged through electrostatic forces. When the pH is above the IEP, all samples have negative surface charges that will cause the electrostatic

repulsion towards Mo anions. Therefore, the following molybdenum adsorption experiments were carried out under an acidic environment so that adsorption can be enhanced.

2.3.2 Molybdenum adsorption

The molybdenum adsorption isotherms of UiO-66 MOFs were investigated under different molybdenum concentrations at room temperature, as shown in Figure 2.3. As can be seen, molybdenum adsorption on all adsorbents displayed a fast increase and their molybdenum uptake is about 150 mg g^{-1} at relative low molybdenum concentration, which may be attributed to the strong interaction between adsorbents and molybdenum species. With molybdenum concentration increasing, the increase in adsorption capacity slowed down until reaching equilibrium. Finally, the saturated capacity of UiO-66-NH$_2$, UiO-66-NO$_2$, Form-UiO-66 and UiO-66 can reach up to 142 mg g^{-1}, 225 mg g^{-1}, 293 mg g^{-1} and 334 mg g^{-1}, respectively. The molybdenum uptake in UiO-66 showed the highest adsorption capacity, which is two times larger than that for UiO-66-NH$_2$.
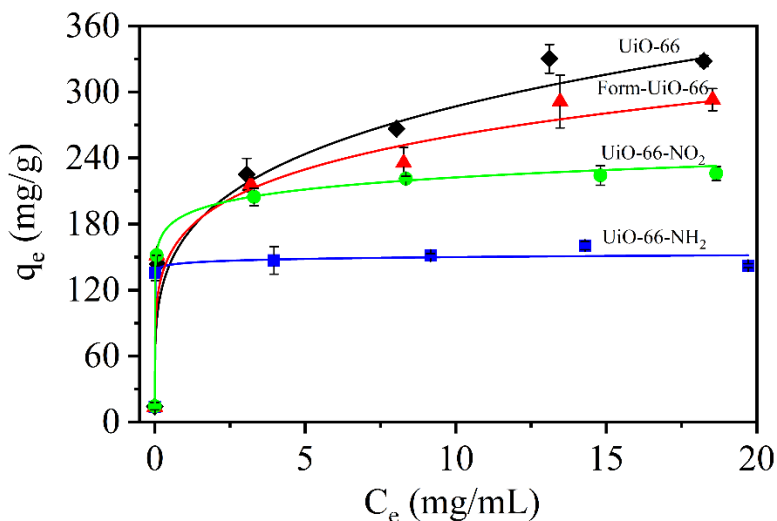

Fig. 2.3. Mo adsorption isotherms of UiO-66 (black), UiO-66-NH$_2$ (blue), Form-UiO-66 (red) and UiO-66-NO$_2$ (green) at pH 3.

To better understand the molybdenum adsorption on those adsorbents, the adsorption isotherms were linearly fitted using the Langmuir and Freundlich model. All calculated parameters of the two models are displayed in Table S2.2. As exhibited in Figure S2.3, the linear fit of the experimental data using the Langmuir model showed a better fit with higher

correlation coefficients ($R^2 > 96.5\%$) than the Freundlich model (Figure S2.4). The model displays that the maximum adsorption capacity of UiO-66, UiO-66-NH$_2$, Form-UiO-66 and UiO-66-NO$_2$ are 335 mg g^{-1}, 131 mg g^{-1}, 296 mg g^{-1} and 227 mg g^{-1}, respectively, which are consistent with adsorption isotherms. The relatively low adsorption capacity for UiO-66-NH$_2$ and UiO-66-NO$_2$ may be related to their relatively low surface area and their lower crystallinity. In Table 2.1, the adsorption capacity of Zr-based MOFs is compared to the Mo adsorption capacity on various other reported materials, showing the outstanding adsorption performance of UiO-66 MOFs.

Table 2.1. Comparison of the static Mo adsorption capacity of the as-synthesized MOFs with other adsorbent materials.

Samples	Mo adsorption capacity (mg g^{-1})	Surface area (m^2 g^{-1})	Ref.
TUD-1	112	402	[13]
Hydrous MnO$_2$	50	--	[49]
Hydrous TiO$_2$	230	--	[50]
Al-dropped mesoporous SiO$_2$	16.8	463	[51]
Nano-crystalline titania	141±2	320	[52]
Mesoporous γ-Al$_2$O$_3$	56.2	251	[12]
Nanocrystalline γ-Al$_2$O$_3$	200	252	[11]
PZC	270	--	[53]
Polymer embedded titania	100	38	[54]
UiO-66	335	1624	This work
Form-UiO-66	296	1653	This work
UiO-66-NH$_2$	131	295	This work
UiO-66-NO$_2$	227	575	This work

2.3.3 Molybdenum adsorption mechanism

To understand the interaction between the molybdenum species and the adsorbents, the MOFs adsorbents were further analyzed by XRD, FT-IR and EDS. In Figure S2.5, the XRD patterns show that all adsorbents retain good crystallinity and structure after molybdenum adsorption, as no shifts in the peak positions are observed. However, the relative intensities of the peaks are weakened after molybdenum adsorption, which may be due to trapped molybdenum species on the surface of the adsorbents leading to diminished X-ray contrast between pore cages and porous framework [55]. The EDS mappings (Figure S2.6) display uniform distribution of Mo, which suggests that molybdenum is homogeneously adsorbed in

the materials. Moreover, the FT-IR spectra (Figure S2.7) of UiO-66 MOFs after adsorption shows two new peaks appearing at 948 cm^{-1} and 889 cm^{-1}, which are assigned to the vibration of the Mo=O stretching and Mo-O-Mo stretching of Mo species [56].
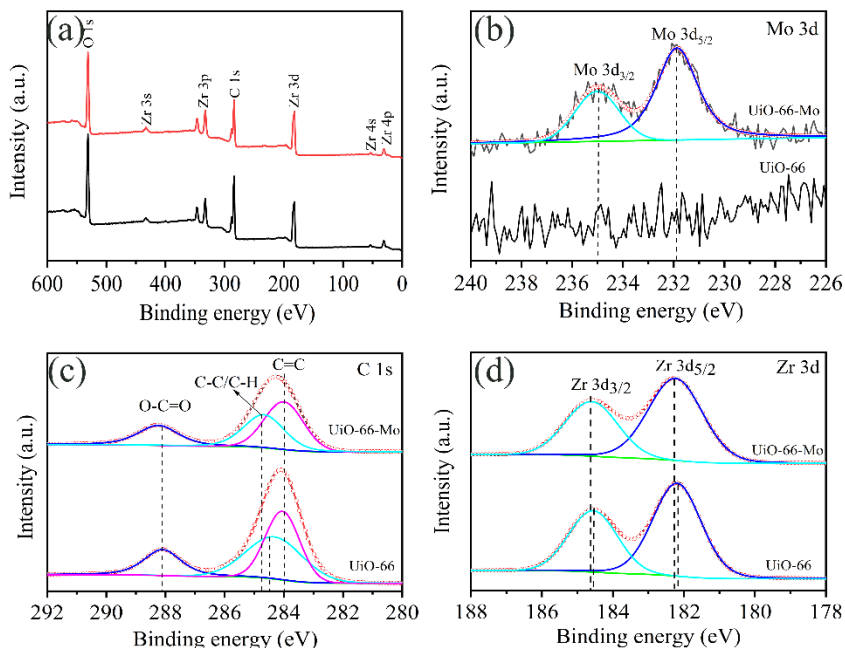

Fig. 2.4. XPS spectra of UiO-66 before and after molybdenum adsorption (a) survey; (b) Mo 3d; (c) C 1s; (d) Zr 3d.

The chemical composition and oxidation states of UiO-66 with the best adsorption performance before and after Mo adsorption were analyzed by XPS. As shown in Figure 2.4 (a), the XPS survey indicates the elements of C, O, Zr exist in the samples. The Mo 3d spectra of UiO-66 are presented in Figure 2.4 (b). Two peaks for Mo $3d_{5/2}$ and Mo $3d_{3/2}$ are located at 231.8 and 234.9 eV, respectively. The gap of 3.1 eV between two peaks indicates a Mo^{6+} oxidation state [57, 58]. The C 1s spectra (Figure 2.4 (c)) of UiO-66 before adsorption can be deconvoluted into three peaks, which are assigned to C=C (284.0 eV), C-C/C-H (284.3 eV) and O-C=O (288.1 eV) [59]. However, the peak of C-H/C-C for UiO-66 after adsorption shifts to 284.7 eV, which indicates the chemical environment of C-H/C-C was changed after loading Mo species. This might be attributed to the different electron density near C-H/C-C in the pores due to the presence of Mo species. In Figure 2.4 (d), the binding energy of Zr 3d exhibits two peaks corresponded to Zr $3d_{5/2}$ and Zr $3d_{3/2}$. After molybdenum adsorption, the

peak of Zr $3d_{5/2}$ shifts from 181.99 eV to 182.24 eV and the peak of Zr $3d_{3/2}$ shifts from 184.36 eV to 184.6 eV. The shift of binding energy towards higher energy may be due to the coordination between Mo species and Zr clusters, causing the change of electron density of Zr [60, 61]. This behavior suggests an electronic interaction between Mo species and Zr-O clusters.
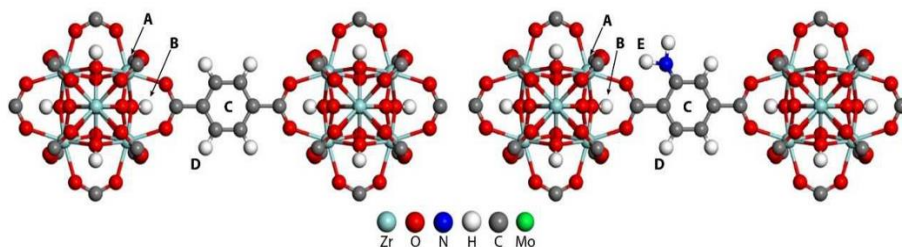

Fig. 2.5. Adsorption sites within the UiO-66 and UiO-66-NH$_2$ MOF structures.

To further elucidate the interaction mechanism between Mo species and UiO-66 MOFs, DFT calculations were conducted to investigate the adsorption properties of molybdenum species on the Zr-based MOFs. From the wide variety of the potential Mo(VI) species that exist, depending on the pH, we examined the following representative molecules, H_2MoO_4, MoO_4^{2-} and $Mo_7O_{24}^{6-}$ (Figure S2.8). Mononuclear species of molybdenum exist when molybdenum concentration is lower than 10^{-4} M. Polynuclear molybdenum species can be formed when molybdenum concentration is higher than 10^{-4} M. $Mo_7O_{24}^{6-}$ is the main species at pH 3~4 when molybdenum concentration is larger than 10^{-3} M [62]. Furthermore, five possible adsorption sites were chosen for inner-sphere calculation, including Zr on clusters (A), O-H groups (B), benzene rings (C), arene C-H groups (D) and the -NH$_2$ or -NO$_2$ groups (E), as shown in Figure 2.5. Therefore, five possible molecular interactions were conducted for DFT calculations: coordination between Zr on clusters and the oxygen of Mo species [63], interaction between hydroxyl groups and the oxygen of Mo species [64], the π-anion interaction between Mo anions and benzene rings [65], and hydrogen bond formation between Mo anions and arene C-H groups/-NH$_2$/NO$_2$ [66]. According to the definition provided in the computational method section, negative energy indicates favourable adsorption and the calculated energies are summarized in Table 2.2.
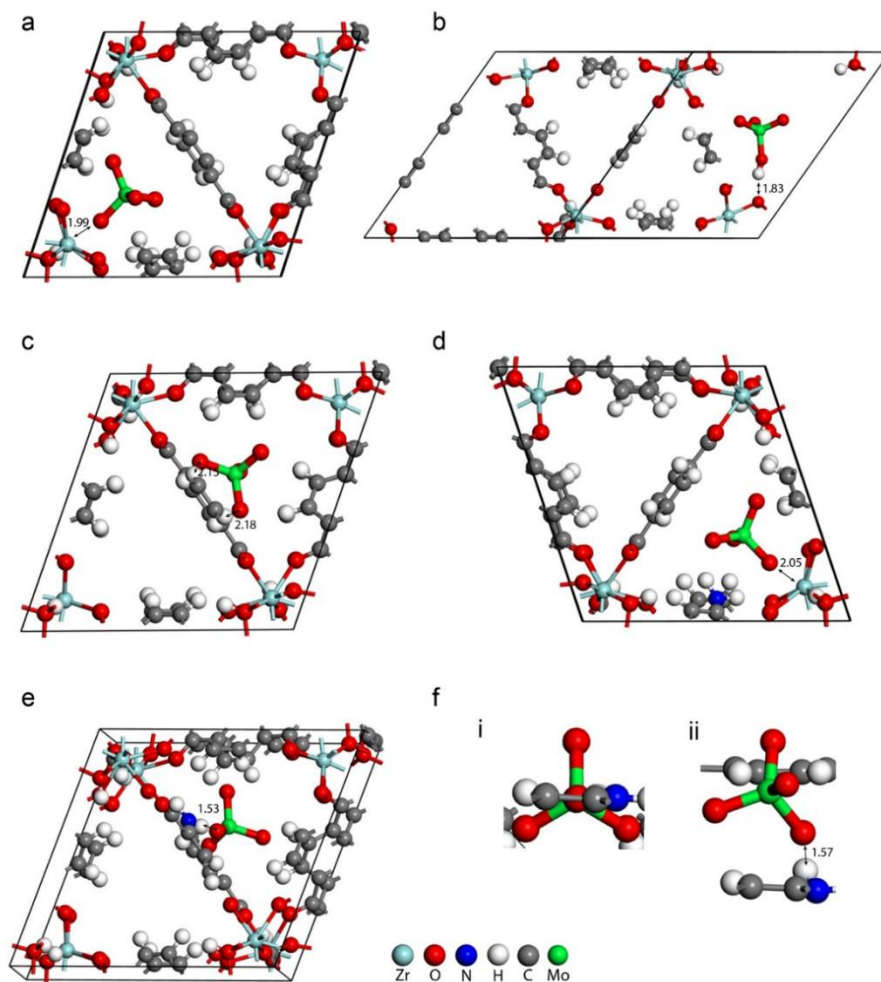
Fig. 2.6. Optimized structures of MoO_4^{-2} adsorption within the UiO-66 host structure near a) position A b) position B, where we observe that the O-H of the Zr-O-H environment of the host breaks to form $HMoO_4^{-1}$, c) and position D. d) Optimized structures of MoO_4^{-2} adsorption within the UiO-66-NH$_2$ host structure near position A and e) position E. f) Difference between the two adsorption environments of adsorption near position E (i) -73 and (ii) -50 kJ/mol. All the interatomic distances indicated are in Å.

For UiO-66, the adsorption of MoO_4^{2-} species had high interaction energy on positions A (-141 kJ mol^{-1}) and B (-130 kJ mol^{-1}). The configurational environments are shown in Fig. 2.6. The optimal configurations between Zr nodes and MoO_4^{2-} species showed the Zr-O formation

with a distance of 1.99 Å (Fig. 2.6a). This connection near the Zr-clusters caused the change of electron density of the Zr-clusters, which is consistent with the analysis of the Zr 3d spectra of UiO-66. Additionally, our calculations predict that the MoO_4^{2-} species can capture the hydrogen atom of the Zr-core (position B), forming $HMoO_4^-$ (Fig. 2.6b). The newly formed molecule stabilizes at a distance of about 1.88 Å from the pore walls. The adsorption site D showed relatively low adsorption energy (-25 kJ mol^{-1}) and formed hydrogen bonds of 2.15 to 2.18 Å, which is why the binding energy of C-H moved 0.4 eV in XPS spectra of C 1s (Figure 2.4c). However, the value of adsorption energy for the C site is positive, indicating unfavourable adsorption. Therefore, the adsorption ability for UiO-66 follows the A<B<D<C order. This behaviour, as mentioned above, is consistent with the UiO-66-NH_2 host that shows the order of A<B<E<D<C. As shown in Table 2.2, the nitrogen environment of the UiO-66-NH_2 structure offers an additional adsorption site with strong binding energies. For adsorption near the NH_2 environment, we scanned more than 12 different conformers, generally revealing two distinct environments for favourable binding (-73/-50 kJ mol^{-1}), related to the orientation of the molecule. The binding oxygen of the MoO_4^{2-} species prefers to be aligned with the plane formed by the NH_2 linker, acquiring lower energies (Fig. 2.6f). Strong stable binding for the neutral H_2MoO_4 species occurs near the hydrogen atom of the Zr cluster (position B), where one of the two hydrogen-free oxygens of the adsorbent binds to the hydrogen of the cluster at a distance of 1.75 Å. The rest of the adsorption sites offer an almost equivalent environment for adsorption with binding energies around -65 kJ mol^{-1} (Figure S2.9), revealing a relatively flat energy landscape both in the UiO-66 and UiO-66-NH_2 hosts. The relatively flat energy landscape indicates enhanced kinetics for the diffusion of the H_2MoO_4 species inside the MOF, allowing site accessibility for all the available material and thus enhancing the adsorption process. An interesting observation is that the H_2MoO_4 species does not necessarily chemically bind to the host structure due to its electrical neutrality. Nonetheless, it favourably adsorbs near the pore walls of the host (Figure S2.9 d-f) in a process that resembles more physio-sorption, which is also evident from the adsorption energy values obtained for positions A, C, D, and E in Table 2.2. However, the neutral H_2MoO_4 species, having the right size and orientation, can chemically adsorb to a binding spot that combines the configurational environment of the B, C and E sites (see Table 2.2). This favourable binding of -113 kJ mol^{-1} is depicted in Figure S2.10, where the adsorbent creates bonds with the host structure of 2.36 Å (H-C), 1.88 Å (O-H) and, 1.93 Å (H-N).

$Mo_7O_{24}^{6-}$ species is a bulky anion, having dimensions of 0.97 by 0.49 nm. As a result, an important question is whether $Mo_7O_{24}^{6-}$ can intercalate within the host structure. DFT optimization of the UiO-66 hosts indicates an available pore size of 1.05 nm. By inserting $Mo_7O_{24}^{6-}$ within the host structure, we find a highly favourable binding environment (Table 2.2). This result is explained by the partial transformation of the host structure where some of the linkages are likely to react with the oxygen of the $Mo_7O_{24}^{6-}$ forming C-O-H bonds (Figure S2.11). The $Mo_7O_{24}^{6-}$ molecule fits within the host, with most of the adsorbent's oxygen atoms being near the hydrogen atoms of the linkage molecules with distances between 2 and 2.4 Å. We also observe that the oxygen atoms of the adsorbent can successfully bind to C with an O-C bond of 1.43 Å. In the case of perfect alignment of $Mo_7O_{24}^{6-}$, an additional bond is created between O and Zr with a distance of 2.35 Å (Fig. 2.7). Further indications of the favourable environment created for $Mo_7O_{24}^{6-}$ adsorption is put forward by examining the predicted volume changes with DFT. The relaxed adsorption structures reveal a volume change of 6%. These values are definitely within the manageable range for mechanical stresses, especially for flexible materials such as MOFs.

Table 2.2. Adsorption Sites and Energies (kJ mol^{-1}) (* refers to a configurational environment that combined with B, C and E sites).

MOFs	Mo species	Adsorption Sites and Energies in (kJ mol^{-1})				
		A	B	C	D	E
UiO-66	MoO_4^{2-}	-141	-130	+33	-25	-
	H_2MoO_4	-65/-56	-97	-65	-61	-
	$Mo_7O_{24}^{6-}$			-1539		
UiO-66-NH$_2$	MoO_4^{2-}	-155	-127	+10	-9	-73[i] /-50[ii]
	H_2MoO_4	-74	-101/-113*	-50	-73	-57

Another important consideration is if the reaction kinetics allow these extremely favorable configurations to occur. The $Mo_7O_{24}^{6-}$ entering the main structure needs to diffuse through the side pores (~0.69 nm) of the MOF, which are considerably smaller. However, the linkers can rotate during motion, causing extended pores, this would be helpful for the penetration

of molybdenum species [67, 68]. Nevertheless, our calculations depict strong indications for favourable adsorption, showing that the binding spots and coordination offered for the $Mo_7O_{24}^{6-}$ species lead to significantly lower energy (more stable) configurations when in the environment of the UiO-66 hosts. Certainly, there are also some other minor molybdenum species in solution, such as $HMoO^-$, $H_2Mo_6O_{21}^{4-}$, which have smaller sizes and would enter the porous structure more easily. Moreover, In the case of UiO-66-NO$_2$, the -NO$_2$ groups are also favourable for Mo adsorption and it has similar binding energy with the UiO-66-NH$_2$. Overall, molybdenum species can adsorb on the surface of Zr-based MOFs by electrostatic adsorption. The inner-sphere interaction between molybdenum species and adsorbents at several adsorption sites is enhanced through the Zr-O-Mo coordination, hydrogen bonds and π-anions.
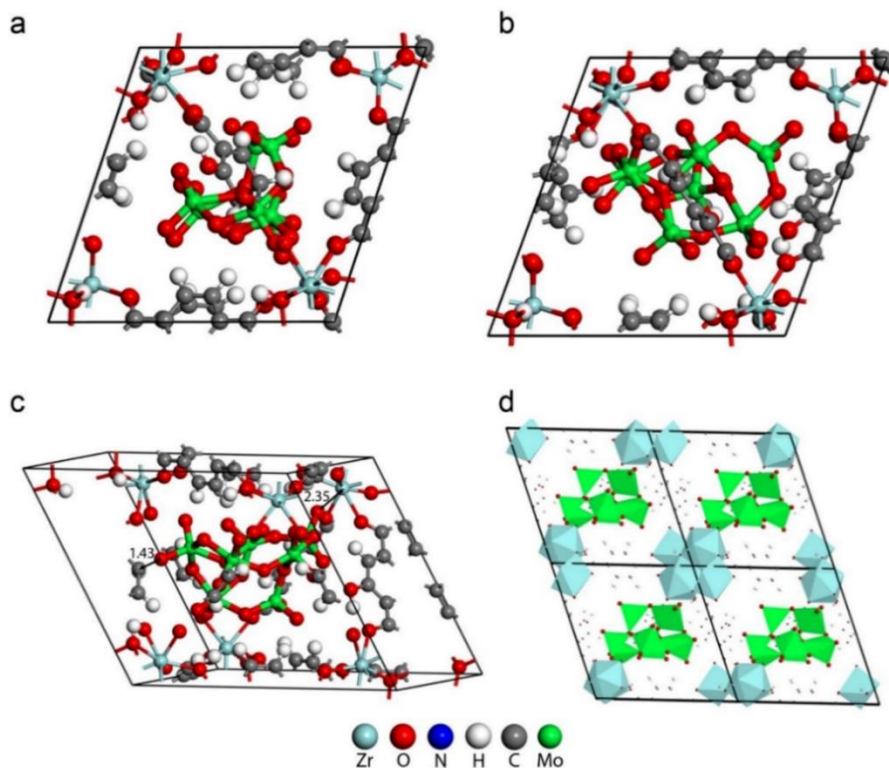

Fig. 2.7. Optimized structure from different angles of $Mo_7O_{24}^{-6}$ in the UiO-66 host.

2.3.4 Performance of Form-UiO-66 as adsorbent in $^{99}Mo/^{99m}Tc$ generator

In order to evaluate the performance of the prepared Zr-based MOFs as adsorbent in the $^{99}Mo/^{99m}Tc$ generator, Form-UiO-66 was selected due to its higher crystal purity and larger particle size, which allows it to be applied in a chromatographic column and continuous loading and elution. The dynamic molybdenum adsorption uptake of Form-UiO-66 was determined to be 203 mg g^{-1}, which is consistent with the adsorption results utilizing non-radioactive molybdenum. After removing the loosely adsorbed molybdenum ions by flushing the column with 0.9% saline solution, the practical dynamic adsorption capacity was determined to be 145 mg g^{-1}, which is consistent with the uptake value during fast adsorption process at low molybdenum concentration (See Figure 2.3). In addition, this practical uptake is more than 7 times than that of conventional bulk alumina with an adsorption capacity in the range of 2~20 mg g^{-1}.

Table 2.3. Elution parameters of the Form-UiO-66 in $^{99}Mo/^{99m}Tc$ generator over a period of 6 days.

Elution No.	Elution efficiency (%)	^{99}Mo breakthrough (%)	Zr breakthrough (ppm)
1	61.4	1.1	0
2	57.6	1.2	0
3	76.2	1.2	0
4	73.1	1.3	0
5	71.2	0.9	0
6	74.7	1.3	0

Subsequently, the column was eluted daily with saline solution for a period of 6 days and ^{99m}Tc elution efficiency was determined. Table 2.3 shows the elution results of the prepared column. It can be observed that about 60% of ^{99m}Tc was eluted in the first two elutions and >70% of ^{99m}Tc was eluted in the following days. The Zr breakthrough in all elution fractions was below the detection limit of ICP-OES (<10 ppb). The presence of ^{99}Mo in the ^{99m}Tc eluted samples is about 1.2% in all elutions, which is higher than the limit of <0.1% as described in the International Pharmacopoeia (IP) [69]. The ^{99}Mo breakthrough may be associated with the size of the column used, which can lead to channel forming. These results prove that our adsorbents show good adsorption performance and chemical stability, while

the elution performance of the column in the ^{99}Mo/^{99m}Tc generator needs to be optimized before clinical applications.

A generator based on 2 g of Form-UiO-66 as adsorbent could deliver 2 Ci ^{99}Mo activity if ^{99}Mo with a specific activity of 6.9 Ci g^{-1} of higher was utilized. The alternative methods of fission deliver ^{99}Mo with specific activities in the range of 1~10 Ci g^{-1} [2]. This indicates the potential of MOFs as adsorbents in ^{99}Mo/^{99m}Tc based on LSA ^{99}Mo, which could provide an alternative to the current scenario and open the possibility of using many more production facilities worldwide.

2.4 Conclusions

In conclusion, this study showed that UiO-66 and its functionalized derivatives have great potential to be utilized as molybdenum adsorbents in ^{99}Mo/^{99m}Tc generator. The results reveal that UiO-66 and its functionalized derivatives exhibit outstanding Mo adsorption performance and that the maximum Mo adsorption capacity of UiO-66 can reach up to 335 mg g^{-1}, which is higher than most metal oxides for molybdenum adsorption. The adsorption mechanism was investigated by DFT, which indicates the interaction between MOFs and Mo species was affected by different binding such as Zr-O-Mo coordination, π-anions and hydrogen bonding. Moreover, DFT results proved that Mo$_7$O$_{24}$$^{6-}$ ions can be intercalated with the host structure by multiple binding sites. The Form-UiO-66 was successfully used for the ^{99}Mo/^{99m}Tc generator fabrication. The practical dynamic adsorption capacity of Form-UiO-66 was 145 mg g^{-1}, when a Mo concentration of 10 mg ml^{-1} was used. ^{99m}Tc can be eluted from the column within a 60~70% efficiency for 6 consecutive days without Zr breakthrough, but having ^{99}Mo breakthrough above the clinically allowed value. Therefore, UiO-66 MOFs have great potential for Mo adsorption and ^{99m}Tc elution in the ^{99}Mo/^{99m}Tc generator and a thorough study and optimization of the generator is under evaluation.

References

[1] D. Papagiannopoulou, Technetium-99m radiochemistry for pharmaceutical applications, J. Label. Compd. Radiopharm. 60 (2017) 502-520.

[2] V. S. Le, Tc-99m generator development: up-to-date Tc-99m recovery technologies for increasing the effectiveness of Mo-99 utilisation, Sci. Technol. Nucl. Install. 2014 (2014) 1-41.

[3] G.C. Krijger, B. Ponsard, M. Harfensteller, H.T. Wolterbeek, J.W. Nijsen, The necessity of nuclear reactors for targeted radionuclide therapies, Trends Biotechnol. 31 (2013) 390-396.

[4] M.R. Pillai, A. Dash, F.F. Knapp, Sustained availability of ^{99m}Tc: possible paths forward, J. Nucl. Med. 54 (2013) 313-323.

[5] E. National Academies of Sciences, Medicine opportunities and approaches for supplying molybdenum-99 and associated medical isotopes to global markets: proceedings of a symposium. National Academies Press: 2018.

[6] T. J. Ruth, The shortage of technetium-99m and possible solutions, Annu. Rev. Nucl. Part. Sci. 70 (2020) 77-94.

[7] A. J. Einstein, Breaking america's dependence on imported molybdenum, JACC Cardiovasc Imaging. 2 (2009) 369-371.

[8] J. Moret, J. Alkemade, T. M. Upcraft, E. Oehlke, H. T. Wolterbeek, J. R. van Ommen, A. G. Denkova, The application of atomic layer deposition in the production of sorbents for ^{99}Mo/^{99m}Tc generator, Appl. Radiat. Isot. 164 (2020) 109266.

[9] S. Hasan, M.A. Prelas, Molybdenum-99 production pathways and the sorbents for ^{99}Mo/^{99m}Tc generator systems using (n, γ) ^{99}Mo: A review, SN Appl. Sci. 2 (2020) 1782.

[10] M. R. Pillai, F. F. Knapp, Overcoming the ^{99m}Tc Shortage: Are Options Being Overlooked? J. Nucl. Med. 52 (2011) 15N.

[11] R. Chakravarty, R. Ram, A. Dash, M.R. Pillai, Preparation of clinical-scale ^{99}Mo/^{99m}Tc column generator using neutron activated low specific activity ^{99}Mo and nanocrystalline gamma-Al$_2$O$_3$ as column matrix, Nucl. Med. Biol. 39(7) (2012) 916-22.

[12] I. Saptiama, Y.V. Kaneti, Y. Suzuki, K. Tsuchiya, N. Fukumitsu, T. Sakae, J. Kim, Y.M. Kang, K. Ariga, Y. Yamauchi, Template-free fabrication of mesoporous alumina nanospheres using post-synthesis water-ethanol treatment of monodispersed aluminum

glycerate nanospheres for molybdenum adsorption, Small 14 (2018) e1800474.

[13] A.G. Denkova, B.E. Terpstra, O.M. Steinbach, J.t. Dam, H.T. Wolterbeek, Adsorption of molybdenum on mesoporous aluminum oxides for potential application in nuclear medicine, Sep. Sci. Technol. 48 (2013) 1331-1338.

[14] R. Chakravarty, R. Ram, R. Mishra, D. Sen, S. Mazumder, M.R.A. Pillai, A. Dash, Mesoporous alumina (MA) based double column approach for development of a clinical scale ^{99}Mo/^{99m}Tc generator using (n, γ) ^{99}Mo: An enticing application of nanomaterial, Ind. Eng. Chem. Res. 52 (2013) 11673-11684.

[15] S. Xiang, Y. He, Z. Zhang, H. Wu, W. Zhou, R. Krishna, B. Chen, Microporous metal-organic framework with potential for carbon dioxide capture at ambient conditions, Nat. Commun. 3 (2012) 954.

[16] P.G. Boyd, A. Chidambaram, E. Garcia-Diez, C.P. Ireland, T.D. Daff, R. Bounds, A. Gladysiak, P. Schouwink, S.M. Moosavi, M.M. Maroto-Valer, J.A. Reimer, J.A.R. Navarro, T.K. Woo, S. Garcia, K.C. Stylianou, B. Smit, Data-driven design of metal-organic frameworks for wet flue gas CO_2 capture, Nature. 576 (2019) 253-256.

[17] E. Lopez-Maya, C. Montoro, V. Colombo, E. Barea, J.A.R. Navarro, Improved CO_2 capture from flue gas by basic sites, charge gradients, and missing linker defects on nickel face cubic centered MOFs, Adv. Func. Mater. 24 (2014) 6130-6135.

[18] L. Jiao, Y. Wang, H.L. Jiang, Q. Xu, Metal-organic frameworks as platforms for catalytic applications, Adv. Mater. 30 (2018) e1703663.

[19] L. Zhu, X.Q. Liu, H.L. Jiang, L.B. Sun, Metal-organic frameworks for heterogeneous basic catalysis. Chem. Rev. 117 (2017) 8129-8176.

[20] N.L. Torad, M. Hu, S. Ishihara, H. Sukegawa, A.A. Belik, M. Imura, K. Ariga, Y. Sakka, Y. Yamauchi, Direct synthesis of MOF-derived nanoporous carbon with magnetic Co nanoparticles toward efficient water treatment, Small. 10 (2014) 2096-2107.

[21] B. Li, J.Q. Zheng, J.Z. Guo, C.Q. Dai, A novel route to synthesize MOFs-derived mesoporous dawsonite and application in elimination of Cu(II) from wastewater, Chem. Eng. J. 383 (2020) 123174.

[22] M.X. Wu, Y.W. Yang, Metal-organic framework (MOF)-based drug/cargo delivery and cancer therapy, Adv. Mater. 29 (2017) 1606134.

[23] I. Abánades Lázaro, R. S. Forgan, Application of zirconium MOFs in drug delivery and biomedicine, Coord. Chem. Rev. 380 (2019) 230-259.

[24] L.L. Tan, H. Li, Y. Zhou, Y. Zhang, X. Feng, B. Wang, Y.W. Yang, Zn^{2+}-Triggered drug release from biocompatible zirconium MOFs equipped with supramolecular gates, Small. 11 (2015) 3807-3813.

[25] I. Abanades Lazaro, C.J.R. Wells, R.S. Forgan, Multivariate modulation of the Zr-MOF UiO-66 for defect-controlled combination anticancer drug delivery, Angew. Chem. Int. Ed. Engl. 59 (2020) 5211-5217.

[26] P. Silva, S.M. Vilela, J.P. Tome, F.A. Almeida Paz, Multifunctional metal-organic frameworks: from academia to industrial applications, Chem. Soc. Rev. 44 (2015) 6774-6803.

[27] C.Y. Lee, O.K. Farha, B.J. Hong, A.A. Sarjeant, S.T. Nguyen, J.T. Hupp, Light-harvesting metal-organic frameworks (MOFs): efficient strut-to-strut energy transfer in bodipy and porphyrin-based MOFs, J. Am. Chem. Soc. 133 (2011) 15858-15861.

[28] P. Kumar, A. Deep, K.H. Kim, Metal organic frameworks for sensing applications, Trac-Trend Anal. Chem. 73 (2015) 39-53.

[29] J. Li, X. Wang, G. Zhao, C. Chen, Z. Chai, A. Alsaedi, T. Hayat, X. Wang, Metal-organic framework-based materials: superior adsorbents for the capture of toxic and radioactive metal ions, Chem. Soc. Rev. 47 (2018) 2322-2356.

[30] J. Canivet, A. Fateeva, Y. Guo, B. Coasne, D. Farrusseng, Water adsorption in MOFs: fundamentals and applications, Chem. Soc. Rev. 43 (2014) 5594-5617.

[31] N.C. Burtch, H. Jasuja, K.S. Walton, Water stability and adsorption in metal-organic frameworks, Chem. Rev. 114 (2014) 10575-10612.

[32] M. Kandiah, M.H. Nilsen, S. Usseglio, S. Jakobsen, U. Olsbye, M. Tilset, C. Larabi, E.A. Quadrelli, F. Bonino, K.P. Lillerud, Synthesis and stability of tagged UiO-66 Zr-MOFs, Chem. Mater. 22 (2010) 6632-6640.

[33] A.J. Howarth, Y. Liu, P. Li, Z. Li, T.C. Wang, J.T. Hupp, O.K. Farha, Chemical, thermal and mechanical stabilities of metal–organic frameworks, Nat. Rev. Mater. 1 (2016) 15018.

[34] C.G. Piscopo, A. Polyzoidis, M. Schwarzer, S. Loebbecke, Stability of UiO-66 under acidic treatment: Opportunities and limitations for post-synthetic modifications, Microporous Mesoporous Mater. 208 (2015) 30-35.

[35] M. Amin, M.A. El-Amir, H.E. Ramadan, H. El-Said, ^{99}Mo/^{99m}Tc generators based on aluminum molybdate gel matrix prepared by nano method, J. Radioanal. Nucl. Chem. 318 (2018) 915-922.

[36] Y. Wang, N. Zhang, D. Chen, D. Ma, G. Liu, X. Zou, Y. Chen, R. Shu, Q. Song, W. Lv,

Facile synthesis of acid-modified UiO-66 to enhance the removal of Cr(VI) from aqueous solutions, Sci. Total. Environ. 682 (2019) 118-127.

[37] J. P. Perdew, K. Burke, M. Ernzerhof, generalized gradient approximation made simple, Phys. Rev. Lett. 77 (1996) 3865-3868.

[38] G. Kresse, J. Furthmuller, Efficiency of Ab-initio total energy calculations for metals and semiconductors using a Plane-Wave Basis set, Comput. Mater. Sci. 6 (1996) 15-50.

[39] P. E. Blochl, Projector Augmented-Wave method, Phys. Rev. B Condens. Matter. 50 (1994) 17953-17979.

[40] S. Grimme, J. Antony, S. Ehrlich, H. Krieg, A consistent and accurate Ab Initio parametrization of density functional dispersion correction (DFT-D) for the 94 elements H-Pu, J. Chem. Phys. 132 (2010) 154104.

[41] M. K. Aydinol, A. F. Kohan, G. Ceder, K. Cho, J. Joannopoulos, Ab Initio study of lithium intercalation in metal oxides and metal dichalcogenides, Phys. Rev. B 56 (1997) 1354-1365.

[42] J. Wei, W. Zhang, W. Pan, C. Li, W. Sun, Experimental and theoretical investigations on Se(IV) and Se(VI) adsorption to UiO-66-Based metal-organic frameworks, Environ. Sci.: Nano 5 (2018) 1441-1453.

[43] H.R. Abid, H.M. Ang, S. Wang, Effects of ammonium hydroxide on the structure and gas adsorption of nanosized Zr-MOFs (UiO-66), Nanoscale. 4 (2012) 3089-3094.

[44] P. Yang, Q. Liu, J. Liu, H. Zhang, Z. Li, R. Li, L. Liu, J. Wang, Interfacial growth of a metal–organic framework (UiO-66) on functionalized graphene oxide (GO) as a suitable seawater adsorbent for extraction of uranium (VI), J. Mater. Chem. A 5 (2017) 17933-17942.

[45] P.C. Lemaire, D.T. Lee, J. Zhao, G.N. Parsons, Reversible low-temperature metal node distortion during atomic layer deposition of Al_2O_3 and TiO_2 on UiO-66-NH_2 metal-organic framework crystal surfaces, ACS Appl. Mater. Interfaces. 9 (2017) 22042-22054.

[46] M.N. Timofeeva, V.N. Panchenko, J.W. Jun, Z. Hasan, M.M. Matrosova, S.H. Jhung, Effects of linker substitution on catalytic properties of porous zirconium terephthalate UiO-66 in acetalization of benzaldehyde with methanol, Appl. Catal. A-Gen 471 (2014) 91-97.

[47] H. Saleem, U. Rafique, R.P. Davies, Investigations on post-synthetically modified UiO-66-NH_2 for the adsorptive removal of heavy metal ions from aqueous solution, Microporous Mesoporous Mater. 221 (2016) 238-244.

[48] A. Davantes, G. Lefevre, In situ real time infrared spectroscopy of sorption of

(poly)molybdate ions into layered double hydroxides, J. Phys. Chem. A. 117 (2013) 12922-12929.

[49] J. Serrano Gómez, F. Granados Correa, ^{99m}Tc generator with hydrated MnO_2 as adsorbent of ^{99}Mo, J. Radioanal. Nucl. Chem. 254 (2002) 625-628.

[50] Q. Qazi, M. Ahmad, Preparation and evaluation of hydrous titanium oxide as a high affinity adsorbent for molybdenum (^{99}Mo) and its potential for use in ^{99m}Tc generators, Radiochim. Acta. 99 (2011) 231-235.

[51] I. Saptiama, Y.V. Kaneti, H. Oveisi, Y. Suzuki, K. Tsuchiya, K. Takai, T. Sakae, S. Pradhan, M.S.A. Hossain, N. Fukumitsu, K. Ariga, Y. Yamauchi, Molybdenum adsorption properties of alumina-embedded mesoporous silica for medical radioisotope production, Bull. Chem. Soc. Jpn. 91 (2018) 195-200.

[52] T.W. Fasih, T.M. Sakr, R.R. Ayoub, M. Amin, Preparation and evaluation of nano-crystalline titania as sorbent for $^{99}Mo/^{99m}Tc$ generator, Sep. Sci. Technol. 51 (2016) 2115-2121.

[53] R. Chakravarty, R. Ramu, D. Ashutosh, Comparative assessment of nanostructured metal oxides: A potential step forward to develop clinically useful $^{99}Mo/^{99m}Tc$ generators using (n, γ) ^{99}Mo, Sep. Sci. Technol. 49 (2014) 1825-1837.

[54] R. Chakravarty, R. Shukla, S. Gandhi, R. Ram, A. Dash, M. Venkatesh, A.K. Tyagi, Polymer embedded nanocrystalline titania sorbent for $^{99}Mo/^{99m}Tc$ generator, J. Nanosci. Nanotechnol. 8 (2008) 4447-4452.

[55] X. Zhu, B. Li, J. Yang, Y. Li, W. Zhao, J. Shi, J. Gu, Effective adsorption and enhanced removal of organophosphorus pesticides from aqueous solution by Zr-based MOFs of UiO-67, ACS Appl. Mater. Interfaces. 7 (2015) 223-31.

[56] N.T. Thao, N.D. Trung, D.V. Long, Activity of molybdate-intercalated layered double hydroxides in the oxidation of styrene with air, Catal. Lett. 146 (2016) 918-928.

[57] L. Huang, J.W. Xiang, W. Zhang, C.J. Chen, H.H. Xu, Y.H. Huang, 3D interconnected porous $NiMoO_4$ nanoplate arrays on Ni foam as high-performance binder-free electrode for supercapacitors, J. Mater. Chem. A 3 (2015) 22081-22087.

[58] D. Ghosh, S. Giri, C.K. Das, Synthesis, characterization and electrochemical performance of graphene decorated with 1D $NiMoO_4 \cdot n\ H_2O$ nanorods, Nanoscale. 5 (2013) 10428-10437.

[59] J. Xu, S. He, H. Zhang, J. Huang, H. Lin, X. Wang, J. Long, Layered metal-organic

framework/graphene nanoarchitectures for organic photosynthesis under visible light, J. Mater. Chem. A 3 (2015) 24261-24271.

[60] J. Yang, Y. Dai, X. Zhu, Z. Wang, Y. Li, Q. Zhuang, J. Shi, J. Gu, Metal-organic frameworks with inherent recognition sites for selective phosphate sensing through their coordination-induced fluorescence enhancement effect, J. Mater. Chem. A. 3 (2015) 7445-7452.

[61] C. Chen, D. Chen, S. Xie, H. Quan, X. Luo, L. Guo, Adsorption behaviors of organic micropollutants on zirconium metal-organic framework UiO-66: analysis of surface interactions, ACS Appl. Mater. Interfaces. 9 (2017) 41043-41054.

[62] J. J. Cruywagen, Protonation, Oligomerization, and Condensation Reactions of Vanadate (V), Molybdate (VI), and Tungstate (VI), Adv. Inorg. Chem. 49 (1999) 127-182.

[63] C. Tian, J. Zhao, X. Ou, J. Wan, Y. Cai, Z. Lin, Z. Dang, B. Xing, Enhanced adsorption of P-Arsanilic acid from water by amine-modified UiO-67 as examined using extended X-Ray absorption fine structure, X-Ray photoelectron spectroscopy, and density functional theory calculations. Environ. Sci. Technol. 52 (2018) 3466-3475.

[64] R.J. Drout, K. Otake, A.J. Howarth, T. Islamoglu, L. Zhu, C. Xiao, S. Wang, O.K. Farha, Efficient capture of perrhenate and pertechnetate by a mesoporous Zr metal–organic framework and examination of anion binding motifs. Chem. Mater. 30 (2018) 1277-1284.

[65] O.B. Berryman, V.S. Bryantsev, D.P. Stay, D.W. Johnson, B.P. Hay, Structural criteria for the design of anion receptors: the interaction of halides with electron-deficient arenes, J. Am. Chem. Soc. 129 (2007) 48-58.

[66] V.S. Bryantsev, B.P. Hay, Are C-H Groups significant hydrogen bonding sites in anion receptors? benzene complexes with Cl^-, NO_3^-, and ClO_4^-. J. Am. Chem. Soc. 127 (2005) 8282-8283.

[67] J.T. Damron, J. Ma, R. Kurz, K. Saalwachter, A.J. Matzger, A. Ramamoorthy, The influence of chemical modification on linker rotational dynamics in metal-organic frameworks, Angew. Chem. Int. Ed. Engl. 57 (2018) 8678-8681.

[68] W. Danowski, T. van Leeuwen, S. Abdolahzadeh, D. Roke, W.R. Browne, S.J. Wezenberg, B.L. Feringa, Unidirectional rotary motion in a metal-organic framework, Nat. Nanotechnol. 14 (2019) 488-494.

[69] Sodium Pertechnetate (^{99m}Tc) Injection (Non-Fission): Final text for addition to the International Pharmacopoeia, World Health Organization Document, 2009.

Supporting Information

S-1. Materials

Formic acid (>98%), hydrochloric acid, 1,4-benzenedicarboxylate (BDC, 98%), 2-aminoterephthalic acid (99%), 2-nitroterephthalic acid (≥99%) and N,N-dimethylformamide (DMF, 99.8%) were purchased from Sigma Aldrich. Zirconium (IV) chloride (≥99.5%) and molybdenum oxide (≥99.95%) were obtained from Alfa Aesar. Deionized water was prepared with the in-house Mili-Q system from Millipore. All chemical reagents were applied directly without further purification.

S-2. Synthesis of UiO-66 analogs

UiO-66. Typically, 125 mg of ZrCl$_4$ was dissolved into a solution containing 5 mL DMF and 1 mL HCl. Then, the resultant solution was treated with sonication for 20 min, followed by adding 10 mL DMF and 123 mg BDC. Subsequently, the mixture solution was heated at 80 ºC for 24 h in an electric oven. The resulting product was washed three times with DMF and ethanol, respectively. Finally, the collected powder was placed into an oven to dry overnight at 120 ºC.

UiO-66-NH$_2$. 0.834 g of ZrCl$_4$ and 0.544 g of 2-aminoterephalic acid were added into 45 mL DMF solution and the mixture solution was stirred magnetically for 30 min at room temperature. Subsequently, the mixture solution was transferred into a Teflon-lined autoclave and heated at 120 ºC for 24 h. After cooling to room temperature, the final product was rinsed with DMF and ethanol 3 times, respectively. Finally, the yellow powder was collected and dried at 80 ºC overnight.

Form-UiO-66. Briefly, 0.431 g of ZrCl$_4$, 0.307 g of BDC and 17 mL of formic acid were added sequentially into deionized water (0.1 mL). After stirring 10 min, 50 mL DMF was injected into the above mixture for 30 min and then transferred to an autoclave that was heated at 120 ºC for 3 days. The precipitation was purified with DMF for 6 times and dried overnight at 120 ºC.

UiO-66-NO$_2$. 0.375 g of ZrCl$_4$ and 0.378 g of 2-nitroterephalic acid were dissolved in 45 mL DMF under magnetic stirring for 30 min at room temperature. Then the mixture was reacted at 80 ºC for 12 h and 100 ºC for 24 h in an electric oven. The white product was rinsed with

DMF and ethanol for 3 times, respectively and dried at 80 ℃ overnight.

S-3. Adsorption models

Generally, the Langmuir model is suitable for homogeneous adsorption that occurs in monolayer. The linear mathematical equation is expressed in Eq. (1).

$$\frac{C_e}{q_e} = \frac{1}{Q_m} C_e + \frac{1}{Q_m K_L} \qquad (1)$$

Where K_L is the Langmuir adsorption constant, related to the adsorption affinity. q_e (mg/g) and Q_m (mg/g) are correspondingly the adsorption amount at equilibrium and maximum adsorption capacity. C_e (mg/mL) is the molybdenum concentration at equilibrium.

The Freundlich model assumes that the adsorption occurs as a multilayer on a heterogeneous surface. The liner form of this model can be described in Eq. (2).

$$ln q_e = \frac{1}{n} ln C_e + ln K_F \qquad (2)$$

Where K_F is the Freundlich constant and 1/n is the heterogeneity factor describing the adsorption intensity.

S-4. Evaluation of the performance of Form-UiO-66 as sorbents in the ^{99}Mo/^{99m}Tc generator

Preparation of the column

About 200 mg of Form-UiO-66 powder was brought into a Teflon column with a filter at the bottom and the sorbent was gently pressed. Then some cotton wool was placed on the top and the column was sealed with a stopper, as shown in figure S2.1. The column was pre-treated with 50 ml of HCl solution (pH=3) at a flow rate of 0.5 ml/min before loading ^{99}Mo.

Preparation of the ^{99}Mo solution

^{99}Mo was obtained by neutron capture of ^{98}MoO$_3$ using the reactor facilities of the Institute for Energy Security and Environmental Safety Centre for Energy Research, Hungary. About 330 mg of irradiated [^{99}Mo]MoO$_3$ (~504 MBq) and 420 mg of non-radioactive MoO$_3$ were dissolved in 40 ml NaOH solution (1 M) at room temperature under magnetic stirring. Then, the pH of the solution was adjusted to 3 using HCl. Finally, the total volume of molybdenum solution was adjusted to 50 ml using stock solution (pH=3). The final concentration of obtained ^{99}Mo solution was 10 mg/mL.

Dynamic adsorption capacity

The column was fed with 24 ml of prepared solution within 8 h at a flow rate of 0.05 ml/min. After loading, the eluted solution was collected. The activity of eluted solution was measured using an automatic gamma counter (Wallac Wizard 2480, PerkinElmer). The dynamic adsorption capacity was calculated by the following equation:

$$C_d = \frac{(A_0 - A_1) \times V \times C_0}{A_0 \times m} \tag{3}$$

Where, A_0 and A_1 are the radioactivity of ^{99}Mo solution in 1 mL before and after sorption, respectively C_0 is the concentration of ^{99}Mo solution, V is the volume of solution and m is the mass (mg) of the sorbent.

The practical dynamic adsorption capacity

In order to remove the molybdenum that was not tightly adsorbed on the adsorbent, 100 ml of saline solution was passed through the column with a flow rate of 0.15 ml/min and the total activity of the effluent (A_2) was measured by the gamma counter. Then the practical dynamic adsorption capacity was calculated by the following equation:

$$C_p = \frac{[(A_0 - A_1) \times V - A_2] \times C_0}{A_0 \times m} \tag{4}$$

Elution efficiency and breakthrough

^{99m}Tc was regularly eluted from the column with 5 mL of saline solution and the performance of the generator was evaluated for 6 days. The activity of ^{99m}Tc and ^{99}Mo (141 keV for ^{99m}Tc and 740 keV for ^{99}Mo) in each eluted fraction was measured using the gamma counter. The detection efficiency of the gamma counter for ^{99m}Tc and ^{99}Mo are 70% and 1%, respectively. The elution efficiency was calculated as:

[^{99m}Tc activity in the eluted fraction]/ [expected ^{99m}Tc activity]

Expected ^{99m}Tc activity was calculated by the total amount of loaded ^{99}Mo on the column and the following formula.

$$A_2 = 0.88(\frac{\lambda_2}{\lambda_2 - \lambda_1})A_1^0 \left(e^{-\lambda_1 t} - e^{-\lambda_2 t} \right) \tag{5}$$

A_2 is the activity of the daughter (^{99m}Tc) and A_1^0 is the activity of parent (^{99}Mo) at the time of last elution; λ_1 is the decay constant of parent ($\frac{ln2}{66}$=0.0105) and λ_2 is the decay constant of the parent ($\frac{ln2}{6}$=0.1155); t is the time since the last elution and 0.88 represents the fraction of ^{99}Mo that decays to ^{99m}Tc (the other 12% directly decays to Tc-99). Finally, the formula was simplified to the following equation:

$$A_2 = 0.96 A_1^0 (1 - e^{-0.105t}) \tag{6}$$

To determine the presence of Zr and Mo contamination, the concentration in the eluted fraction was measured by inductively coupled plasma optical emission spectroscopy (ICP-OES) after the decay of ^{99}Mo. Therefore, zirconium breakthrough refers to the zirconium concentration in the eluted fraction in ppm and molybdenum breakthrough refers to the molybdenum concentration in the eluted fraction in ppm.
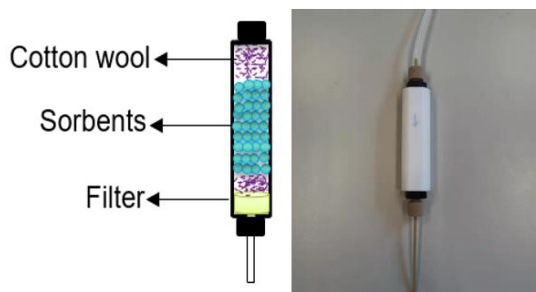

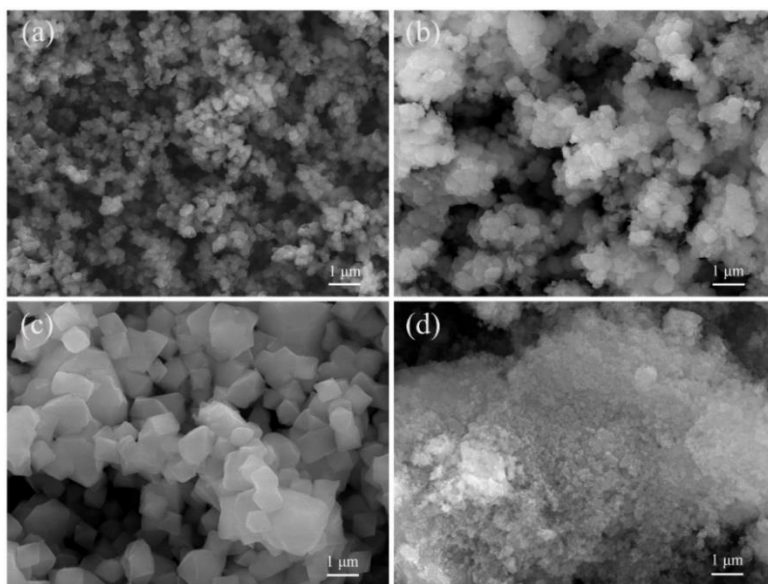**Figure S2.1.** Schematic diagram (left) and a photo (right) of the Teflon column

Figure S2.2. SEM images of a) UiO-66, b) UiO-NH$_2$, c) Form-UiO-66 and d) UiO-66-NO$_2$ before adsorption.

The morphology of UiO-66, UiO-66-NH$_2$, Form-UiO-66 and UiO-66-NO$_2$ particles is shown in Figure S2.2. From Figure S2.2 (a) and (b), it can be seen that UiO-66 and UiO-66-NH$_2$ samples show spheroidal shape with an average diameter of approximately 350 nm. The Form-UiO-66 sample displays regular-dispersed crystals with an octahedral morphology and

a mean size of around 800 nm, which is similar to previously reported. Fig. S2.2 (d) displays a rough surface of UiO-66-NO_2 that is composed of small particles.
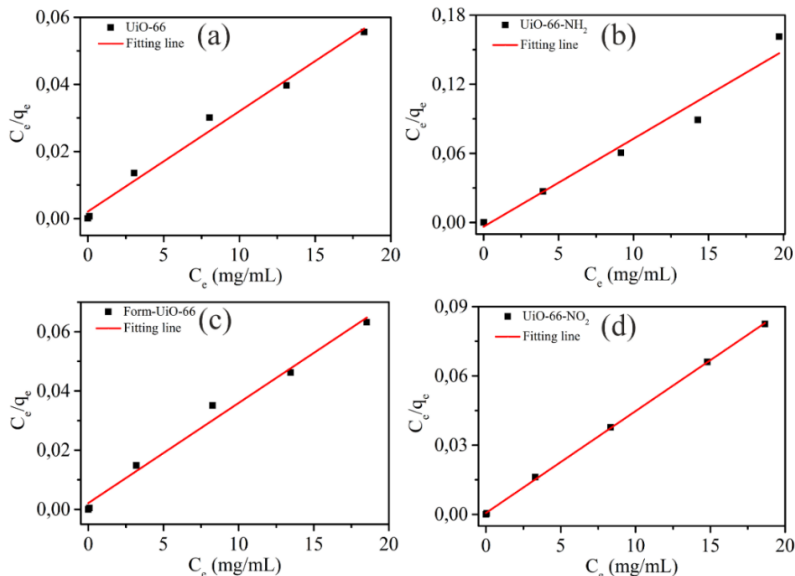

Figure S2.3. Langmuir model fitting results of (a) UiO-66, (b) UiO-66-NH_2 (c) Form-UiO-66 and (d) UiO-66-NO_2
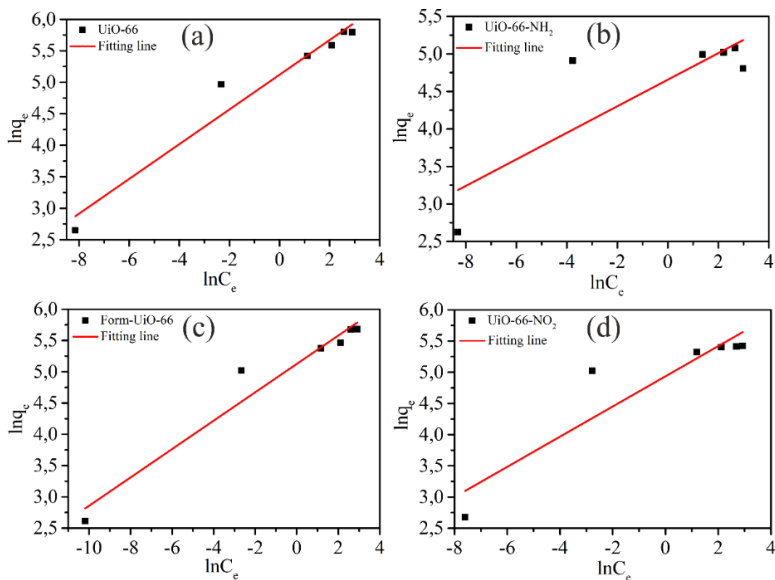

Figure S2.4. Freundlich fitting results of (a) UiO-66, (b) UiO-66-NH_2 (c) Form-UiO-66 and (d) UiO-66-NO_2
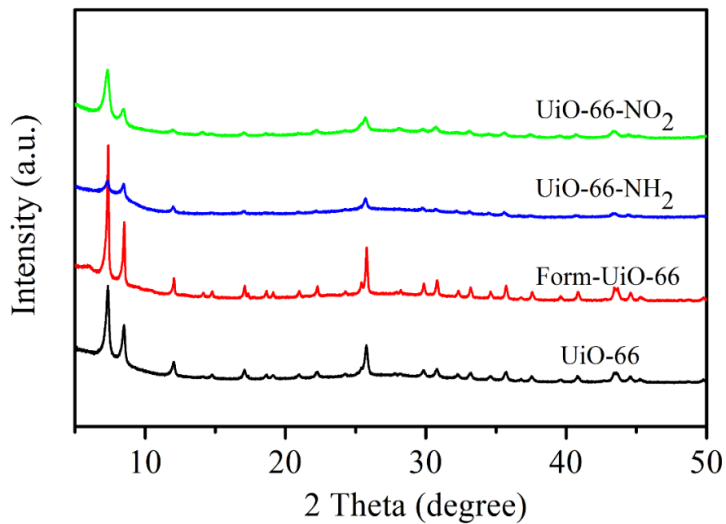
Figure S2.5. XRD pattern of UiO-66 and its derivatives after adsorption
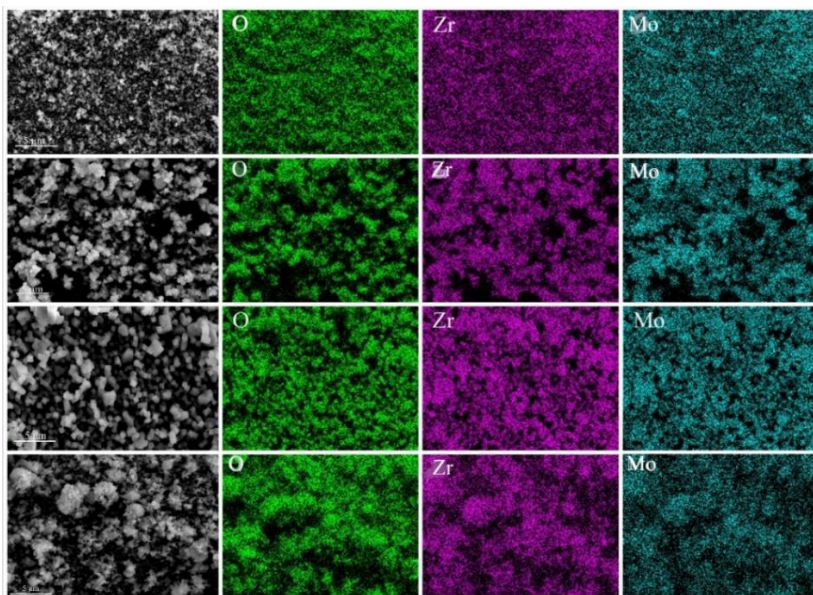

Figure S2.6. SEM images and EDS mapping of (a) UiO-66, (b) UiO-66-NH₂ (c) Form-UiO-66 and (d) UiO-66-NO₂ after Mo adsorption
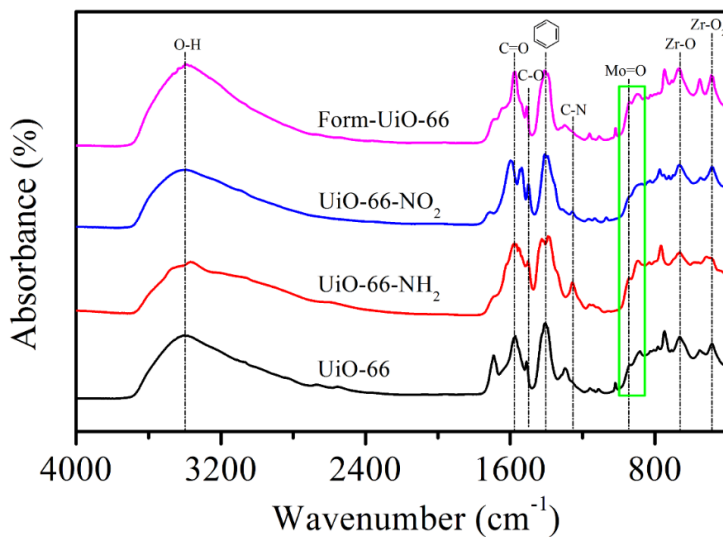
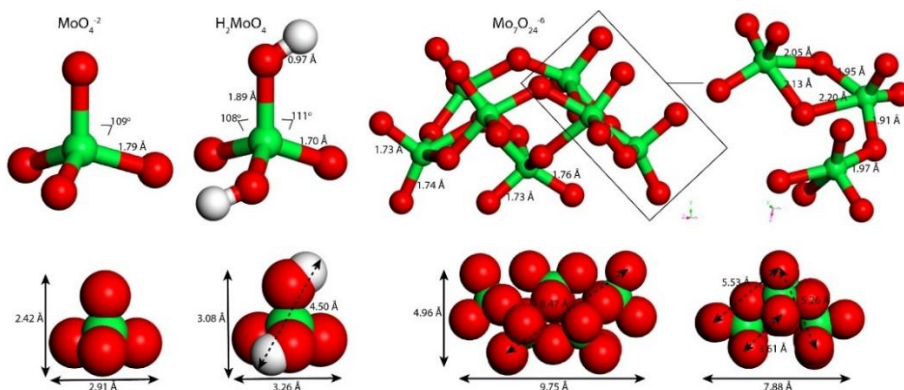**Figure S2.7.** FT-IR spectra of UiO-66 and its derivatives after adsorption

Figure S2.8. The optimized geometries (top row) and sizes (bottom row) of the molybdenum species. Green, red and white spheres are Mo, O and H, respectively.

Figure S2.9. Relaxed structure of H_2MoO_4 adsorption within the UiO-66 and UiO-66-NH$_2$ host structures. a) Near position A, the hydrogen is bonded to the O-Zr. b) Near position A, both hydrogens are in the vicinity of the oxygens of the Zr-core. c) position B. d) e) and f) adsorption near the pore walls of the linkages. All the atom distances between the adsorbent and host for the d, e and f cases are above 2.55 Å.

Figure S2.10. Triple binding spot of H_2MoO_4 in UiO-66-NH$_2$. The indicated interatomic distances are in Å.

Figure S2.11. Formation of C-O-H bonds in the linkages upon insertion of $Mo_7O_{24}^{-6}$ in the UiO-66 host.

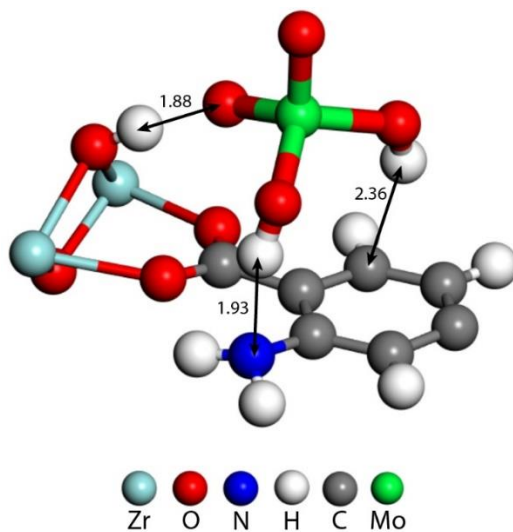**Table S2.1.** Surface area and pore sizes of UiO-66, UiO-66-NH$_2$, Form-UiO-66 and UiO-66-NO$_2$

Samples	BET (m^2/g)	V (cm^3/g)
UiO-66	1624	0.59
Form-UiO-66	1653	0.61
UiO-66-NH$_2$	295	0.11
UiO-66-NO$_2$	575	0.19

Table S2.2. All calculated parameters using the Langmuir and Freundlich model

Samples	Langmuir Parameters			Freundlich Parameters		
	Q$_m$	K$_L$ (mL/mg)	R^2	1/n	K$_F$ (mL/mg)	R^2
UiO-66	335	1.43	0.984	0.27	167	0.946
UiO-66-NH$_2$	131	2.08	0.965	0.18	105	0.642
Form-UiO-66	296	1.61	0.985	0.23	168	0.942
UiO-66-NO$_2$	227	7.58	0.999	0.24	139	0.822

Porphyrinic metal-organic frameworks as molybdenum adsorbents for the ^{99}Mo/^{99m}Tc generator

3

Abstract

Two porphyrinic metal-organic frameworks (PCN-222 and PCN-224) were prepared and their potential as adsorbents for the $^{99}Mo/^{99m}Tc$ generator was explored. The molybdenum adsorption properties of the two adsorbents, including adsorption kinetics and equilibrium isotherms, were evaluated at different molybdenum concentrations and pH. The maximum adsorption capacity of PCN-222 and PCN-224 was 525 mg/g and 455 mg/g, respectively. The possible adsorption mechanism was investigated by X-ray Photoelectron Spectra and Fourier-Transform Infrared Spectroscopy. The results demonstrated that molybdenum species were adsorbed on the two MOFs through electrostatic attraction and hydrogen bonds. In the case of PCN-222, the Mo-O-Zr coordination interaction also played an important role. Additionally, the elution performance of two $^{99}Mo/^{99m}Tc$ generators developed by using PCN-222 and PCN-224 as adsorbents was measured to assess possible clinical applications. The PCN-222-based $^{99}Mo/^{99m}Tc$ generator exhibited better elution performance and showed that around 56% of ^{99m}Tc could be obtained without zirconium breakthrough when relatively high pH solutions were used (pH=9.6).

3.1. Introduction

Technetium-99m (^{99m}Tc) is the most utilized radionuclide in nuclear medicine, being applied in more than 30 million diagnostic procedures annually all over the world [1, 2]. The huge demand is attributed to its low gamma energy emission and short half-life (6 h), which allow for diagnosis without exposing patients to high radiation dose. The rich chemistry of technetium further facilitates the preparation of various diagnostic radiopharmaceuticals. In addition, ^{99m}Tc can be produced by the β^- decay of Molybdenum-99 (^{99}Mo) from the $^{99}Mo/^{99m}Tc$ generator, which provides a convenient and reliable supply of this radionuclide in nuclear medicine departments all over the world [3].

Currently, most of the ^{99}Mo is produced by the fission of enriched uranium-235 in six nuclear reactors worldwide [4]. Unfortunately, the reliability of ^{99}Mo production has been affected in the past few years due to sudden shutdowns and maintenance of some reactors, leading to a global ^{99}Mo supply shortage in 2009 [5]. In addition, this route has a ^{99}Mo yield of 6.1%, producing a huge amount of nuclear waste [6, 7]. Due to these main problems, alternative production routes for the production of ^{99}Mo have been explored, such as the (n, γ) and (γ, n) reactions from ^{98}Mo and ^{100}Mo respectively. if those routes became a reality, more than 75 research reactors and many accelerators worldwide could be utilized to produce ^{99}Mo [8, 9]. However, ^{99}Mo produced by (n, γ) and (γ, n) reactions has low specific activity and the commercial generator material cannot be used because of the low adsorption capacity of the alumina column (2~20 mg/g) currently used [10]. There are two options to overcome this limitation. One of the solutions is increasing the amount of adsorbent and the other one is exploring new adsorbents with higher adsorption capacity. Using more adsorbent is not a desired option, since it will increase the size of the generator causing more shielding and costs. Furthermore, large elution volumes will produce ^{99m}Tc with low concentration, which complicates its medical application. Therefore, it is necessary to develop adsorbents with a higher adsorption capacity. Many efforts have been carried out to implement the use of low specific activity ^{99}Mo by investigating porous materials with good adsorption properties. Some traditional materials such as mesoporous Al_2O_3 [11], Al-TUD-1 [12], TiO_2 [13], ZrO_2 and CeO_2 [14-16] were researched as adsorbents to develop a $^{99}Mo/^{99m}Tc$ generator. In all cases, improved molybdenum adsorption capacities (50~230 mg/g) with acceptable ^{99m}Tc elution efficiency have been achieved. However, these new adsorbents still have limited

surface area and adsorption sites, which restricts fabricating clinical-grade [99]Mo/^{99m}Tc generator for widespread application in nuclear medicine. Hence, the development of new-generation adsorbents with higher adsorption capacity is very meaningful and necessary to realize a generator available for clinical application using low specific activity [99]Mo.

Metal-organic frameworks (MOFs) have gained considerable attention and exhibit excellent prospects in many applications, including purification [17, 18], drug delivery [19], adsorption and separation [20, 21] because of their high surface area, easily to functionalize cavities and controlled porosity [22, 23]. Our previous work showed that UiO-66 MOF is a great adsorbent for the preparation of [99]Mo/^{99m}Tc generator [24]. Based on the previous promising results we attempted to further increase the adsorption capacity using MOFs. We choose two zirconium MOFs (PCN-222 and PCN-224) due to their higher surface area and bigger pore sizes, which were expected to result in the high loading of molybdenum ions while retaining their high chemical stability.
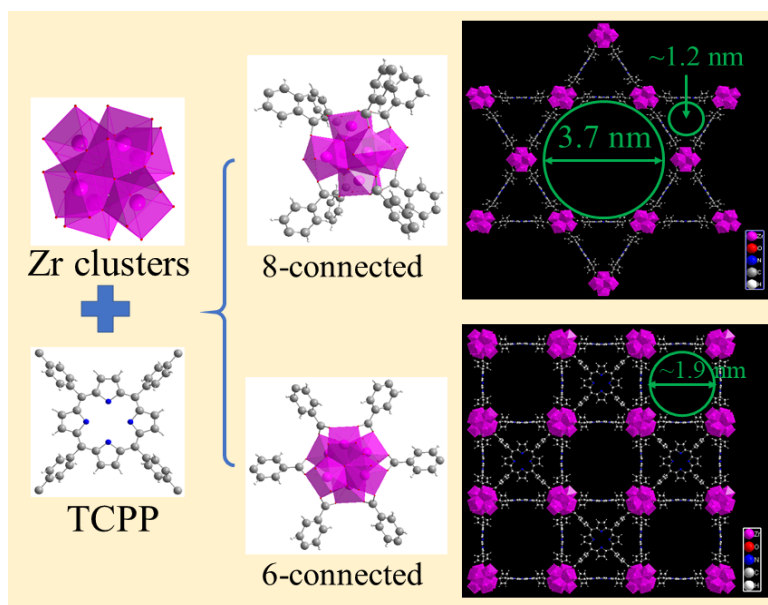

Fig. 3.1. The crystallographic structures of PCN-222 and PCN-224. Color: C, gray; O, red; H, white; N, blue; Zr, pink.

Although the structures of PCN-222 and PCN-224 are based on tetra(4-carboxyphenyl) porphyrin (TCPP) linker, they have 8 and 6 linker coordination with Zr_6 clusters, respectively. PCN-222 has two types of pores, i.e. micropores with a diameter of ~1.2 nm and mesopores

with a diameter of ~3.7 nm, while PCN-224 has only micropores with a diameter of ~1.9 nm (as shown in Fig. 3.1). In this work, we synthesized the two MOFs and evaluated their Mo adsorption performance including kinetics, isotherms and capacity at different Mo concentrations and pH. Furthermore, the adsorption mechanism was also investigated by XPS and FT-IR to reveal the interaction between Mo species and the adsorbents. Finally, adsorption batch experiments using ^{99}Mo were carried out to determine their potential as adsorbents for $^{99}Mo/^{99m}Tc$ generator.

3.2. Experimental section

3.2.1 Materials

All chemical reagents were ordered from the indicated suppliers and used without further purification. Zirconium (IV) chloride (≥99.5%) was purchased from Alfa Aesar. N, N-dimethylformamide (DMF, 99.8%), benzoic acid (≥99.5%), Tetrakis(4-carboxyphenyl) porphyrin (97%) were purchased from Sigma Aldrich.

3.2.2 Synthesis of PCN-222 and PCN-224

PCN-222 was synthesized based on previous literature with a few modifications using the solvothermal method [25, 26]. First, 150 mg of $ZrOCl_2·8H_2O$ (465 μmol) was added to 40 ml of DMF by magnetic stirring for 30 min and 116 mg of TCPP (147 μmol) was added afterward. Then, 19 ml of formic acid solution was introduced and the mixture was further stirred for 15 min. Finally, the solution was transferred to a Teflon-lined autoclave and heated at 130 °C for 3 days. After cooling down to room temperature, the precipitates were collected and washed with DMF and acetone for three times, respectively. The final product was dried at room temperature.

The synthesis of PCN-224 was prepared according to previous research [27]. Briefly, 30 mg of $ZrCl_4$, 10 mg of TCPP and 400 mg of benzoic acid were ultrasonically dissolved for 20 min in 2 ml of DMF. Then the solution was heated at 120 °C for 24 h by an electric furnace. After cooling to room temperature, the precipitation was washed with DMF and acetone three times, respectively. Finally, the sample was immersed in acetone for over 12 h and dried at 80 °C for 6 h under vacuum.

3.2.3　Characterization

Powder X-ray diffraction was collected with PANalytical X'Pert Pro pw3040/60 diffractometer equipped with Cu Kα radiation under the condition of 45 kV and 40 mA. Nitrogen adsorption at 77 K was performed using a Micromeritics Tristar II and the samples were pre-treated at 150 °C for 16 h under vacuum before measurement. Fourier-transform infrared spectroscopy (FT-IR) was carried out by a NICOLET 6700 instrument in a wavenumber range of 400~4000 cm^{-1} at room temperature. The crystal morphology was observed using a field emission scanning electron microscopy and elemental composition was measured with an energy dispersive spectrometer (EDS, JEOL ISM-IT100). The zeta potential was collected in a pH range of 2-10 to determine the surface charge of adsorbents by a Malvern ZetaSizer nano-ZS instrument. The suspension was prepared by dispersing 0.3±0.1 mg of sample into 1 ml of solutions with different pH values. The concentration of the different molybdenum solutions was determined by inductively coupled plasma optical emission spectroscopy (ICP-OES, Optima 4300, Perkin and Elmer). The chemical states of composing elements of MOFs were analyzed by K-Alpha X-ray photoelectron spectra (XPS, ThermoFisher scientific).

3.2.4　Molybdenum adsorption

Molybdenum adsorption isotherms of PCN-222 and PCN-224 were carried out at different pH (2~9) and initial molybdenum concentrations (0.1~20 mg/mL) by batch experiments. The stock solution was prepared by dissolving 3 g of MoO_3 into 1.8 g of NaOH (1M) solution and the pH of the solution was adjusted to predetermined values. Then, the stock solution was diluted to prepare molybdenum solutions with different concentrations. Typically, 6±0.5 mg of adsorbent was added into Eppendorf tubes containing 1 ml Mo solution with different initial concentrations. The mixture was shaken at 25 °C for 24 h by a temperature-controlled shaker with 1400 rpm. Then all Eppendorf tubes were centrifuged and the concentration in the supernatant was analyzed by ICP-OES. The molybdenum uptake of the adsorbents was determined by the following equation:

$$q_e = \frac{(C_0 - C_e) \times V}{m} \tag{1}$$

Where q_e and C_e (mg/mL) are the molybdenum uptake and concentration at equilibrium, respectively. C_0 represents the initial Mo concentration. V (mL) denotes the volume of

solution and m (mg) is the mass of adsorbent. The molybdenum adsorption kinetics and the effect of pH on adsorption were also carried out and more details can be found in the Supporting Information.

3.3 Results and discussion

3.3.1 Molybdenum adsorption studies

Effects of pH

The effects of pH on the Mo adsorption on PCN-222 and PCN-224 were conducted in a pH range of 2~10 and initial molybdenum concentration of 5 mg/mL. The results are shown in Fig. 3.2 (a). It can be observed that the molybdenum uptake of PCN-222 decreased continuously from 457 mg/g (pH=2) to 140 mg/g (pH=10) with increasing pH value. The uptake on PCN-224 decreased slightly from pH 2 (332 mg/g) to 3 (321 mg/g) and then decreased to 145 mg/g at pH 8.7.
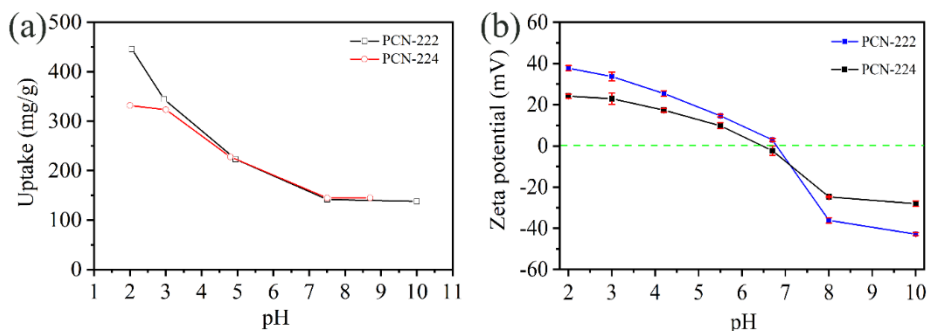

Fig. 3.2. (a) Effect of pH on the Mo adsorption of PCN-222 and PCN-224 when the initial Mo concentration was 5 mg/mL; (b) Zeta potential of PCN-222 and PCN-224 as function of pH.

The zeta potential, which reflects the surface charge of the adsorbents, is shown in Fig. 3.2 (b). The isoelectric points (IEPs) of PCN-222 and PCN-224 are between 6.5 and 7. Meanwhile, the molybdenum species present in the solution vary with the molybdenum concentration and the pH of the solution. According to previously reported literature [28], when molybdenum solution of 0.01 M is used, the major molybdenum chemical species is $Mo_7O_{24}^{6-}$ at a pH range between 2 and 5; at pH>5 the dominant species is MoO_4^{2-}. When the pH value is less than IEPs, the adsorbents have positive charges that can interact with the

negatively charged molybdenum species by electrostatic attraction. However, when the pH value is higher than IEPs, the adsorption of two adsorbents was found to be still around 140 mg/g, which suggests that chemisorption plays a role.

Adsorption kinetics

The molybdenum adsorption kinetics of PCN-222 and PCN-224 were measured with starting concentrations from 1.5 mg/ml to 20 mg/ml and the results are shown in Fig. 3.3 (a) and (b). The molybdenum adsorption uptake of PCN-222 reached equilibrium at 1 h with an uptake of ~220 mg/g when the initial molybdenum concentration was 1.5 mg/mL. The adsorption processes could reach equilibrium within 3 h when the initial molybdenum concentrations were 5 mg/mL and 10 mg/mL. With increasing molybdenum concentration (15 mg/ml and 20 mg/ml), the adsorption approached equilibrium after 5 h. This adsorption phenomenon could be attributed to the dimensions of the molybdenum species and the pore size of the adsorbent. At the initial adsorption stage, the molybdenum species would occupy the preferential adsorption sites of PCN-222. Subsequently, the large concentration gradient promotes the diffusion of molybdenum ions to the remaining adsorption sites. When the molybdenum concentration is 1mM (ca 0.1 mg/mL) at pH=3, MoO_4^{2-} is the dominate molybdenum species. When molybdenum concentration is 0.1 M (ca 10 mg/mL) at pH=3, the main molybdenum species is $Mo_8O_{26}^{4-}$. Molybdenum species with small sizes at low concentrations could rapidly diffuse into two types of pores in PCN-222. At high concentrations, molybdenum species with larger sizes would have a relatively slow rate of diffusion into pores. In comparison, the adsorption uptake of PCN-224 can reach 90 % of the total adsorption capacity within 1 hour and equilibrium within 2 hours, which appears not to be influenced much by the molybdenum concentration due to the bigger pore size in PCN-224. To further analyze the adsorption process, the pseudo-first-order and pseudo-second-order models were employed to fit the experimental data (see Supporting Information). The calculated parameters are summarised in Table S3.1 and Table S3.2. The pseudo-second kinetic model of PCN-222 and PCN-224 has higher correlation coefficient values ($R^2 > 0.999$) than the pseudo-first-order model, indicating that the Mo adsorption process can be better described by the pseudo-second kinetic model. Furthermore, the calculated adsorption capacities by the pseudo-second kinetic model are consistent with experimental data for two MOFs, which also indicates the existence of a chemisorption process.
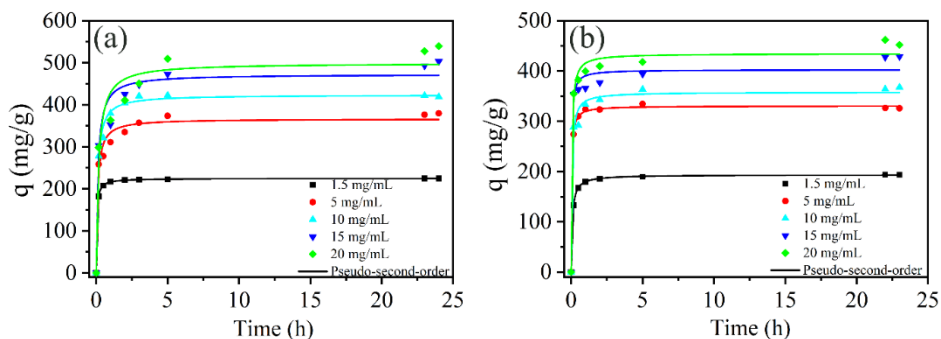
Fig. 3.3. Molybdenum adsorption kinetics of (a) PCN-222 and (b) PCN-224 at different molybdenum concentration (pH=3).
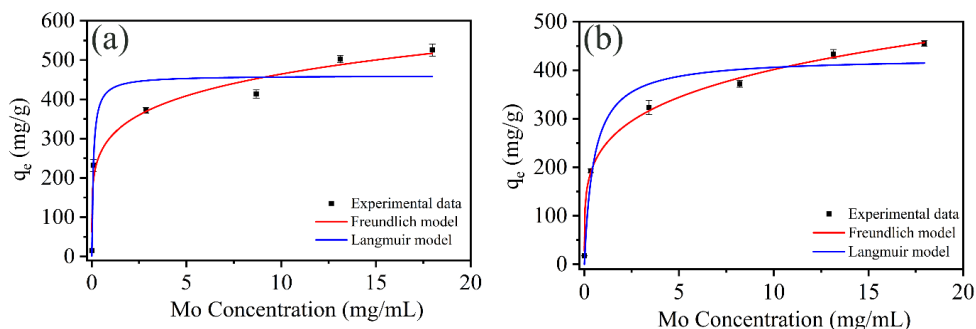

Fig. 3.4. Molybdenum adsorption isotherm of (a) PCN-222 and (b) PCN-224 at pH 3. Adsorption curves were fitted by the Langmuir (blue) and Freundlich models (red).

Molybdenum adsorption isotherms

Molybdenum adsorption isotherms of PCN-222 and PCN-224 were measured at pH 3 as the function of the equilibrium molybdenum concentration to determine the molybdenum adsorption capacity, and the results are displayed in Fig. 3.4 (a) and (b). Their molybdenum uptake increased to around 350 mg/g and can exceed 70% of the adsorption saturation value at low molybdenum concentration (C_{Mo}<5 mg/mL). The maximum molybdenum adsorption capacity of PCN-222 was determined to be around 525 mg/g, which is higher than that of PCN-224 (455 mg/g). To better estimate the adsorption behaviour, the Freundlich and Langmuir models were applied to fit the obtained data. The fitted results are depicted in Table S3.3. The R^2 values suggested that the Freundlich model could better fit the molybdenum adsorption isotherms of PCN-222 (96.1%) and PCN-224 (99.7%), which indicated that the

adsorption was multilayer adsorption on heterogeneous surface [29]. The molybdenum adsorption capacity of PCN-222 is larger than that of PCN-224, which may be attributed to its higher surface area and larger pore size than PCN-224. Moreover, both adsorbents exhibit excellent Mo adsorption performance compared to the previously reported adsorbents (Table 3.1). In addition, compared to PCN-224, UiO-66 (Zr) has a relatively lower adsorption capacity (335) because it has smaller pore sizes, which restrict the adsorption of big-sized molybdenum species. It demonstrates that pore sizes also play a key role during the molybdenum adsorption process.

Table 3.1. Summary of the static Mo adsorption capacity of various adsorbents.

Adsorbents	Mo adsorption capacity (mg/g)	Surface area (m^2/g)	Ref.
TUD-1	112	402	[12]
Hydrous MnO_2	50	--	[30]
Hydrous TiO_2	230	--	[13]
Al-dropped mesoporous SiO_2	16.8	463	[31]
Mesoporous γ-Al_2O_3	56.2	251	[32]
Nanocrystalline γ-Al_2O_3	200	252	[33]
Nano $Zr(OH)_4$ gel	292	151	[34]
Macro/mesoporousγ-Al_2O_3	250	542	[35]
$Al^{99}Mo$ gel	364	--	[36]
UiO-66 (Zr)	335	1624	[24]
Form-UiO-66	296	1653	[24]
UiO-66-NH_2	131	295	[24]
UiO-66-NO_2	227	575	[24]
UiO-66 (Ce)	475	1140	[24]
PCN-222	525	1882	This work
PCN-224	455	1467	This work

3.3.2 Molybdenum adsorption mechanism

Characterization

To observe the structural information after molybdenum adsorption, the XRD patterns of PCN-222 and PCN-224 were recorded and are shown in Fig. 3.5 (a) and (b). All diffraction peaks of PCN-222 and PCN-224 before adsorption match well with their corresponding calculated patterns [36, 37], which demonstrates that PCN-222 and PCN-224 with good crystalline structure were synthesized. After molybdenum adsorption, the intensity of the

diffraction pattern of PCN-222 was greatly decreased and the two peaks at 7.09° and 7.29° disappeared, which can be attributed to the partial occupation of the pores by Mo ions [38], causing diminishment of X-ray. At the same time, all diffraction peaks of PCN-224 disappeared after adsorption except a tiny peak at 4.6° because the material was completely saturated with adsorbed Mo, resulting in a loss of long-range order in the crystal structure of the framework.

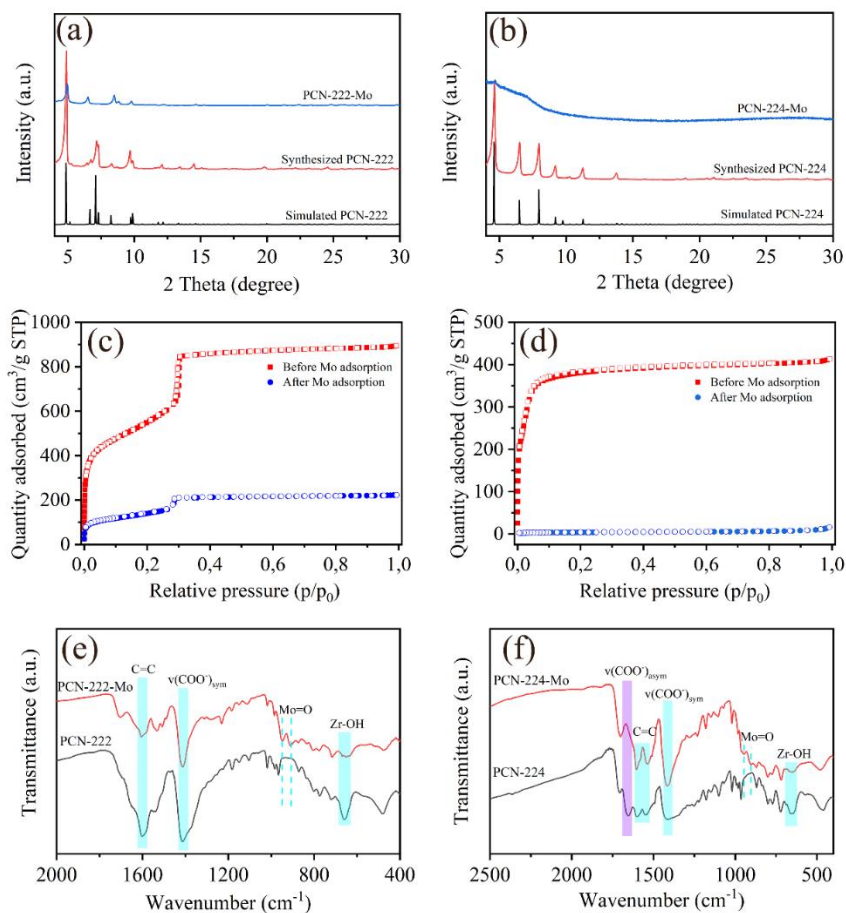**Fig. 3.5.** XRD patterns of (a) PCN-222 and (b) PCN-224; N_2 adsorption isotherms of (c) PCN-222 and (d) PCN-224; FT-IR spectra of (e) PCN-222 and (f) PCN-224 before and after molybdenum adsorption using molybdenum concentration of 20 mg/mL (pH=3).

The surface area of PCN-222 and PCN-224 was determined by the nitrogen adsorption-desorption technique, as displayed in Fig. 3.5 (c) and (d). The adsorption isotherms of PCN-

222 with a type IV curve have two plateaus at relatively lower pressure and P/P_0=0.3, corresponding to 1.2 nm micropores and 3.7 nm mesopores, respectively. While the nitrogen adsorption isotherms of PCN-224 belong to the type I curve, indicating microporosity. After molybdenum adsorption, the surface area and pore volume of PCN-222 decreased from 1882 m^2/g and 1.22 cm^3/g to 471 m^2/g and 0.31 cm^3/g, respectively (Table S3.4), which demonstrates that the molybdenum species enter the pores of PCN-222, indicating favorable molybdenum adsorption.

The relatively high residual surface area indicates that the material is not fully saturated or that there are some pores that Mo species cannot reach. The surface area and pore volume of PCN-224 before adsorption are 1467 m^2/g and 0.56 cm^3/g, respectively, which decreased to 13 m^2/g and 0.002 cm^3/g after adsorption, respectively. These results suggest that all the adsorption sites of PCN-224 were accessible and were occupied by molybdenum species.

The FT-IR spectra of PCN-222 and PCN-224 before and after adsorption are shown in Fig. 3.5 (e) and (f), respectively. Two new peaks at 908 cm^{-1} and 948 cm^{-1} for both MOFs after adsorption can be observed, demonstrating the presence of the Mo species (Mo=O) [39, 40]. The peak at 650 cm^{-1}, which is attributed to the vibration of Zr-OH, is weaken for the two materials after adsorption, indicating that there is an interaction between the Mo species and the hydroxyl groups via hydrogen bonds [24]. The peak at 966 cm^{-1} corresponding to the N-H in-plane bending vibration of pyrrolic nitrogen disappeared after Mo adsorption, suggesting an interaction between the -NH group and the Mo species [41].

To explore the possible adsorption mechanism, the surface composition and chemical states of the adsorbents were analyzed by XPS. Fig. 3.6 (a) shows the full view of the XPS spectra of PCN-222 before and after molybdenum adsorption. The primary peaks of C 1s, O 1s, N 1s and Zr 3d can be observed in PCN-222 before and after Mo adsorption. The appearance of new peaks after Mo adsorption at 231.7 eV, 234.87 eV and 415.1 eV, which are attributed to Mo $3d_{5/2}$, Mo $3d_{3/2}$ and Mo 3p, respectively (Fig. 3.6b), indicates that Mo is successfully adsorbed by the adsorbents. Fig. 3.6 (c) shows the Zr 3d spectra PCN-222, which was deconvoluted to two peaks of Zr $3d_{5/2}$ at 182.21 eV and Zr $3d_{3/2}$ at 184.58 eV [42]. After Mo adsorption, these two peaks shifted to 181.8 eV and 184.17 eV. The binding energy shifts to lower energy caused by the increased electron density on the Zr surface, which may be ascribed to the formation of Mo-O-Zr coordination bonds vis donating one pair of electrons from the Mo species [24]. The N 1s spectrum of PCN-222 before adsorption, as shown in

Fig. 3.6 (d), can be divided into two peaks at 398.95 eV and 397.16 eV, which are assigned to pyrrolic N and pyridinic N, respectively [43]. Their binding energies moved to 398.79 eV and 397.02 eV after Mo adsorption. This small energy shift indicates the weak interaction between Mo species and N atoms. Moreover, the C 1s spectra of PCN-222 (Figure S3.2) before adsorption could be divided into three peaks at 284.4 eV, 285.4 eV and 288.2 eV, which are attributed to O-C=O, C-N and C-C/C-H, respectively [44].
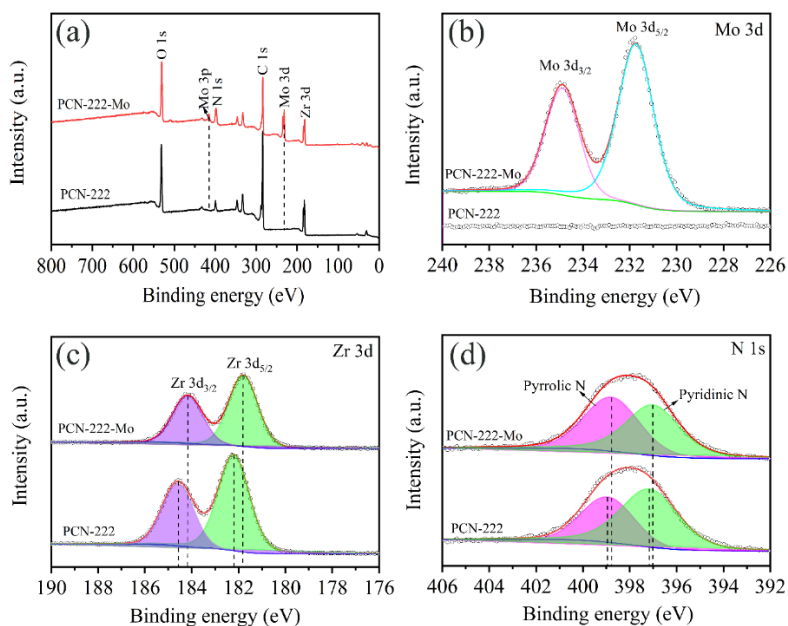

Fig. 3.6. (a) Full view XPS spectrum; (b) Mo 3d; (c) Zr 3d and (d) N 1s of PCN-222 before and after molybdenum adsorption.

The XPS survey spectra of PCN-224 before and after Mo adsorption is displayed in Fig. 3.7 (a) and the strong peaks of Mo observed for the PCN-224 after adsorption can be observed. High-resolution XPS spectra of Mo 3d is shown in Fig. 3.7 (b) and two peaks at 234.78 eV and 231.61 eV are ascribed to Mo $3d_{3/2}$ and Mo $3d_{5/2}$, respectively. Fig. 3.7 (c) shows the comparison between PCN-224 and PCN-224-Mo and no shifts can be observed, indicating that there is no charge in the redistribution of the Zr atoms. As shown in Fig. 3.7 (d), the N 1s spectra of PCN-224 can be fitted with two separate peaks, which are attributed to pyrrolic N and pyridinic N. After Mo adsorption, the peak of pyrrolic N shifted from 398.94 eV to 398.18 eV, suggesting the occurrence of interaction between Mo species and pyrrolic groups, which are consistent with the analysis of FT-IR results. In the C 1s spectra of PCN-224 (See

in Figure S3.3), the binding energy of O-C=O moved from 288.2 eV to 288.6 eV and the higher binding energy shift suggests the electron loss of this chemical bond, leading to structural change, which is consistent with the XRD and FT-IR results.
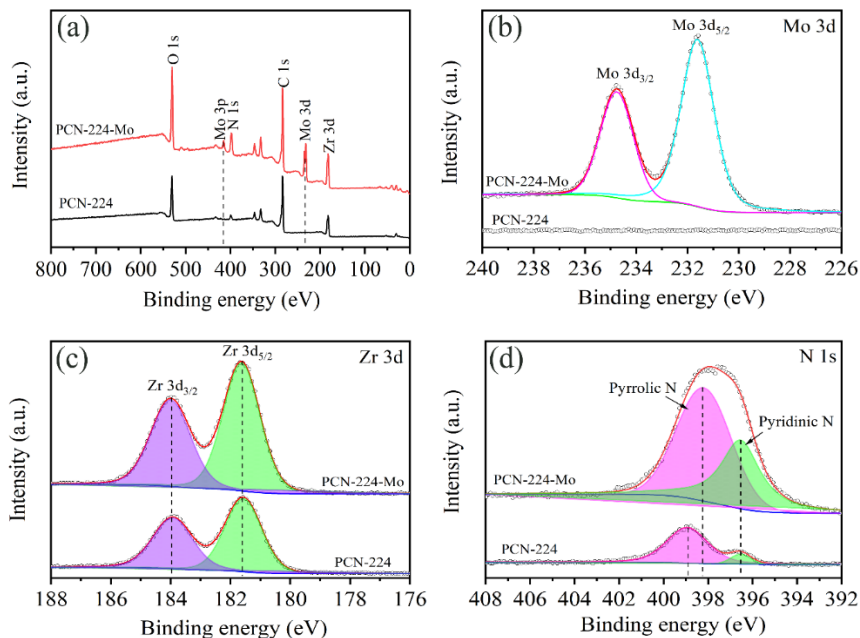

Fig. 3.7. (a) XPS survey spectra; (b) Mo 3d; (c) Zr 3d and (d) N 1s of PCN-224 before and after molybdenum adsorption.

Based on the above analysis, the possible molybdenum adsorption mechanisms seem to be derived by hydrogen bonds, electrostatic attraction and coordination interaction. The following is a summary: (1) The molybdenum species can be adsorbed through electrostatic attraction by PCN-222 and PCN-224, when $pH<pH_{PZC}$; (2) The adsorption sites on the metal clusters (hydroxyl groups) and linkers (pyrrolic N) of PCN-222 and PCN-224 serve to interact with molybdenum species through hydrogen bonds; (3) Zr-O-Mo coordination interaction only appears in PCN-222, which is probably ascribed to its higher number of hydroxyl groups ($Zr_6(\mu_3\text{-}OH)_8$) and lower volumetric density of TCPP linkers (1.9 mmol/cm^3) compared with that of PCN-224 ($Zr_6(\mu_3\text{-}O)_4(\mu_3\text{-}OH)_4$ and 3.6 mmol/cm^3) [45].

3.3.3 PCN-222 and PCN-224 as adsorbents for the ^{99}Mo/^{99m}Tc generator

To further support the feasibility of PCN MOFs in practical application, their adsorption performance in batch and column mode was examined utilizing ^{99}Mo. The results showed that the ^{99}Mo static adsorption capacity of PCN-222 and PCN-224 was 365 mg/g and 336 mg/g, respectively, when the initial Mo concentration was 5 mg/ml, which is consistent with the results obtained using non-active molybdenum. Then, the dynamic adsorption of PCN-222 and PCN-224 was determined to be 280 mg/g and 268 mg/g, respectively. These promising results indicate that high amounts of ^{99}Mo could be loaded allowing the development of ^{99}Mo/^{99m}Tc generator.

Table. 3.2. Elution parameters of PCN-222 based ^{99}Mo/^{99m}Tc generator using eluent having different pH values.

Elution No.	pH	Time of growth (h)	Elution yield (%)	^{99}Mo breakthrough (%)	Zr breakthrough (ppm)
1	6.1	24	31.3	1.9	<0.01
2		24	52.4	2.0	<0.01
3	7.9	25	45.0	2.4	<0.01
4		24	49.0	2.4	<0.01
5	9.6	23	56.4	2.2	<0.01

^{99m}Tc elution performance of PCN-222 and PCN-224 as adsorbent for ^{99}Mo/^{99m}Tc generator was subsequently evaluated. The generator was washed using saline solution (pH=6.1) after one day of ^{99m}Tc ingrowth. The detailed elution results can be found in Table S3.5 and Table S3.6. The elution yield of ^{99m}Tc for PCN-222 and PCN-224 was about 30% and 8%, respectively. The low elution yield was most likely caused by the inappropriate pH (<IEPs) of the saline solution. To improve the elution yield, saline solutions with different pH values were applied to elute the ^{99}Mo/^{99m}Tc generator fabricated with PCN-222 as shown in Table 3.2. It can be observed that the elution efficiency of ^{99m}Tc increased gradually with the increasing pH of the saline solution, reaching about 56% when the pH of the saline solution was 9.6. At the same time, the amount of ^{99}Mo was about 2 % in all eluted fractions, which is higher than the limit of 0.1% based on the requirements of the International Pharmacopoeia (IP) (World Health Organization, 2009).[46] The zirconium breakthrough was less than the ICP-OES detection limit (i.e. 10 ppb) and is not considered to be a problem. The results show that PCN-222 could be a promising candidate as molybdenum adsorbent for ^{99}Mo/^{99m}Tc generator. The higher elution efficiency and lower molybdenum breakthrough have to be

pursued by optimizing separation conditions for practical medical applications in the future.

3.4. Conclusion

PCN-222 and PCN-224 metal-organic frameworks with high surface area were synthesized and their molybdenum adsorption performance was studied at different pH and molybdenum concentrations. The maximum static molybdenum adsorption capacity of PCN-222 and PCN-224 could reach up to 525 mg/g and 455 mg/g, respectively. XPS, FT-IR and zeta potential were employed to understand the interaction between molybdenum ions and MOFs. It was demonstrated that high surface area MOFs with big porous structures can improve molybdenum adsorption capacity by electrostatic attraction, hydrogen and coordination bonds. The ^{99m}Tc elution yield of ^{99}Mo/^{99m}Tc generator using PCN-222 and PCN-224 as adsorbents was about 30% and 8%, respectively, when the pH of the saline solution was 6.1. A higher elution yield (56%) for the PCN-222 based generator can be obtained by increasing the pH of the saline solution to 9.6, but relatively high ^{99}Mo breakthrough (~2%) was observed. Future studies will be done by focusing on improving ^{99m}Tc elution yield and reducing ^{99}Mo breakthrough under different conditions so that PCN-222 possessing high molybdenum adsorption capacity can be used as adsorbent for the ^{99}Mo/^{99m}Tc generator in eventual clinical application.

References

[1] M., Pillai, A. Dash, FR. Jr. Knapp, Radionuclide generators: a ready source diagnostic and therapeutic radionuclides for nuclear medicine applications. Radiopharmaceuticals: application, insights and future, 2016 vol 63.

[2] W.C. Eckelman, Unparalleled contribution of technetium-99m to medicine over 5 decades, J. Am. Coll. Cardiol. Image 2(3) (2009) 364–368.

[3] S. Hasan, M.A. Prelas, Molybdenum-99 production pathways and the sorbents for ^{99}Mo/^{99m}Tc generator systems using (n, γ) ^{99}Mo: a review, SN Appl. Sci. 2 (2020) 1–28.

[4] M.R. Pillai, A. Dash, F.F. Knapp, Jr., Sustained availability of ^{99m}Tc: possible paths forward, J. Nucl. Med. 54(2) (2013) 313-23.

[5] R. Van Noorden, Radioisotopes: The medical testing crisis. Nature 504(7479) (2013)

202-204.

[6] T. Takeda, M. Fujiwara, M. Kurosawa, N. Takahashi, M. Tamura, T. Kawabata, Y. Fujikawa, K.N. Suzuki, N. Abe, T. Kubota, T. Takahashi, ^{99m}Tc production via the (γ, n) reaction on natural Mo, J. Radioanal. Nucl. Chem. 318(2) (2018) 811-821.

[7] J. Stillman, E. Feldman, S. Pham, D. Yoon, E. Wilson, W. Cowherd, L. Foyto, K. Kutikkad, N. Peters, Safety Analysis of the Mo-99 Production Upgrade to the University of Missouri Research Reactor (MURR) with Highly-Enriched and Low-Enriched Uranium Fuel, Argonne National Lab.(ANL), Argonne, IL (United States), 2019.

[8] M.R. Pillai, F.F. Knapp, Jr., Molybdenum-99 production from reactor irradiation of molybdenum targets: a viable strategy for enhanced availability of technetium-99m, Quat. J. Nucl. Med. Mol. Imaging 56(4) (2012) 385-399.

[9] M. Mostafa, M. Atef, M.A. El-Amir, Preparation and performance studies of ^{99}Mo/^{99m}Tc column generators based on nano zirconium molybdate, J. Radioanal. Nucl. Chem. 314(3) (2017) 1683-1694.

[10] H. Arino, H.H. Kramer, Fission product ^{99m}Tc generator, Int. J. Appl. Radiat. Isot. 26(5) (1975) 301-303.

[11] R. Chakravarty, R. Ram, R. Mishra, D. Sen, S. Mazumder, M.R.A. Pillai, A. Dash, Mesoporous Alumina (MA) Based Double Column Approach for Development of a Clinical Scale ^{99}Mo/^{99m}Tc Generator Using (n,γ)^{99}Mo: An Enticing Application of Nanomaterial, Ind. Eng. Chem. Res. 52(33) (2013) 11673-11684.

[12] A.G. Denkova, B.E. Terpstra, O.M. Steinbach, J.t. Dam, H.T. Wolterbeek, Adsorption of Molybdenum on Mesoporous Aluminum Oxides for Potential Application in Nuclear Medicine, Separ. Sci. Technol. 48(9) (2013) 1331-1338.

[13] Q.M. Qazi, M. Ahmad, Preparation and evaluation of hydrous titanium oxide as a high affinity adsorbent for molybdenum (^{99}Mo) and its potential for use in ^{99m}Tc generators, Radiochim. Acta. 99 (2011) 231.

[14] R. Chakravarty, R. Shukla, R. Ram, A.K. Tyagi, A. Dash, M. Venkatesh, Practicality of Tetragonal Nano-Zirconia as a Prospective Sorbent in the Preparation of ^{99}Mo/^{99m}Tc Generator for Biomedical Applications, Chromatographia 72(9-10) (2010) 875-884.

[15] R. Chakravarty, R. Shukla, S. Gandhi, R. Ram, A. Dash, M. Venkatesh, A.K. Tyagi, Polymer embedded nanocrystalline titania sorbent for ^{99}Mo/^{99m}Tc generator, J. Nanosci. Nanotechnol. 8(9) (2008) 4447-4452.

[16] R. Chakravarty, R. Shukla, R. Ram, M. Venkatesh, A. Dash, A.K. Tyagi, Nanoceria-PAN composite-based advanced sorbent material: a major step forward in the field of clinical-grade [68]Ge/^{68}Ga generator, ACS Appl. Mater. Interfaces 2(7) (2010) 2069-75.

[17] W.G. Cui, T.L. Hu, X.H. Bu, Metal-Organic Framework Materials for the Separation and Purification of Light Hydrocarbons, Adv. Mater. 32(3) (2020) e1806445.

[18] B.M. Jun, Y.A.J. Al-Hamadani, A. Son, C.M. Park, M. Jang, A. Jang, N.C. Kim, Y. Yoon, Applications of metal-organic framework based membranes in water purification: A review, Sep. Purif. Technol. 247 (2020) 116947.

[19] M.X. Wu, Y.W. Yang, Metal-Organic Framework (MOF)-Based Drug/Cargo Delivery and Cancer Therapy, Adv. Mater. 29(23) (2017) 1606134.

[20] G.R. Xu, Z.-H. An, K. Xu, Q. Liu, R. Das, H.-L. Zhao, Metal organic framework (MOF)-based micro/nanoscaled materials for heavy metal ions removal: The cutting-edge study on designs, synthesis, and applications, Coord. Chem. Rev. 427 (2021) 213554.

[21] S.W. Lv, J.M. Liu, C.Y. Li, N. Zhao, Z.H. Wang, S. Wang, A novel and universal metal-organic frameworks sensing platform for selective detection and efficient removal of heavy metal ions, Chem. Eng. J. 375 (2019) 122111.

[22] J. Li, X. Wang, G. Zhao, C. Chen, Z. Chai, A. Alsaedi, T. Hayat, X. Wang, Metal-organic framework-based materials: superior adsorbents for the capture of toxic and radioactive metal ions, Chem. Soc. Rev. 47(7) (2018) 2322-2356.

[23] S. Rojas, P. Horcajada, Metal-Organic Frameworks for the Removal of Emerging Organic Contaminants in Water, Chem. Rev. 120(16) (2020) 8378-8415.

[24] C. Ma, A. Vasileiadis, H.T. Wolterbeek, A.G. Denkova, P. Serra Crespo, Adsorption of molybdenum on Zr-based MOFs for potential application in the [99]Mo/^{99m}Tc generator, Appl. Surf. Sci. 572 (2022) 151340.

[25] W. Morris, B. Volosskiy, S. Demir, F. Gandara, P.L. McGrier, H. Furukawa, D. Cascio, J.F. Stoddart, O.M. Yaghi, Synthesis, structure, and metalation of two new highly porous zirconium metal-organic frameworks, Inorg. Chem. 51(12) (2012) 6443-5.

[26] J. Hynek, S. Ondrusova, D. Buzek, P. Kovar, J. Rathousky, J. Demel, Postsynthetic modification of a zirconium metal-organic framework at the inorganic secondary building unit with diphenylphosphinic acid for increased photosensitizing properties and stability, Chem. Commun. 53(61) (2017) 8557-8560.

[27] J. Park, Q. Jiang, D. Feng, L. Mao, H.C. Zhou, Size-Controlled Synthesis of Porphyrinic Metal-Organic Framework and Functionalization for Targeted Photodynamic Therapy, J. Am. Chem. Soc. 138(10) (2016) 3518-25.

[28] M. Lee, S. Sohn, M. Lee, Ionic Equilibria and Ion Exchange of Molybdenum(VI) from Strong Acid Solution, Bulletin Korean Chem. Soc. 32(10) (2011) 3687-3691.

[29] T. Guo, Y. Lei, X. Hu, G. Yang, J. Liang, Q. Huang, X. Li, M.Y. Liu, X.Y. Zhang, Y. Wei, Hydrothermal synthesis of MXene-MoS_2 composites for highly efficient removal of pesticides. Appl. Surf. Sci. 588 (2022) 152597.

[30] J. Serrano Gómez, F. Granados Correa, ^{99m}Tc generator with hydrated MnO_2 as adsorbent of ^{99}Mo, J. Radioanal. Nucl. Chem. 254(3) (2002) 625-628.

[31] Y. Suzuki, T. Kitagawa, Y. Namekawa, M. Matsukura, K. Nishikata, H. Mimura, K. Tsuchiya, Molybdenum Adsorption and Desorption Properties of Alumina with Different Surface Structures for $^{99}Mo/^{99m}Tc$ Generators, Trans. Mater. Res. Soc. Jpn. 43(2) (2018) 75-80.

[32] I. Saptiama, Y.V. Kaneti, Y. Suzuki, K. Tsuchiya, N. Fukumitsu, T. Sakae, J. Kim, Y.M. Kang, K. Ariga, Y. Yamauchi, Template-Free Fabrication of Mesoporous Alumina Nanospheres Using Post-Synthesis Water-Ethanol Treatment of Monodispersed Aluminium Glycerate Nanospheres for Molybdenum Adsorption, Small 14(21) (2018) e1800474.

[33] R. Chakravarty, R. Ram, A. Dash, M.R. Pillai, Preparation of clinical-scale $^{99}Mo/^{99m}Tc$ column generator using neutron activated low specific activity ^{99}Mo and nanocrystalline gamma-Al_2O_3 as column matrix, Nucl. Med. Biol. 39(7) (2012) 916-22.

[34] H.E. Ramadan, M.A. El-Amir, M. Mostafa, Adsorption studies of molybdate(VI)-(99)Mo onto nano zirconium hydroxide gel, Appl. Radiat. Isot. 181 (2022) 110092.

[35] J. Wang, R. Gao, Q. Huang, X. Yin, M. Lin, S. Cao, D. Chen, F. Fan, X. Wu, Z. Qin, Z. Guo, J. Bai, J. Chu, W. Tian, C. Tan, B. Li, N. Cheng, Z. Jia, Practicality of hierarchically macro/mesoporous gamma-Al_2O_3 as a promising sorbent in the preparation of low specific activity $^{99}Mo/^{99m}Tc$ generator, Appl. Radiat. Isot. 178 (2021) 109986.

[36] M. Amin, M.A. El-Amir, H.E. Ramadan, H. El-Said, $^{99}Mo/^{99m}Tc$ generators based on aluminum molybdate gel matrix prepared by nano method, J. Radioanal Nucl. Chem. 318(2) (2018) 915-922.

[37] D. Feng, W.C. Chung, Z. Wei, Z.Y. Gu, H.L. Jiang, Y.P. Chen, D.J. Darensbourg, H.C. Zhou, Construction of ultrastable porphyrin Zr metal-organic frameworks through linker

elimination, J. Am. Chem. Soc. 135(45) (2013) 17105-17110.

[38] D. Feng, Z.Y. Gu, J.R. Li, H.L. Jiang, Z. Wei, H.C. Zhou, Zirconium-metalloporphyrin PCN-222: mesoporous metal-organic frameworks with ultrahigh stability as biomimetic catalysts, Angew Chem. Int. Ed. Engl. 51(41) (2012) 10307-10310.

[39] X. Zhu, B. Li, J. Yang, Y. Li, W. Zhao, J. Shi, J. Gu, Effective adsorption and enhanced removal of organophosphorus pesticides from aqueous solution by Zr-based MOFs of UiO-67, ACS Appl. Mater. Interfaces 7(1) (2015) 223-231.

[40] Y. Zhan, Y. Liu, H. Zu, Y. Guo, S. Wu, H. Yang, Z. Liu, B. Lei, J. Zhuang, X. Zhang, D. Huang, C. Hu, Phase-controlled synthesis of molybdenum oxide nanoparticles for surface enhanced Raman scattering and photothermal therapy, Nanoscale 10(13) (2018) 5997-6004.

[41] W. Zhu, X. Huang, Y. Zhang, Z. Yin, Z. Yang, W. Yang, Renewable molybdate complexes encapsulated in anion exchange resin for selective and durable removal of phosphate, Chin. Chem. Lett. 32, (2021) 3382-3386.

[42] L. Wang, P.X. Jin, S.H. Duan, J.W. Huang, H.D. She, Q.Z. Wang, T.C. An, Accelerated Fenton-like kinetics by visible-light-driven catalysis over iron(iii) porphyrin functionalized zirconium MOF: effective promotion on the degradation of organic contaminants, Environ. Sci. Nano 6(8) (2019) 2652-2661.

[43] H. Jia, D. Ma, S. Zhong, L. Li, L. Li, L. Xu, B. Li, Boosting photocatalytic activity under visible-light by creation of PCN-222/g-C_3N_4 heterojunctions, Chem. Eng. J. 368 (2019) 165-174.

[44] G.Q. Lv, S.W. Chen, H.F. Zhu, M. Li, Y.X. Yang, Pyridinic-nitrogen-dominated nitrogen-doped graphene stabilized Cu for efficient selective oxidation of 5-hydroxymethfurfural, Appl. Surf. Sci. 458 (2018) 24-31.

[45] Q.Q. Zhu, W.W. Zhang, H.W. Zhang, R.R. Yuan, H.M. He, Elaborately manufacturing an electrochemical aptasensor based on gold nanoparticle/COF composites for amplified detection performance, J. Mater. Chem. C 8(47) (2020) 16984-16991.

[46] X. Gong, Y. Shu, Z. Jiang, L. Lu, X. Xu, C. Wang, H. Deng, Metal-Organic Frameworks for the Exploitation of Distance between Active Sites in Efficient Photocatalysis, Angew Chem. Int. Ed. Engl. 59(13) (2020) 5326-5331.

[47] World Health Organization, 2009. Sodium Pertechnetate ([99mTc]) Injection (Non-fission): Revised Final text for addition to The International Pharmacopoeia.

Supporting Information

S1. Adsorption experiments

Adsorption kinetics of PCN-222 and PCN-224 was conducted as follows: 6±0.5 mg adsorbents and 1 ml of Mo solution at pH 3 (5 mg/ml) were added in Eppendorf tubes. After shaking from 5 to 1440 min, all tubes were centrifuged and the Mo concentration of the supernatant solutions was measured using ICP-OES.

To explore the influence of pH on Mo adsorption, experiments were carried out at a pH ranging from 2 to 10. First, 6±0.5 mg of the adsorbents and 1 ml of Mo solution (5 mg/ml) were added in Eppendorf tubes. After shaking for 24 h, all tubes were centrifuged and the molybdenum concentration of the supernatant solutions was measured using ICP-OES.

S2. Adsorption models

The experimental data were fitted using the Freundlich and Langmuir models. The linear mathematical equation of the Freundlich model can be described as

$$lnq_e = \frac{1}{n}lnC_e + lnK_F \qquad (S-1)$$

The linear mathematical equation of the Langmuir model can be described as

$$\frac{C_e}{q_e} = \frac{1}{Q_m}C_e + \frac{1}{Q_mK_L} \qquad (S-2)$$

Where C_e (mg/mL) and q_e (mg/g) are the Mo concentration and the Mo adsorption capacity at equilibrium, respectively. K_F is Freundlich constant and K_L is Langmuir constant. Q_m (mg/g) is the maximum adsorption capacity. The value of n reflects the sorption intensity, which is classified to be irreversible (n=0), favorable (0<1/n<1) and unfavorable (1/n>1).

The experimental dates were analyzed with the pseudo-first-order and the pseudo-second-order model to determine the adsorption kinetic process. The pseudo-first-order model can be described as follow:

$$ln(q_e-q_t)=lnq_e-K_1t \qquad (S-3)$$

The pseudo-second-order model can be described as follow:

$$\frac{t}{q_t} = \frac{1}{K_2q_e^2} - \frac{t}{q_e} \qquad (S-4)$$

Where K_1 is the pseudo-first-order constant and K_2 is the pseudo-second-order constant. q_t (mg/g) and q_e (mg/g) are Mo adsorption capacity at time t and equilibrium.

S3. Fabrication of ^{99}Mo/^{99m}Tc generator

20 mg of enriched MoO_3 (>99.95%) was sealed in a glass vial and irradiated 3 h by neutrons at the reactor Institute of Energy Security and Environmental Safety Centre for Energy Research, Hungary. The 20 mg of irradiated target (~68 MBq) and 355 mg of non-irradiated MoO_3 were dissolved in 20 mL of NaOH solution at room temperature. Then pH of the prepared solution was adjusted to 3 resulting in total volume of molybdenum solution of 25 mL. Therefore, the molybdenum concentration was 10 mg/mL and the specific activity was 272 MBq/g.

A plastic column of 0.5 cm inner diameter (0.5 cm×10 cm) was equipped with two filters (20 µm pores) and ~100 mg of prepared MOFs. 50 mL of HCl solution (pH=3) was used to rinse the columns, which were fed using 5 ml (A_0) of molybdenum solution (5 mg/ml) under flow rate of 0.3 ml/min. The eluted solution was collected and its activity was measured (A_1). 150 ml of saline solution was then passed through the columns to remove loose molybdenum species and the eluted solution was collected for gamma counts measurement (A_2) using Wallac. Finally, the generator was eluted periodically at 24 hours intervals using saline solution with different pH values (6.1, 7.9 and 9.6). The activity of all eluted fractions was analyzed by a germanium detector (Model LG22) and a NaI(T1) counter coupled to a 2048 analyzer (Wallac gamma counter, PerkinElmer). The gamma counts were recorded by measuring the 140 keV (^{99m}Tc) and 740 keV (^{99}Mo) γ-ray photon-peaks.

The dynamic adsorption capacity was calculated by the following equation:

$$q_d = \frac{(A_0 - C_1 - C_2) \times V}{m} \tag{S-5}$$

The zirconium breakthrough was measured by ICP-OES. The ^{99}Mo breakthrough was determined by using the following equation:

[^{99}Mo activity in eluted fraction]/[^{99}Mo activity +^{99m}Tc activity in eluted fraction]

The elution yield was calculated based on the following equation:

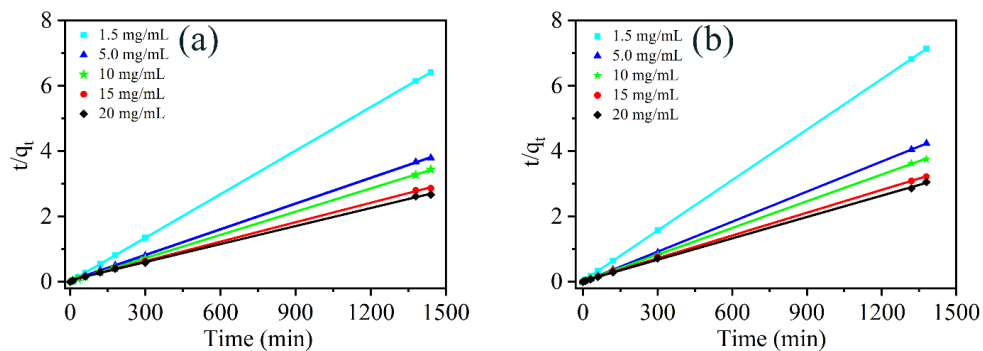[^{99m}Tc activity in the eluted fraction]/ [expected ^{99m}Tc activity]

Figure S3.1. Mo adsorption kinetics of (a) PCN-222 and (b) PCN-224 fitted using the pseudo-second-order model.
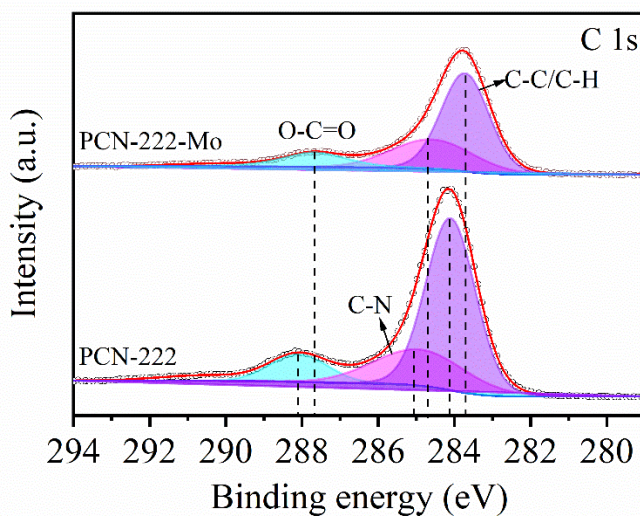

Figure S3.2. C 1s XPS spectra of PCN-222 before and after Mo adsorption.
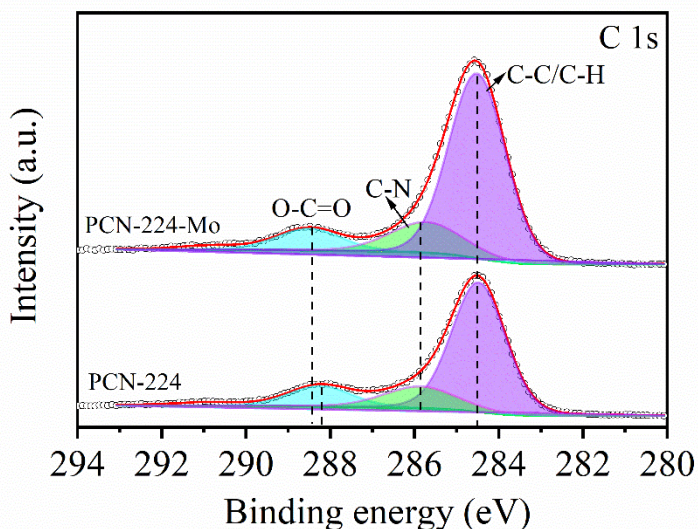
Figure S3.3. C 1s XPS spectra of PCN-224 before and after Mo adsorption.

Table S3.1. Parameters calculated from the pseudo-first-order and pseudo-second-order

model for Mo adsorption on PCN-222

C_0 (mg/mL)	Pseudo-first order			Pseudo-second order		
	q_e, calcd (mg/g)	K_1 (min^{-1})	R^2	q_e, calcd (mg/g)	K_2 (g/mg·min)	R^2
1.62	11.22	0.0035	0.828	224.72	0.0018	1.000
5.57	58.47	0.0024	0.780	380.23	0.0093	0.999
10.91	166.98	0.0207	0.981	421.94	0.0005	0.999
16.20	109.95	0.0019	0.784	505.05	0.0001	0.999
21.46	146.55	0.0020	0.784	543.48	0.00006	0.999

Table S3.2. Parameters calculated from the pseudo-first-order and pseudo-second-order

model for Mo adsorption on PCN-224

C_0 (mg/mL)	Pseudo-first order			Pseudo-second order		
	q_e, calcd (mg/g)	K_1 (min^{-1})	R^2	q_e, calcd (mg/g)	K_2 (g/mg·min)	R^2
1.55	34.08	0.0082	0.807	194.18	0.0001	1.000
5.51	35.21	0.0112	0.660	325.73	0.0019	0.999
10.54	39.35	0.0020	0.592	367.65	0.0006	0.999
15.69	77.45	0.0032	0.998	434.78	0.0002	0.999
20.93	79.43	0.0031	0.750	458.72	0.0002	0.999

Table S3.3. Parameters calculated from the Langmuir and Freundlich model fit for Mo

adsorption

Samples	Langmuir Parameters			Freundlich Parameters		
	Q_m	K_L	R^2	$1/n$	K_F	R^2
PCN-222	503	12.25	0.903	0.18	304	0.961
PCN-224	452	1.99	0.945	0.22	240	0.997

Table S3.4. Surface area of PCN-222 and PCN-224

Samples	BET (m^2/g)	V (cm^3/g)
PCN-222	1882	1.22
PCN-224	1467	0.56
PCN-222-Mo	471	0.31
PCN-224-Mo	13	0.002

Table S3.5. Elution performances of PCN-222 based $^{99}Mo/^{99m}Tc$ generator

Elution No.	Time of growth (h)	Elution yield (%)	^{99}Mo breakthrough
1	24	28.4	5.9
2	25	30.1	7.1
3	22	33.8	6.5
4	24	30.2	5.0

Table S3.6. Elution performances of PCN-224 based $^{99}Mo/^{99m}Tc$ generator

Elution No.	Time of growth (h)	Elution yield (%)	^{99}Mo breakthrough
1	23	7.9	19.7
2	25	9.9	14.4
3	22	5.9	15.1
4	24	6.5	14.2

A cerium-based metal-organic framework as adsorbent for the ^{99}Mo/^{99m}Tc generator

4
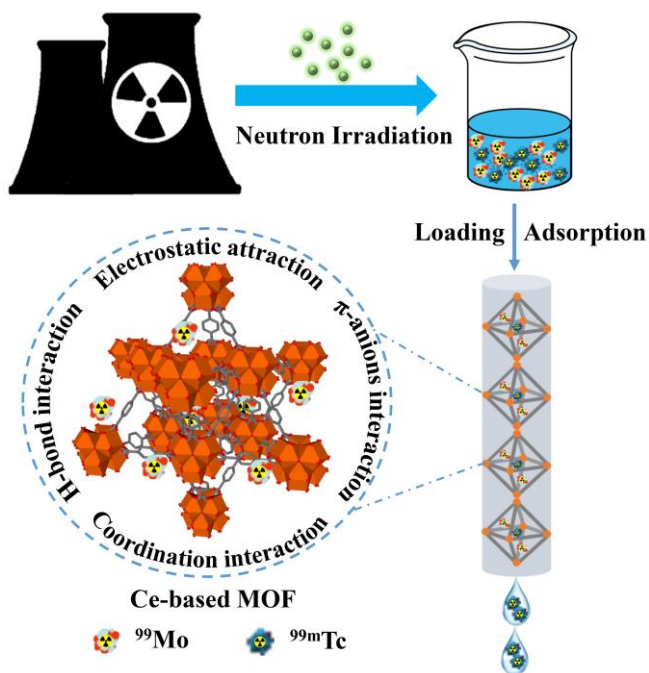
Abstract

The cerium-based metal-organic framework UiO-66 (Ce) was examined as a potential adsorbent for the ^{99}Mo/^{99m}Tc generator. The results showed that the adsorbent had an outstanding adsorption performance, reaching up to 475 mg/g adsorption capacity at pH 3. An adsorption mechanism was proposed, where the adsorption was governed by hydrogen bonds, Ce-O-Mo coordination, π-anions and electrostatic interaction. Additionally, the adsorbent exhibited excellent radiation stability and good adsorption performance when radioactive ^{99}Mo was applied. A ^{99}Mo/^{99m}Tc generator was fabricated with UiO-66 (Ce) as adsorbent and its performance was evaluated over two weeks. The elution results showed that 92±3% of ^{99m}Tc elution efficiency could be obtained with negligible cerium breakthrough, showing the great potential of UiO-66 (Ce) as adsorbent for ^{99}Mo/^{99m}Tc generators.

4.1 Introduction

Technetium-99m, which is typically produced from the $^{99}Mo/^{99m}Tc$ generator, is the most applied diagnostic radionuclide in nuclear medicine [1]. Technetium-99m, which is the decay product of molybdenum-99, can be separated from its parent radionuclide using various methods, for example, column chromatography, solvent extraction, sublimation and electrochemical separation [2]. Chromatographic separation is the most often applied due to its high efficiency, simplicity and speed of operation. When preparing commercial generators, ^{99}Mo is obtained as a ^{235}U fission product with high specific activity, which is essential due to the limited molybdenum adsorption capacity of the alumina adsorbent used (2~20 mg/g) in the commercial generators [3].

Alternative ^{99}Mo production routes involving the irradiation of molybdenum targets by the ^{98}Mo (n, γ) ^{99}Mo and the ^{100}Mo (γ, n) ^{99}Mo reactions have received attention in the last few years [4]. These processes have advantages such as lower cost, no nuclear waste and availability of many production places worldwide, i.e., nuclear research reactors and accelerators [5]. However, these routes produce low specific activity ^{99}Mo that restricts its application using conventional alumina-based chromatography columns. To overcome this drawback, many adsorbents have been prepared and their performance in $^{99}Mo/^{99m}Tc$ generators has been explored. For example, Saptiama et al. synthesized mesoporous alumina under high calcination temperature, achieving maximum molybdenum adsorption of 41.6 mg/g [6]. The ^{99}Mo adsorption capacity of polymer zirconium composites synthesized by Tanase et al. could reach about 200 mg/g with ^{99m}Tc elution yield of 80% [7]. Chakravarty et al. developed some nanomaterials with an acceptable adsorption capacity from 70 to 250 mg/g, such as nano titania, nanocrystalline alumina and nano zirconia [8, 9]. These materials, however, have limited molybdenum adsorption capacity due to their low surface area. Therefore, new adsorbents having higher adsorption capacity and fast uptake are still required. Over the past few years, metal-organic frameworks (MOFs) have been extensively researched for diverse applications, due to their high surface area, easy functionalization and tuneable pore size [10, 11]. One of the most studied MOFs is UiO-66 (University of Oslo), thanks to its outstanding thermal, chemical and mechanical stability [12, 13]. Our previous work proved that UiO-66 (Zr) shows good performance and can be applied as an adsorbent for $^{99}Mo/^{99m}Tc$ generator [14]. Meanwhile, it was reported that cerium was a promising metal

to use for MOF fabrication due to its inherent conversion trend between Ce^{4+} and Ce^{3+}, which could result in different adsorption sites [15]. The first cerium-based MOF with the UiO-66 structure was reported by Lammert et.nl. in 2015 [16] and was applied in various fields, including gas separation, catalysis and sensor [17-19].

In this study, the potential of UiO-66 (Ce) as a molybdenum adsorbent for $^{99}Mo/^{99m}Tc$ generator was explored. The molybdenum adsorption performance of UiO-66 (Ce), including adsorption kinetics and isotherms, was investigated by varying the molybdenum concentration and the pH value. The interaction between adsorbent and molybdenum species was also analysed by a combination of different characterization techniques, including zeta potential, Raman spectroscopy and X-ray photoelectron spectroscopy. The radiation stability of UiO-66 (Ce) was also investigated under gamma radiation. Furthermore, a $^{99}Mo/^{99m}Tc$ generator was fabricated with UiO-66 (Ce) and its performance was investigated including elution yield, ^{99}Mo breakthrough and cerium breakthrough.

4.2 Experimental section

4.2.1 Materials

1,4-benzenedicarboxylate (BDC, 98%), ammonium cerium(IV) nitrate $((NH_4)_2Ce(NO_3)_6, >95.5\%)$ and N,N-dimethylformamide (DMF, 99.8%) were purchased from Sigma Aldrich. Molybdenum oxide (≥99.95%) was purchased from Alfa Aesar. All chemical reagents were used without any purification.

4.2.2 Synthesis of Ce-based MOF

UiO-66 (Ce) was synthesized based on previously reported literature [16]. First, 1,4-benzenedicarboxylate (85.2 mmol) was dissolved into a glass bottle containing DMF (4.8 mL). Then, the aqueous solution of cerium ammonium nitrate (0.5333 M, 0.8 mL) was added to the mixture and the glass bottle was heated at 100 °C for 20 min using magnetic stirring. Afterwards, the precipitate was washed two times with DMF and ethanol, respectively. The obtained powder was dried at 70 °C for 12 h.

4.2.3 Characterization

The X-ray diffraction patterns of prepared MOF were recorded by a PANalytical X'pert Pro PW3040/60 diffractometer with Cu Kα radiation with an angular 2θ ranging from 5~40°. The surface area of the samples was determined by nitrogen adsorption at liquid nitrogen temperature by a Micromeritics Tristar II and calculated using the Brunauer-Emmett-Teller (BET) method. Inductively coupled plasma optical emission spectrometry (ICP-OES, Optima 4300 DV, Perkin Elmer) was applied to determine the molybdenum concentration before and after adsorption. The Zeta potential of the samples was performed within a pH range of 2~12 using a Malvern Zetasizer Nano S at room temperature. X-ray photoelectron spectra (XPS) were obtained on Thermofisher Scientific electron spectroscopy with Mg K-alpha source. The optical absorption property of sample was collected by a UV adsorption spectrophotometer (UV-6300PCC, VWR). The morphology and elements distribution of the adsorbent were studied using scanning electron microscopy (SEM, JEOL ISM-IT100) and energy dispersive spectroscopy (EDS, JEOL ISM-IT100). Raman spectroscopy of the sample was performed by a Raman spectrometer (LabRAM HR, HORIBA Scientific) with a green laser (λ=532 nm) at room temperature. The prepared sample was irradiated by a Co-60 source with different doses (100 kGy, 350 kGy and 550 kGy) at a dose rate of 0.53 kGy/h.

4.2.4 Molybdenum adsorption

The effect of pH on the molybdenum adsorption uptake of UiO-66 (Ce) was studied for a pH range of 2~12. Typically, 6 mg of the adsorbent was added to Eppendorf tubes with different molybdenum concentrations (0.1~20 mg/mL). All tubes were shaken for 20 h at room temperature by a temperature-controlled vibrator. Then, the adsorbents were separated using a centrifuge and the supernatant solution was diluted at appropriate times for concentration measurement using ICP-OES. The uptake (*q*) was defined by the following equation:

$$q=(C_b-C_a)*V/m$$

Where C_b and C_a (mg/mL) are the molybdenum concentration before and after adsorption, respectively. *V* (mL) and *m* (mg) represent the volume of molybdenum solution and mass of adsorbent, respectively. All adsorption experiments were performed in triplicate. The details about column preparation of the $^{99}Mo/^{99m}Tc$ generator and the separation of radionuclides were described in Supporting Information S-1.

4.3 Results and discussion

4.3.1 Characterization

The morphology and elemental distribution of UiO-66 (Ce) were determined by SEM and EDS. As shown in Fig. 4.1, it can be observed that the prepared sample had spherical particles with a diameter between 200 and 400 nm. The EDS mapping showed the presence of uniformly distributed C, O, Ce. Fig. 4.2 (a) shows the XRD patterns of UiO-66 (Ce) before and after molybdenum adsorption. The pattern of UiO-66 (Ce) prior to molybdenum adsorption displayed all diffraction peaks consistent with the simulated XRD pattern (also shown in Fig. 4.2 (a)) and no impurities were observed. Fig. 4.2 (b) displays the N_2 adsorption-desorption isotherms of UiO-66 (Ce) at 77 K. The adsorption isotherms belong to the type I adsorption curve. The calculated BET surface area and micropore volumes were 1140 m^2/g and 0.4 cm^3/g, respectively. The XRD and N_2 adsorption results of UiO-66 (Ce) after molybdenum adsorption in Fig. 4.2 will be discussed later.
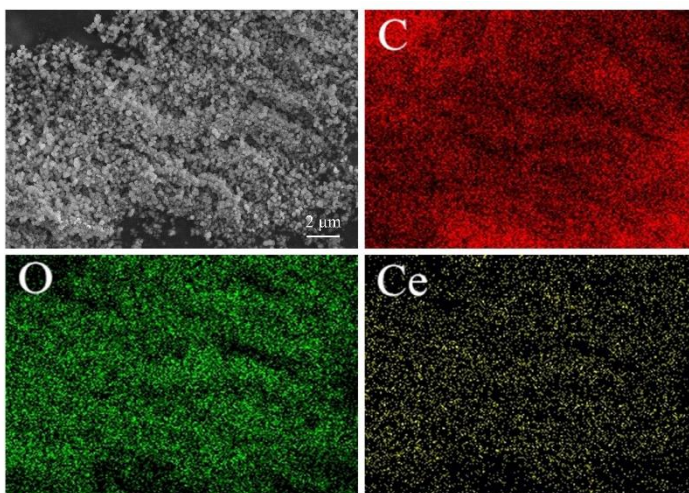

Fig. 4.1. SEM images and EDS mapping of UiO-66 (Ce) before molybdenum adsorption (b) C, (c) O and (d) Ce.
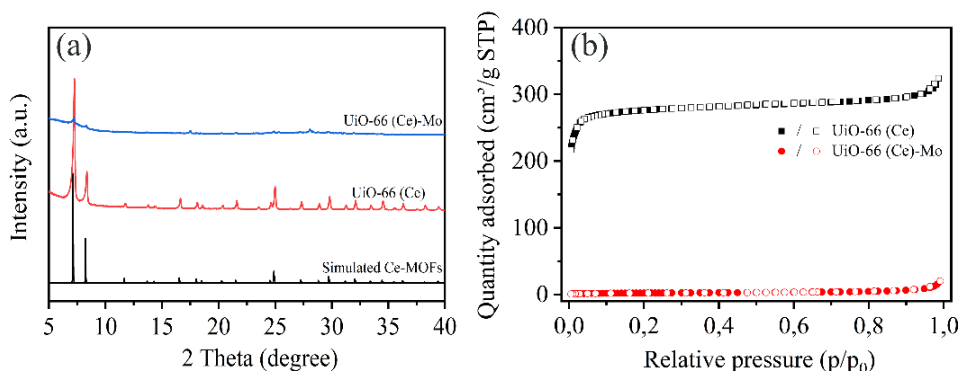
Fig. 4.2. (a) XRD patterns and (b) N_2 adsorption-desorption isotherms of UiO-66 (Ce) before and after molybdenum adsorption at pH 3 in equilibrium concentration.

4.3.2 Molybdenum adsorption studies

Effect of pH

The pH of the solution influences the formation of molybdenum species and therefore its effect on the molybdenum adsorption was investigated [20]. Fig. 4.3 (a) shows the zeta potential of UiO-66 (Ce) and its isoelectric point (IEP) was somewhere between 8 and 11.5, meaning that the adsorbent was positively charged when the pH was lower than the pH value of the IEP. The $Mo_7O_{24}^{6-}$ complexes are the dominant molybdenum chemical species at a pH range of 2~5 and the major species is MoO_4^{2-} at pH>5 (Figure S4.3), when molybdenum concentration is 5 mg/mL [21]. The negatively charged molybdenum species in an acidic and neutral environment are beneficial for the adsorption on the positively charged UiO-66 (Ce). Fig. 4.3 (b) shows the effect of pH on the adsorption capacity of UiO-66 (Ce). The molybdenum uptake of UiO-66 (Ce) decreased gradually from 400 to 250 mg/g with increasing pH from 2 to 5, reaching eventually 220 mg/g at pH 8. This trend is consistent with the zeta potential of UiO-66 (Ce), suggesting that electrostatic attraction plays a key role in molybdenum adsorption. However, the adsorption capacity of UiO-66 (Ce) is still 182 mg/g when the zeta potential of the adsorbent was negative, indicating that electrostatic attraction was not the only interaction mechanism involved in the molybdenum adsorption.
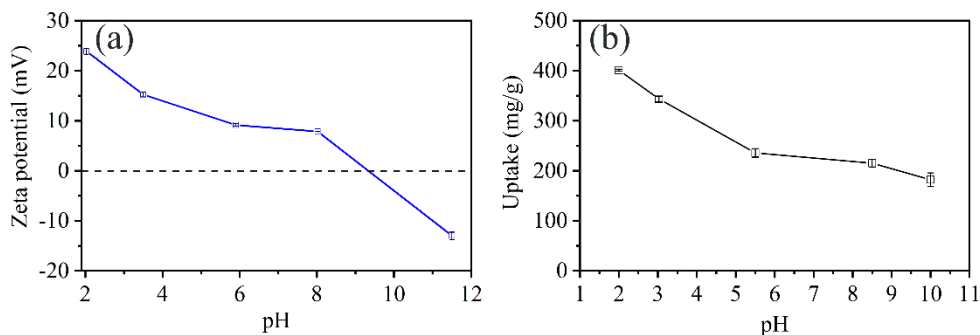
Fig. 4.3. Effect of pH on (a) zeta potential and (b) uptake of UiO-66 (Ce), the initial Mo concentration of 5 mg/mL.

Adsorption kinetics

Batch experiments were carried out to investigate the molybdenum adsorption isotherms and adsorption kinetics of UiO-66 (Ce). The molybdenum adsorption uptake was investigated at pH 3 for different incubation times, as shown in Fig. 4.4 (a). UiO-66 (Ce) showed an initial rapid molybdenum adsorption uptake, reaching 80% of the equilibrium value after 30 min for all studied concentrations. This fast adsorption kinetics could be due to the existence of many available sites on the external surface, which prompts molybdenum ions to diffuse into the adsorption sites [22]. The uptake was more than 90% of the equilibrium value after 1.5 h and reached saturation after 3 h, due to the diffusion of molybdenum species into the inner pores of UiO-66 (Ce). Moreover, the equilibrium uptake of UiO-66 (Ce) increased when increasing the concentration and then remained stable when the initial molybdenum concentration was 10 mg/mL, suggesting that the molybdenum adsorption is closed to reach saturation. To further characterize the adsorption kinetics, the pseudo-first-order and pseudo-second-order kinetic models were applied to fit the adsorption kinetics. The fitting results of these models are displayed in Figure S4.4 and Table S4.1. These results indicated that the adsorption process was better described by the pseudo-second-order model, which according to the model indicated that the adsorption rate was dominated by chemical interaction [23]. In addition, the intraparticle diffusion model was employed to better understand the adsorption process. As shown in Figure S4.5 and Table S4.2, it can be observed that the first stage has a fast adsorption rate on the surface or adsorption sites of UiO-66 (Ce). In contrast, molybdenum species diffuse into inner pores showing a slower adsorption rate.

Adsorption isotherms

Fig. 4.4 (b) shows the Mo adsorption isotherm on UiO-66 (Ce) obtained by the varying initial molybdenum concentration from 0.1 to 20 mg/mL at pH 3. The adsorption uptake of the adsorbent increased abruptly at low concentrations, reaching a capacity of approximately ~350 mg/g at 5 mg/mL, which was more than 80% of the maximum adsorption capacity. Eventually, a plateau of around 475 mg/g, which is consistent with the results of the adsorption kinetics, was achieved. To further understand the molybdenum adsorption process, the Langmuir model and Freundlich models were employed to fit the experimental data. The non-linear fit results and calculated parameters are displayed in Table S4.3. The Langmuir model (R^2=0.997) can fit the experimental data better than the Freundlich model. The maximum adsorption capacity calculated by the Langmuir model was 485 mg/g, which is much higher when compared to that of UiO-66 (Zr) in our previous work [14]. Although the UiO-66 (Ce) has the same crystal structure as UiO-66 (Zr) and has a relatively lower surface area, the Ce-based MOF displayed a much higher molybdenum adsorption capacity, which is probably related to the inherent characteristics of cerium and will be discussed in the adsorption mechanism part of this paper. Moreover, this material exhibited the highest molybdenum adsorption capacity reported so far (Table S4.4).
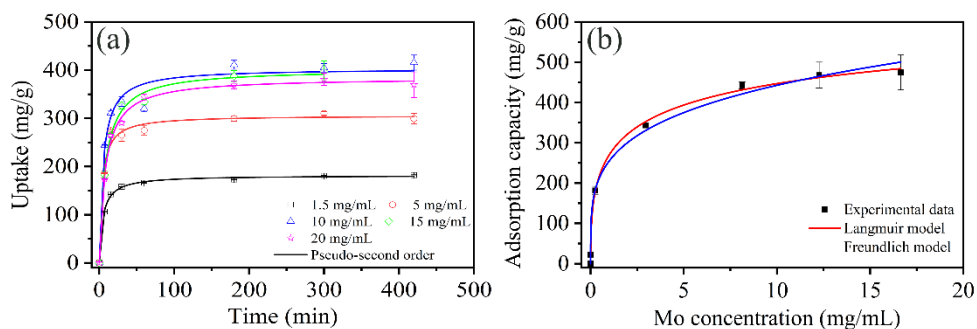

Fig. 4.4. Adsorption (a) kinetics fitted by the pseudo-second-order model and (b) isotherms of UiO-66 (Ce) non-linearly fitted by the Langmuir and Freundlich models at pH 3.

4.3.3   Adsorption mechanism

XRD was utilized to analyse the structure of the UiO-66 (Ce) after adsorption (Fig. 4.2 (a)). The XRD analysis showed that all diffraction peaks still matched well with the sample before adsorption, which indicated that Ce-MOF-Mo kept its crystalline structure upon

molybdenum adsorption. However, all diffraction peaks decreased in intensity after molybdenum adsorption, which was attributed to the trapped molybdenum species, causing the diminished X-ray contrast [24, 25]. The N_2 adsorption-desorption experiment of the Ce-MOF-Mo was also carried out after adsorption (Fig. 4.2 (b)). The BET surface area and pore volumes were 8 m^2/g and 0.0009 cm^3/g, respectively. This dramatic decline in pore volume and surface area indicated that the molybdenum species completely filled the pores of the adsorbent. Furthermore, the EDS mapping (Figure S4.6) showed that the adsorbed molybdenum was distributed uniformly. (Table S4.5).

The Raman spectra of UiO-66 (Ce) before and after molybdenum adsorption at equilibrium concentration is presented in Fig. 4.5. The main peak at 453 cm^{-1} is assigned to the symmetric stretching vibration of Ce-O bonds in metal clusters [26]. After molybdenum adsorption, the peak of UiO-66(Ce)-Mo at 440 cm^{-1} showed a blue-shift, which could be caused by the introduced molybdenum species or defects sites formed in the sample [27, 28]. The broad and weak peaks at 313 cm^{-1} and 813 cm^{-1} were assigned to Mo=O bending vibrations and Mo-O-Mo antisymmetric stretches, respectively. A peak observed at 890 cm^{-1} was attributed to the Ce-O-Mo stretching vibration mode [29], which indicated that molybdenum species were anchored on the adsorbent by Ce-O-Mo coordination [30, 31].
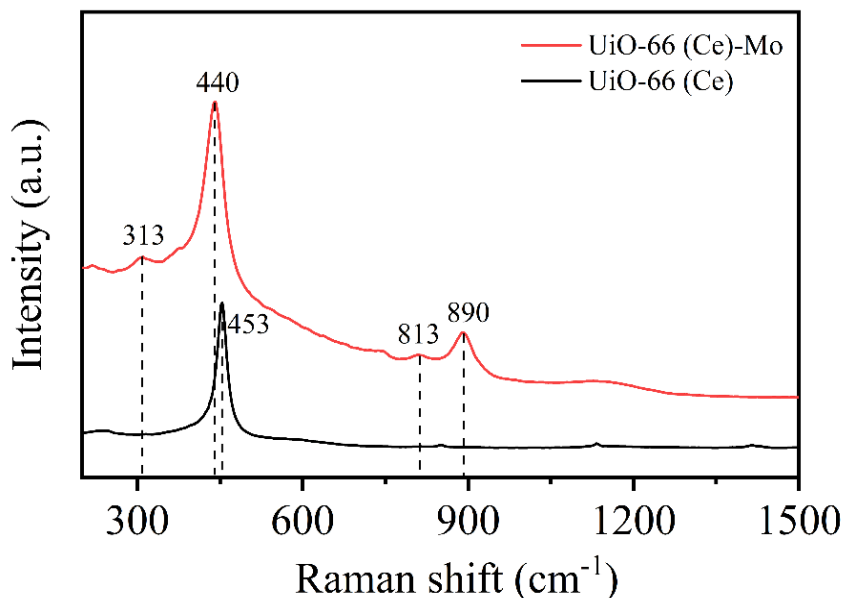

Fig. 4.5. Raman spectroscopy of UiO-66 (Ce) before and after molybdenum adsorption.

To further explore the adsorption mechanism, XPS spectra of UiO-66 (Ce) before and after adsorption were performed. The XPS spectra survey showed the existence of C, O and Ce elements in UiO-66 (Ce) before and after adsorption (Fig. 4.6 (a)). The new binding energy peaks for Ce-MOF-Mo at 228~240 eV and 410~420 eV were attributed to Mo 3d and Mo 3p spectra, respectively [32]. The lower binding energy peaks could be deconvoluted into two doublets at 232.0 eV and 235.1 eV (Fig. 4.6 (b)), which are assigned to Mo $3d_{5/2}$ and Mo $3d_{3/2}$, respectively, indicating the presence of Mo^{6+} [33]. The XPS Ce 3d spectrum of UiO-66 (Ce) before and after adsorption is shown in Fig. 4.6 (c). The whole spectrum could be deconvoluted into 8 peaks corresponding to two different valence states (Table S4.6). This is related to the electron configuration of Ce ([Xe]4f^{1}5d^{1}6s^2) and the low-lying nature of the empty 4f band, causing the formation of Ce^{4+} and partial reduction to Ce^{3+} [34, 35]. The presence of Ce^{3+} cations could cause structural defects such as linker vacancies. These defects would induce the formation of Ce-OH groups [36-38], which are favourable for molybdenum adsorption. In addition, the shift of binding energy to a lower value indicates that the electron density of the Ce atoms increased after adsorption, which was probably due to the formation of Mo-O-Ce coordination bonds [39], matching with the observations of the Raman analysis. Fig. 4.6 (d) shows the C 1s spectra of UiO-66 (Ce) before and after molybdenum adsorption. The C 1s spectra could be deconvoluted into four peaks, which were assigned to π-π*, O=C-O, C-O and C-C/C-H (Table S4.7) [40]. After adsorption, the negative shift by 0.23 eV suggests a strong chemical interaction between C-C/C-H and molybdenum species via hydrogen bonds. The satellite peak at 290.1 eV was determined to be the π-π* component and its percentage decreased from 6.16% to 2.15% after molybdenum adsorption, suggesting the π-anions interaction between adsorbent and molybdenum species. Fig. S4.7 shows the UV absorbance spectra of UiO-66 (Ce). A peak was detected at 240 nm, which was ascribed to the π-π* transitions [40, 41]. However, this peak disappeared after molybdenum adsorption, indicating that the π-π* component reacted with the molybdenum species, which is consistent with the C 1s XPS results. Based on the above analysis, the interaction between the adsorbent and Mo species is governed by electrostatic attraction, hydrogen bonds formation, Mo-O-Ce coordination and π-anions.
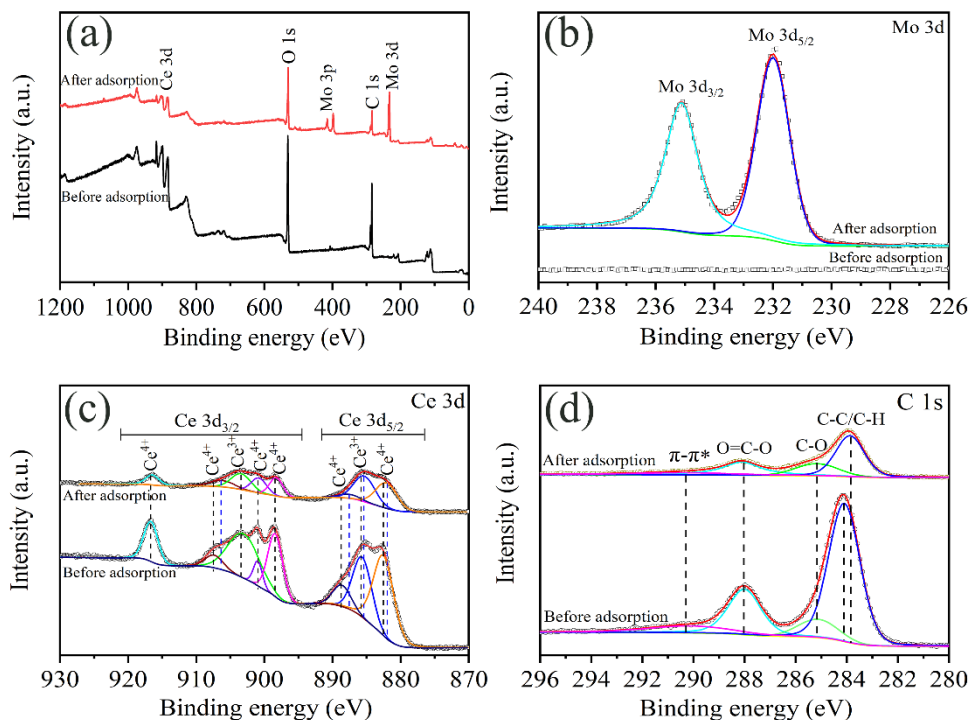
Fig. 4.6. (a) XPS survey spectrum, high-resolution XPS spectra of (b) Mo 3d, (c) Ce 3d and (4) C 1s.

4.3.4 Radiation stability of UiO-66 (Ce)

To further evaluate the adsorption performance of UiO-66 (Ce) as adsorbent for the ^{99}Mo/^{99m}Tc generator, adsorption experiments involving ^{99}Mo were carried out. The results showed that the adsorption capacities of the adsorbent were 11 mg/g, 184 mg/g and 304 mg/g, respectively, when the initial Mo concentrations were 0.1 mg/mL, 1.5 mg/mL and 5 mg/mL. This adsorption uptake was consistent with the adsorption capacity using the non-radioactive Mo solution. Moreover, the crystal structure of the adsorbent after adsorption was characterized by XRD (Fig. 4.7 (a)) and they all showed the same diffraction peaks as the original material, suggesting that the crystal structure of the adsorbent was not affected after ^{99}Mo adsorption. In addition, the radiation stability of UiO-66 (Ce) is an essential characteristic for its use in the ^{99}Mo/^{99m}Tc generator. Fig. 4.7 (b) shows the XRD patterns of UiO-66 (Ce) after exposure to different doses of gamma-ray originating from a Co-60 source. It can be confirmed that this adsorbent kept its good crystallinity after 550 kGy gamma

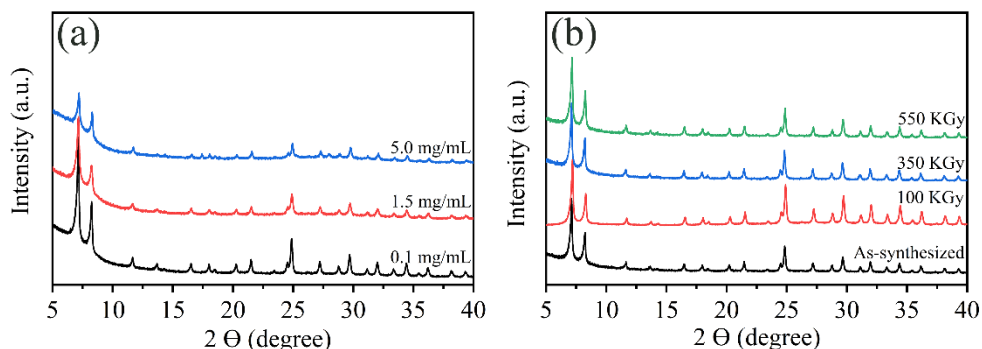irradiation, exhibiting an outstanding radiation resistance.

Fig. 4.7. XRD patterns of UiO-66 (Ce) (a) after ^{99}Mo adsorption at pH 3 for 20 h and (b) after exposure to gamma-ray irradiation.

4.3.5 Performance of UiO-66 (Ce) as adsorbent in $^{99}Mo/^{99m}Tc$ generator

A $^{99}Mo/^{99m}Tc$ generator was packed using UiO-66 (Ce) particles as column bed. After loading ^{99}Mo, the adsorption capacity of the UiO-66 (Ce) generator was determined to be 297 mg/mL, which was consistent with the previous results when non-radioactive molybdenum was applied. Then the column was rinsed with 0.9% saline solution to remove the loosely absorbed molybdenum ions. The practical adsorption capacity of UiO-66 (Ce) was calculated to be 246 mg/g, which was close to the uptake value in the pH range of 5 to 8 (as shown in Fig. 4.3 (b)). Afterwards, the column was eluted daily using 0.9% saline solution (pH=6) for two consecutive weeks. The elution yield and cumulative yield curve of ^{99m}Tc as a function of the volume of the eluted saline solution are shown in Fig. 4.8. It was observed that the elution yield of ^{99m}Tc decreased sharply with the increasing volume of the saline solution. More than 99% of ^{99m}Tc could be collected after passing 6 mL of saline solution through the generator. In Table 4.1, the elution efficiency and the ^{99}Mo and Ce breakthrough of the $^{99}Mo/^{99m}Tc$ generator are displayed. It can be seen that the elution yield of ^{99m}Tc was about 92±3% and remained around that value for two weeks. There is about 0.2%~0.3% of ^{99}Mo contamination in each elution fraction, which is slightly higher than the requirement (<0.1%) defined by the International Pharmacopoeia [42]. The Ce breakthrough in all elution fractions was determined to be around 1 ppm.
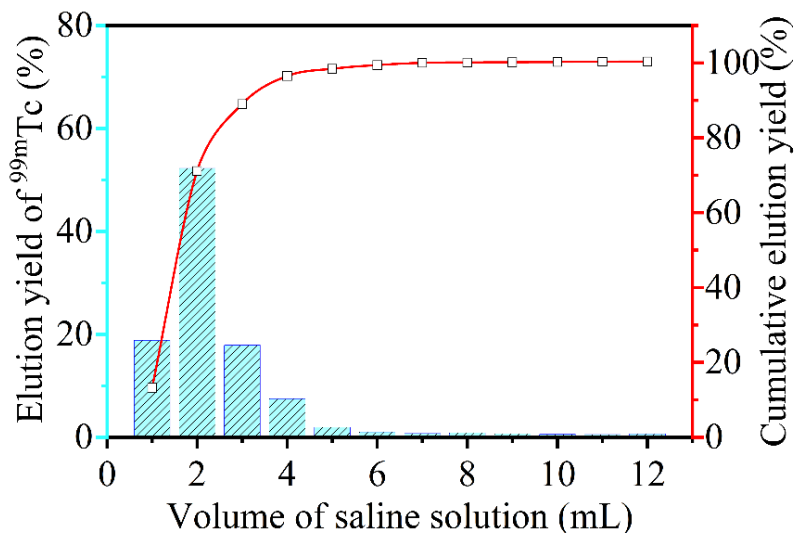
Fig. 4.8. Elution yield of ^{99m}Tc of the ^{99}Mo/^{99m}Tc generator using saline solution (pH=6).

Table 4.1. Elution performance of UiO-66 (Ce) in the ^{99}Mo/^{99m}Tc generator over two weeks

Elution No.	Time of ingrowth (h)	Elution efficiency (%)	^{99}Mo breakthrough (%)	Ce breakthrough (ppm)
1	24	88.8	0.36	1.21
2	72	87.7	0.21	0.92
3	24	91.2	0.28	0.46
4	24	91.0	0.24	0.99
5	24	93.6	0.30	0.98
6	24	90.2	0.33	0.96
7	68	88.6	0.20	0.27
8	24	91.7	0.29	0.96
9	23	93.5	0.19	0.92
10	24	96.9	0.24	0.53
11	24	95.9	0.29	0.93
12	72	96.6	0.09	0.81

The total activity of many commercial generators is about 2 Ci when 2 g of adsorbent is typically used. Alternative production methods to ^{235}U fission can provide ^{99}Mo with specific activity in the range of 1-10 Ci/g [43]. Assuming a generator fabricated with 2 g of UiO-66 (Ce) and 6 Ci/g of specific activity of ^{99}Mo, this adsorbent should be able to deliver 3 Ci of ^{99}Mo, when ~52% of the maximum adsorption capacity (250 mg/g) was applied here. In addition, the column experiment was repeated and the results are shown in Table S4.8. About

92% of ^{99m}Tc elution yield can be achieved, which corresponds with previous results, showing good repeatability. The above results indicated that UiO-66 (Ce) exhibited great potential as adsorbent for ^{99}Mo/^{99m}Tc generator utilizing low specific activity ^{99}Mo, providing new exciting opportunities for production using more production facilities worldwide.

4.4 Conclusions

UiO-66 (Ce) was synthesized successfully and utilized as adsorbent for ^{99}Mo/^{99m}Tc generator. The maximum adsorption capacity of the adsorbent was 475 mg/g and the adsorption reached equilibrium within 3 h. The positive charge of the adsorbent was favourable for molybdenum adsorption by electrostatic attraction. The XPS results confirmed the existence of Ce^{3+}/Ce^{4+} i.e. two chemical valences, causing linker defects and the formation of extra hydroxyl groups, which were beneficial for molybdenum adsorption via coordination interaction, π-anions and hydrogen bonds. Moreover, the adsorption performance of UiO-66 (Ce) using radioactive ^{99}Mo solution verified its good adsorption behaviour and radiation stability. The column results showed that about 92±3% elution efficiency of ^{99m}Tc and low cerium breakthrough could be achieved for two-week elution. The excellent performance of the developed ^{99}Mo/^{99m}Tc generator reveals that UiO-66 (Ce) is a great adsorbent candidate for applications using low specific activity ^{99}Mo.

References

[1] M.R. Pillai, A. Dash, F.F. Knapp, Sustained availability of ^{99m}Tc: possible paths forward, J. Nucl. Med., 54 (2013) 313-323.

[2] A. Dash, R. Chakravarty, Pivotal role of separation chemistry in the development of radionuclide generators to meet clinical demands, RSC Adv., 4(81) (2014) 42779-42803.

[3] R. Chakravarty, R. Ram, R. Mishra, D. Sen, S. Mazumder, M.R.A. Pillai, A. Dash, Mesoporous Alumina (MA) Based Double Column Approach for Development of a Clinical Scale ^{99}Mo/^{99m}Tc Generator Using (n,γ)^{99}Mo: An Enticing Application of Nanomaterial, Ind. Eng. Chem. Res., 52(33) (2013) 11673-11684.

[4] H. Naik, S.V. Suryanarayana, K.C. Jagadeesan, S.V. Thakare, P.V. Joshi, V.T. Nimje, K.C. Mittal, A. Goswami, V. Venugopal, S. Kailas, An alternative route for the preparation of the medical isotope ^{99}Mo from the ^{238}U(γ, f) and ^{100}Mo(γ, n) reactions, J. Radioanal. Nucl. Chem., 295(1) (2012) 807-816.

[5] J. Wang, R. Gao, Q. Huang, X. Yin, M. Lin, S. Cao, D. Chen, F. Fan, X. Wu, Z. Qin, Z. Guo, J. Bai, J. Chu, W. Tian, C. Tan, B. Li, N. Cheng, Z. Jia, Practicality of hierarchically macro/mesoporous γ-Al$_2$O$_3$ as a promising sorbent in the preparation of low specific activity ^{99}Mo/^{99m}Tc generator, Appl. Radiat. Isot., 178 (2021) 109986.

[6] I. Saptiama, Y.V. Kaneti, Y. Suzuki, Y. Suzuki, K. Tsuchiya, T. Sakae, K. Takai, N. Fukumitsu, Z.A. Alothman, M.S.A. Hossain, K. Ariga, Y. Yamauchi, Mesoporous Alumina as an Effective Adsorbent for Molybdenum (Mo) toward Instant Production of Radioisotope for Medical Use, Bull. Chem. Soc. Jpn., 90(10) (2017) 1174-1179.

[7] M. Tanase, K. Tatenuma, K. Ishikawa, K. Kurosawa, M. Nishino, Y. Hasegawa, A ^{99m}Tc generator using a new inorganic polymer adsorbent for (n, γ) ^{99}Mo, Appl. Radiat. Isot., 48(5) (1997) 607-611.

[8] S. Hasan, M.A. Prelas, Molybdenum-99 production pathways and the sorbents for ^{99}Mo/^{99m}Tc generator systems using (n, γ) ^{99}Mo: a review, SN Appl. Sci., 2(11) (2020) 1-28.

[9] A. Dash, R. Chakravarty, Nanomaterial-Based Adsorbent: Promises, Opportunities, and Challenges to Develop Column Chromatography Radionuclide Generators for Nuclear Medicine, Sep. Purif. Rev., 46(2) (2016) 91-107.

[10] J. Canivet, A. Fateeva, Y. Guo, B. Coasne, D. Farrusseng, Water adsorption in MOFs: fundamentals and applications, Chem. Soc. Rev., 43(16) (2014) 5594-5617.

[11] N. Stock, S. Biswas, Synthesis of metal-organic frameworks (MOFs): routes to various MOF topologies, morphologies, and composites, Chem. Rev., 112(2) (2012) 933-969.

[12] M. Kandiah, M.H. Nilsen, S. Usseglio, S. Jakobsen, U. Olsbye, M. Tilset, C. Larabi, E.A. Quadrelli, F. Bonino, K.P. Lillerud, Synthesis and Stability of Tagged UiO-66 Zr-MOFs, Chem. Mater., 22(24) (2010) 6632-6640.

[13] F. Ahmadijokani, R. Mohammadkhani, S. Ahmadipouya, A. Shokrgozar, M. Rezakazemi, H. Molavi, T.M. Aminabhavi, M. Arjmand, Superior chemical stability of UiO-66 metal-organic frameworks (MOFs) for selective dye adsorption, Chem. Eng. J., 399 (2020) 125346.

[14] C. Ma, A. Vasileiadis, H.T. Wolterbeek, A.G. Denkova, P. Serra Crespo, Adsorption of molybdenum on Zr-based MOFs for potential application in the ^{99}Mo/^{99m}Tc generator, Appl. Surf. Sci., 572 (2022) 151340.

[15] J. He, Y. Xu, Z. Xiong, B. Lai, Y. Sun, Y. Yang, L. Yang, The enhanced removal of phosphate by structural defects and competitive fluoride adsorption on cerium-based adsorbent, Chemosphere, 256 (2020) 127056.

[16] M. Lammert, M.T. Wharmby, S. Smolders, B. Bueken, A. Lieb, K.A. Lomachenko, D.D. Vos, N. Stock, Cerium-based metal organic frameworks with UiO-66 architecture: synthesis, properties and redox catalytic activity, Chem. Commun., 51(63) (2015) 12578-12581.

[17] Z. Hu, Y. Wang, D. Zhao, The chemistry and applications of hafnium and cerium(iv) metal-organic frameworks, Chem. Soc. Rev., 50(7) (2021) 4629-4683.

[18] J. Yang, K. Li, C. Li, J. Gu, Intrinsic Apyrase-Like Activity of Cerium-Based Metal-Organic Frameworks (MOFs): Dephosphorylation of Adenosine Tri- and Diphosphate, Angew. Chem. Int. Ed., 59(51) (2020) 22952-22956.

[19] Y. Zhang, X. Zeng, X. Jiang, H. Chen, Z. Long, Ce-based UiO-66 metal-organic frameworks as a new redox catalyst for atomic spectrometric determination of Se(VI) and colorimetric sensing of Hg(II), Microchem. J., 149 (2019) 103967.

[20] L. Cifuentes, C. Ramírez, G. Crisóstomo, J.M. Casas, Separation of Molybdenum Species by Electrodialysis, Chem. Eng. Commun., 198(6) (2011) 805-814.

[21] L., Man-Seung, S., Seong-Ho, L., Myung-Ho, Ionic Equilibria and Ion Exchange of Molybdenum (VI) from Strong Acid Solution. Bulletin Korean Chem. Soc., 32 (2011) 3687-3691.

[22] J. Wu, J. Zhou, S. Zhang, A. Alsaedi, T. Hayat, J. Li, Y. Song, Efficient removal of metal contaminants by EDTA modified MOF from aqueous solutions, J. Colloid. Interface Sci., 555 (2019) 403-412.

[23] W. Tan, T. Chen, W.R. Liu, F.G. Ye, S.L. Zhao, Design and fabrication of boric acid functionalized hierarchical porous metal-organic frameworks for specific removal of cis-diol-containing compounds from aqueous solution, Appl. Surf. Sci., 535 (2021) 147714.

[24] J.L. Gu, J.L. Shi, G.J. You, L.M. Xiong, S.X. Qian, Z.L. Hua, H.R. Chen, Incorporation of highly dispersed gold nanoparticles into the pore channels of mesoporous silica thin films and their ultrafast nonlinear optical response, Adv. Mater., 17(5) (2005) 557-560.

[25] X. Zhu, B. Li, J. Yang, Y. Li, W. Zhao, J. Shi, J. Gu, Effective adsorption and enhanced

removal of organophosphorus pesticides from aqueous solution by Zr-based MOFs of UiO-67, ACS Appl. Mater. Interfaces, 7(1) (2015) 223-231.

[26] E. Villa-Aleman, A.L. Houk, D.D. Dick, S.E.H. Murph, Hyper-Raman spectroscopy of CeO_2, J. Raman Spectrosc., 51(7) (2020) 1260-1263.

[27] L. Wang, J. Zhang, G. Wang, W. Zhang, C. Wang, C. Bian, F.S. Xiao, Selective hydrogenolysis of carbon-oxygen bonds with formic acid over a Au-Pt alloy catalyst, Chem. Commun., 53(18) (2017) 2681-2684.

[28] F. Wang, S. He, H. Chen, B. Wang, L. Zheng, M. Wei, D.G. Evans, X. Duan, Active Site Dependent Reaction Mechanism over Ru/CeO_2 Catalyst toward CO_2 Methanation, J. Am. Chem. Soc., 138(19) (2016) 6298-6305.

[29] W.X. Kuang, Y.N. Fan, K.D. Chen, Y. Chen, Partial oxidation of toluene over ultrafine mixed Mo-based oxide particles, J. Catal. 186(2) (1999) 310-317.

[30] F. Chandoul, A. Boukhachem, F. Hosni, H. Moussa, M.S. Fayache, M. Amlouk, R. Schneider, change of the properties of nanostructured MoO_3 thin films using gamma-ray irradiation, Ceram. Int., 44(11) (2018) 12483-12490.

[31] H. Jeziorowski, H. Knozinger, Raman and Ultraviolet Spectroscopic Characterization of Molybdena on Alumina Catalysts, J. Phys. Chem., 83(9) (1979) 1166-1173.

[32] G.D. Khattak, M.A. Salim, A.S. AlHarthi, D.J. Thompson, L.E. Wenger, Structure of molybdenum-phosphate glasses by X-ray photoelectron spectroscopy (XPS), J. Non-Cryst. Solids, 212(2-3) (1997) 180-191.

[33] G. Tai, T. Zeng, J. Yu, J. Zhou, Y. You, X. Wang, H. Wu, X. Sun, T. Hu, W. Guo, Fast and large-area growth of uniform MoS_2 monolayers on molybdenum foils, Nanoscale, 8(4) (2016) 2234-2241.

[34] F. Esch, S. Fabris, L. Zhou, T. Montini, C. Africh, P. Fornasiero, G. Comelli, R. Rosei, Electron localization determines defect formation on ceria substrates, Science 309(5735) (2005) 752-755.

[35] X.P. Wu, L. Gagliardi, D.G. Truhlar, Cerium Metal-Organic Framework for Photocatalysis, J. Am. Chem. Soc., 140(25) (2018) 7904-7912.

[36] H. Giang, T. Nguyen, N.M. Schweitzer, C.-Y. Chang, T.L. Drake, M.C. So, P.C. Stair, O.K. Farha, J.T. Hupp, S.T. Nguyen, Vanadium-Node-Functionalized UiO-66: A Thermally Stable MOF-Supported Catalyst for the Gas-Phase Oxidative Dehydrogenation of Cyclohexene, ACS Catal. 4(8) (2014) 2496-2500.

[37] M. Wen, Y. Kuwahara, K. Mori, D. Zhang, H. Li, H. Yamashita, Synthesis of Ce ions doped metal–organic framework for promoting catalytic H$_2$ production from ammonia borane under visible light irradiation, J. Mater. Chem. A, 3(27) (2015) 14134-14141.

[38] F. Nouar, M.I. Breeze, B.C. Campo, A. Vimont, G. Clet, M. Daturi, T. Devic, R.I. Walton, C. Serre, Tuning the properties of the UiO-66 metal-organic framework by Ce substitution, Chem. Commun., 51(77) (2015) 14458-14461.

[39] Z.J. Lin, H.Q. Zheng, Y.N. Zeng, Y.L. Wang, J. Chen, G.J. Cao, J.F. Gu, B.L. Chen, Effective and selective adsorption of organoarsenic acids from water over a Zr-based metal-organic framework, Chem. Eng. J., 378 (2019) 122196.

[40] H.N. Abdelhamid, G.A. Mahmoud, W. Sharmouk, A cerium-based MOFzyme with multi-enzyme-like activity for the disruption and inhibition of fungal recolonization, J. Mater. Chem. B, 8(33) (2020) 7548-7556.

[41] J. He, J. Wang, Y. Chen, J. Zhang, D. Duan, Y. Wang, Z. Yan, A dye-sensitized Pt@UiO-66(Zr) metal-organic framework for visible-light photocatalytic hydrogen production, Chem. Commun., 50(53) (2014) 7063-7066.

[42] Sodium Pertechnetate (^{99m}Tc) Injection (Non-Fission): Final text for addition to the International Pharmacopoeia, World Health Organization Document, 2009.

[43] V.S. Le, ^{99m}Tc generator development: up-to-date ^{99m}Tc recovery technologies for increasing the effectiveness of ^{99}Mo utilization, Sci. Technol. Nucl. Install., 2014 (2014) 1-41.

Supporting information

S-1 Gamma irradiation

The irradiation facility (GC220) was equipped with cobalt-60 sources (as shown in Figure S4.1) having half-life of 5.272 years. ~100 mg of UiO-66 (Ce) was packaged in a Posthumus plastic capsule in air and then the capsule was exposed to different gamma radiation doses (100 KGy, 350 KGy and 550 KGy).

S-2 Evaluation of the performance of UiO-66 (Ce) as sorbents in the ^{99}Mo/^{99m}Tc generator

Column fabrication

A plastic column with an inner diameter of 0.6 cm was fabricated with ~150 mg of UiO-66 (Ce). A filter and some cotton wools were placed at the bottom of the column, as shown in Figure S2. The column was conditioned by passing HCl solution at pH 3. The whole system was derived using a multi-channel peristaltic pump. All experiments were carried out within a shield on the lead brick wall.

Preparation of ^{99}Mo solution

About 20 mg of MoO_3 (>99.95%) in the form of powder, the enriched target material, was sealed in a plastic capsule and was irradiated for 3 h by neutrons at the reactor of the Institute for Energy Security and Environmental Safety Centre for Energy Research, Hungary. The irradiated [^{99}Mo]MoO_3(~67 MBq) and 355 mg of non-radioactive MoO_3 were dissolved into deionized water containing 300 mg of NaOH. Then the above solution was stirred using a magnetic rotor until all powder was dissolved. After that, the pH of the solution was adjusted to 3 and the total volume of the Mo solution was titrated to 25 mL. Eventually, the concentration of molybdenum solution was 10 mg/mL.

The adsorption and separation characteristics of UiO-66 (Ce)

The prepared column was fed with 4 ml of ^{99}Mo solution (5 mg/mL) at a flow rate of 0.15 ml/min. The loaded column was washed using 50~100 mL of saline solution (0.9% NaCl). Then the column was eluted every 24 h using 12 ml of saline solution over a period of two

weeks. Finally, the activity of ^{99}Mo and ^{99m}Tc (740 keV for ^{99}Mo and 141 keV for ^{99m}Tc) for the eluted solution was collected with a gamma counter (Wallac Wizard 2480, PerkinElmer). The elution yield was evaluated according to the following equation:

$$[^{99m}Tc \text{ activity in the eluted fraction}]/ [\text{expected } ^{99m}Tc \text{ activity}]$$

The expected activity of ^{99m}Tc was calculated by the following formula:

$$A_e = 0.88(\frac{\lambda_2}{\lambda_2 - \lambda_1})A(e^{-\lambda_1 t} - e^{-\lambda_2 t}) \qquad (1)$$

A_e is the activity of the daughter (^{99m}Tc) and A is the activity of the parent (^{99}Mo) at the time of last elution; λ_1 and λ_2 are the decay constant of the parent ($\frac{\ln2}{66}$=0.0105) and daughter ($\frac{\ln2}{6}$=0.1155), respectively; 0.88 is the fraction of ^{99}Mo that decays to ^{99m}Tc (the other 12% directly decays to Tc-99); t is the time since the last elution. The ^{99}Mo breakthrough was calculated by the following equation:

$$[^{99}Mo \text{ activity in the eluted fraction}]/[^{99}Mo \text{ activity} +^{99m}Tc \text{ activity in the eluted fraction}]$$

In addition, the cerium breakthrough and molybdenum breakthrough were the concentration of Ce and Mo in each eluted fraction, respectively. Their concentrations were determined by inductively coupled plasma optical emission spectroscopy (ICP-OES, Optima 4300 DV, Perkin Elmer) after the decay of ^{99}Mo.

S-3 Adsorption kinetic models

The equation of pseudo-first-order, pseudo-second-order kinetic and intraparticle diffusion models are displayed as following:

$$ln (q_e - q_t) = ln\, q_e - K_1 t \qquad (2)$$

$$\frac{t}{q_t} = \frac{t}{q_e} + \frac{1}{K_2 q_e^2} \qquad (3)$$

$$q_t = K_3 t^{0.5} + C \qquad (4)$$

Where q_e and q_t are adsorption capacity (mg/g) at equilibrium and time t (min), respectively. K_1, K_2 and K_3 adsorption rate constant of pseudo-first-order, pseudo-second-order kinetic and intraparticle diffusion model, respectively. t (min) is the reaction time.

The equations of Langmuir and Freundlich models are displayed as following:

$$q_e = \frac{K_L Q_m C_e}{1 + K_L C_e} \qquad (5)$$

$$q_e = K_F C_e^{1/n} \qquad (6)$$

where K_L and K_F denote the Langmuir and Freundlich constants, respectively. Q_m is the Langmuir maximum adsorption capacity. q_e represents Mo adsorption capacity at equilibrium and C_e is the residual concentration of Mo solution at equilibrium.

Figure S4.1. The facility of Cobalt-60 sources.

Figure S4.2. Photos of column experimental set up (left) and the fabricated column (right).
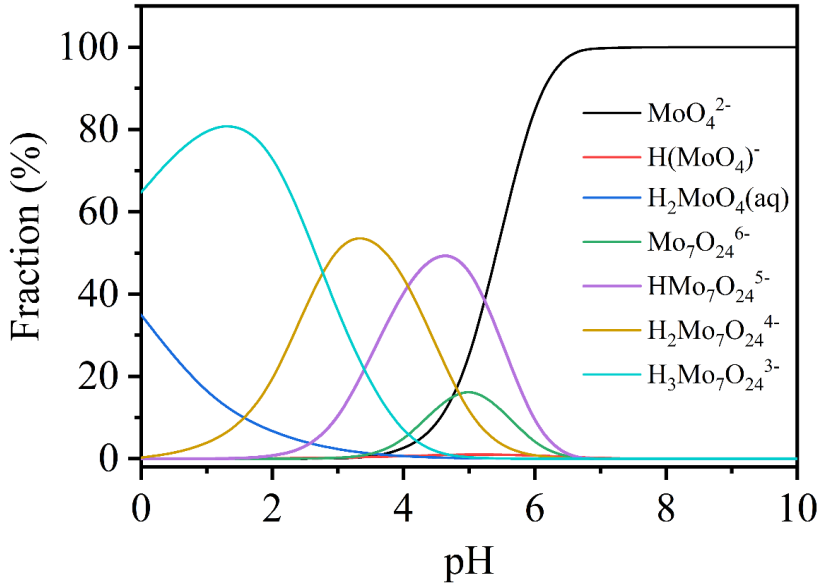
Figure S4.3. Molybdenum speciation in solution as a function of Ph by CHEAQS when molybdenum concentration is 5 mg/mL.
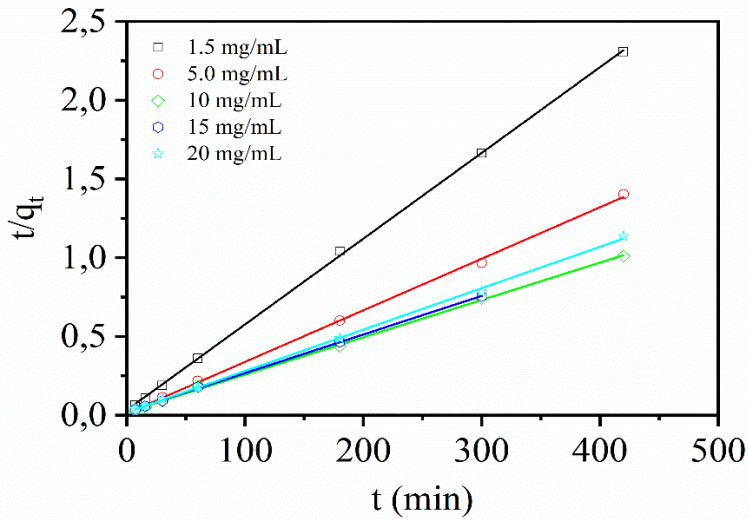

Figure S4.4. Linear fits of the adsorption kinetics of UiO-66 (Ce) by the pseudo-second-order model at pH 3.
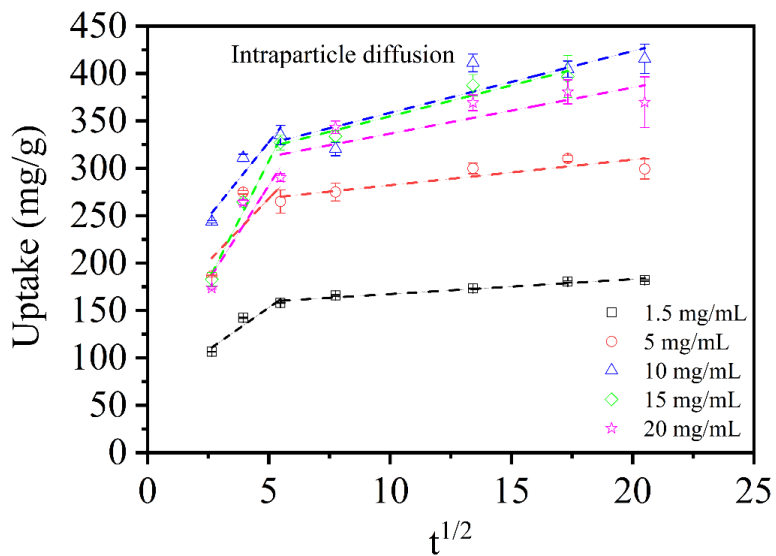
Figure S4.5. The adsorption kinetics of UiO-66 (Ce) fitted by the intraparticle diffusion model at pH 3.
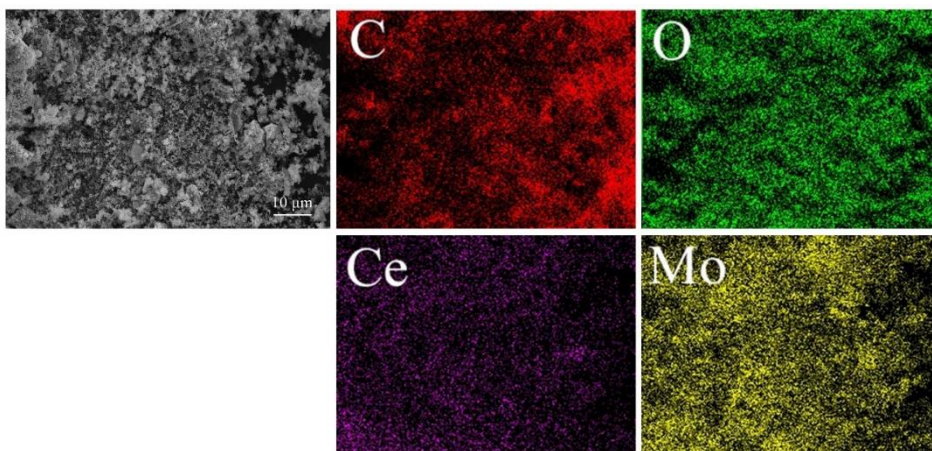

Figure S4.6. SEM image and EDS mapping of UiO-66 (Ce) after molybdenum adsorption.
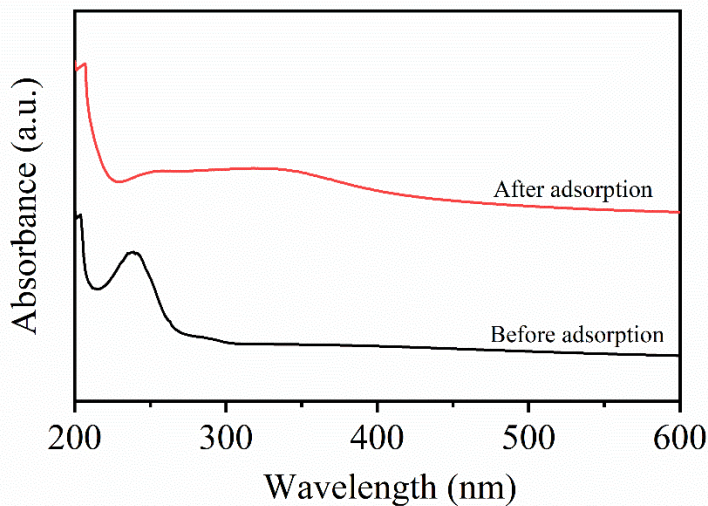
Figure S4.7. The ultraviolet spectrum of UiO-66 (Ce) before and after molybdenum adsorption.

Table S4.1. The liner fitting parameters of adsorption kinetic models.

C_0 (mg/mL)	Pseudo-first order			Pseudo-second order		
	Q_e, calcd (mg/g)	K_1 (min^{-1})	R_2	q_e, calcd (mg/g)	K_2 (g/mg·min)	R_2
1.5	47.5	0.0110	0.904	183.8	0.0009	0.997
5	52.6	0.0045	0.520	305.8	0.0009	0.999
10	124.8	0.0108	0.661	421.9	0.0003	0.999
15	261.3	0.0267	0.921	408.2	0.0003	1.000
20	100.2	0.0064	0.626	380.2	0.0004	0.999

Table S4.2. The calculated parameters of the intraparticle diffusion model

Concentration (mg/mL)	The first stage			The second stage		
	K_3	C	R_2	K_3	C	R_2
1.5	17.91	63.58	0.928	1.57	151.62	0.962
5	26.68	134.79	0.709	2.70	255.19	0.796
10	31.73	169.09	0.913	6.51	293.55	0.805
15	50.63	54.71	0.983	6.53	89.64	0.953
20	40.36	80.35	0.878	4.86	287.97	0.707

Table S4.3. The calculated parameters of adsorption models.

Samples	Langmuir Parameters			Freundlish Parameters		
	Q_m	K_L	R^2	$1/n$	K_F	R^2
Ce MOFs	485	0.549	0.997	0.32	224	0.983

Table S4.4. Comparison of the Mo adsorption capacity of various adsorbents.

Adsorbents	Mo adsorption capacity (mg/g)	Surface area (m²/g)	Initial Mo concentration	Ref.
TUD-1	112	402	2.6 mM	[1]
Hydrous TiO$_2$	230	--	--	[2]
Hydrous MnO$_2$	50	--	150 mg/mL	[3]
Al-dropped mesoporous SiO$_2$	16.8	463	10 mg/mL	[4]
Mesoporous γ-Al$_2$O$_3$	56.2	251	--	[5]
Nanocrystalline γ-Al$_2$O$_3$	200	252	10 mg/mL	[6]
Macro/mesoporous γ-Al$_2$O$_3$	250	542	10 mg/mL	[7]
Al^{99}Mo gel	364	--	100 mg/mL	[8]
UiO-66 (Zr)	335	1624	20 mg/mL	[9]
Form-UiO-66	296	1653	20 mg/mL	[9]
UiO-66-NH$_2$	131	295	20 mg/mL	[9]
UiO-66-NO$_2$	227	575	20 mg/mL	[9]
UiO-66 (Ce)	475	1140	20 mg/mL	This work

Table S4.5. Summary of elemental contents of UiO-66 (Ce) after molybdenum adsorption by EDS analysis.

Elements	Mass (%)	Atom (%)
C	25.31	47.77
O	30.62	43.39
Ce	21.11	3.42
Mo	22.96	5.42

Table S4.6. Percentage of Ce XPS peak before and after Mo adsorption.

	Ce-MOFs		Ce-MOFs-Mo	
	Binding energy (eV)	Percentage	Binding energy (eV)	Percentage
Ce 3d$_{3/2}$	916.64	8.60 %	916.43	6.91 %
	906.70	6.28 %	906.53	5.63 %
	903.55	10.97 %	903.58	12.58 %
	901.05	9.44 %	901.04	12.61 %
	898.40	15.48 %	898.29	11.51 %
Ce 3d$_{5/2}$	888.57	5.82 %	887.18	5.24 %
	885.71	16.46 %	885.24	22.93 %
	882.57	28.52 %	882.07	23.96 %

Table S4.7. Percentage of C XPS peak before and after Mo adsorption.

	Ce-MOFs		Ce-MOFs-Mo	
	Binding energy (eV)	Percentage	Binding energy (eV)	Percentage
C 1s	290.10	6.16%	290.19	2.15%
	288.04	18.89 %	288.12	18.76 %
	285.24	21.83 %	285.24	33.83 %
	284.11	55.05 %	283.88	46.44 %

**Table S4.8.** Elution performance of UiO-66 (Ce) in the ^{99}Mo/^{99m}Tc generator for four days

Elution No.	Time of ingrowth (h)	Elution efficiency (%)	^{99}Mo breakthrough (%)
1	24	96.2	0.51
2	24	90.8	0.53
3	24	90.4	0.39
4	24	93.6	0.54

References

[1] A.G. Denkova, B.E. Terpstra, O.M. Steinbach, J.t. Dam, H.T. Wolterbeek, Adsorption of Molybdenum on Mesoporous Aluminum Oxides for Potential Application in Nuclear Medicine, Sep. Sci. Technol. 48(9) (2013) 1331-1338.

[2] Q.M. Qazi, M. Ahmad, Preparation and evaluation of hydrous titanium oxide as a high affinity adsorbent for molybdenum (^{99}Mo) and its potential for use in ^{99m}Tc generators, Radiochimica. Acta, 2011 231.

[3] R. Chakravarty, R. Shukla, S. Gandhi, R. Ram, A. Dash, M. Venkatesh, A.K. Tyagi, Polymer embedded nanocrystalline titania sorbent for ^{99}Mo/^{99m}Tc generator, J. Nanosci. Nanotechnol., 8(9) (2008) 4447-4452.

[4] Y. Suzuki, T. Kitagawa, Y. Namekawa, M. Matsukura, K. Nishikata, H. Mimura, K. Tsuchiya, Molybdenum adsorption and desorption properties of alumina with different surface structures for ^{99}Mo/^{99m}Tc generators, Trans. Mater. Res. Soc. Jpn., 43(2) (2018) 75-80.

[5] J. Serrano Gómez, F. Granados Correa, ^{99m}Tc generator with hydrated MnO_2 as adsorbent of ^{99}Mo, J. Radioanal. Nucl. Chem., 254(3) (2002) 625-628.

[6] R. Chakravarty, R. Ram, A. Dash, M.R. Pillai, Preparation of clinical-scale ^{99}Mo/^{99m}Tc column generator using neutron activated low specific activity ^{99}Mo and nanocrystalline gamma-Al_2O_3 as column matrix, Nucl. Med. Biol., 39(7) (2012) 916-22.

[7] J. Wang, R. Gao, Q. Huang, X. Yin, M. Lin, S. Cao, D. Chen, F. Fan, X. Wu, Z. Qin, Z. Guo, J. Bai, J. Chu, W. Tian, C. Tan, B. Li, N. Cheng, Z. Jia, Practicality of hierarchically macro/mesoporous gamma-Al_2O_3 as a promising sorbent in the preparation of low specific activity ^{99}Mo/^{99m}Tc generator, Appl. Radiat. Isot., 178 (2021) 109986.

[8] M. Amin, M.A. El-Amir, H.E. Ramadan, H. El-Said, ^{99}Mo/^{99m}Tc generators based on aluminum molybdate gel matrix prepared by nano method, J. Radioanal. Nucl. Chem., 318(2) (2018) 915-922.

[9] C. Ma, A. Vasileiadis, H.T. Wolterbeek, A.G. Denkova, P. Serra Crespo, Adsorption of molybdenum on Zr-based MOFs for potential application in the ^{99}Mo/^{99m}Tc generator, Appl. Surf. Sci., 572 (2022) 151340.

Effects of high gamma doses on the structural stability of metal-organic frameworks

5
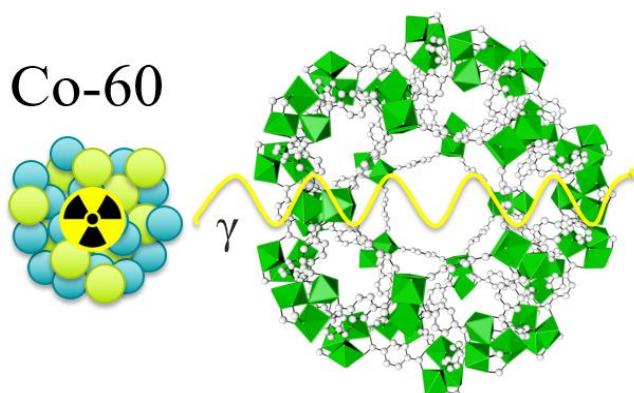
Abstract

Four different MOFs were exposed to gamma rays by a cobalt-60 source reaching a maximum dose of 5 MGy. The results showed that the MIL-100 (Cr) and MIL-100 (Fe) did not exhibit obvious structural damage, suggesting their excellent radiation stability. MIL-101 (Cr) showed good radiation stability up to 4 MGy, but its structure started degrading with increasing radiation dose. Furthermore, the results showed that the structure of AlFu MOFs started to decompose at a gamma dose of 1 MGy, exhibiting a much lower tolerance to gamma radiation. At this radiation energy, the dominant interaction of the gamma-ray with MOFs is the Compton effect and the radiation stability of MOFs can be improved by prolific aromatic linkers, high linker connectivity and good crystallinity. The results of this study indicate that MIL-100 and MIL-101 MOFs have a good potential to be employed in nuclear applications, where relatively high radiation doses play a role, e.g. nuclear waste treatment and radionuclides production.

5.1 Introduction

In recent years, the increasing energy demand has renewed the interest in nuclear energy especially since it is an effective way to achieve carbon dioxide neutral energy production [1]. Nevertheless, nuclear waste is still a major concern and has resulted in studies aiming at better waste management in which separation or sequestration of the different radionuclides is essential, especially in the long-run. On top of that, the production of radionuclides of medical interest is also a major topic in the nuclear filed [2].

Metal-organic frameworks (MOFs) materials have been investigated extensively as adsorbents for nuclear waste treatment as well as for radionuclide production, due to their high specific surface area, tunable functional groups allowing high selectivity and good chemical stability [3-6]. For instance, several MOFs have shown outstanding performance in the field of radioactive gas separation (^{85}Kr, ^{129}I, ^{135}Xe and ^{222}Rn) [7-11], seawater purification [12-14], radionuclide adsorption for wastewater remediation (^{59}Fe, ^{65}Zn, ^{137}Cs and ^{235}U) [15-24] and radionuclide production [25]. Although these MOFs have excellent chemical stability and have shown great potential in waste treatment application, their resistance to ionizing radiation has hardly been reported. To fully exploit the potential of MOFs in these fields, it is imperative to determine their radiation resistance. So far, the stability of only a few MOFs has been investigated under gamma radiation. For example, A series of SIFSIX-3 MOFs have been studied under beta and gamma irradiation by Elsadi et al., who reported that SIFSIX-3-Cu had the best radiation resistance to gamma and beta radiation up to a dose of 50 kGy and 25 MGy, respectively [22]. The radiation stability of several MOFs with different metals (Al, Zr, Cu, Zn) has been studied under different gamma doses and the results have demonstrated that MIL-100 (Al) shows the best radiation tolerance, i.e. 2 MGy [23]. Gilson et al. have developed a thorium-based MOF, which has survived gamma radiation up to a dose of 4 MGy and a dose of α particles up to 25.5 MGy [26]. Furthermore, Nenoff et al. have investigated the influence of gamma dose rates (0.78 Gy/min, 3days and 423.3 Gy/min, 23 min) on the stability of NU-1000 and UiO-66, and found that NU-1000 exhibits better stability because of its high linker connectivity and lower node density [27]. However, the radiation resistance of many other promising MOFs and especially at higher gamma radiation dose remains unknown.

MIL-101 (Cr), possessing high surface area and excellent chemical stability, has shown good potential to separate radionuclides [28]. In addition, this MOF can also be applied to produce the ^{51}Cr radionuclide, which is widely used to label platelets and red blood cells, and to evaluate their lifespan in clinical application and is desired radionuclide, requiring high specific activity (high activity per unit mass). Achieving high specific activity with nuclear reactors is hard but would be possible by the combination of Cr-based MOFs and hot atom approaches (Szilard-Chalmers effect) [29]. In order to realize the application of MIL-101 (Cr) in a highly radioactive environment, the effects of gamma radiation on its structural evolution need to be explored. At the same time, it is very interesting to determine the influence of organic linkers and metal clusters on the radiation stability of MOFs in a more systematic fashion allowing rational choice of a MOF according to its application. Therefore, MIL-100 (Fe), MIL-100 (Cr) and aluminum fumarate MOFs (AlFu MOFs) have been studied and compared. The structure of these MOFs and corresponding organic linkers are shown in Figure 5.1. All MOFs in this study have been irradiated by gamma-ray from 0 Gy to 5 MGy and their structural changes were monitored by XRD, SEM, FT-IR and nitrogen adsorption.
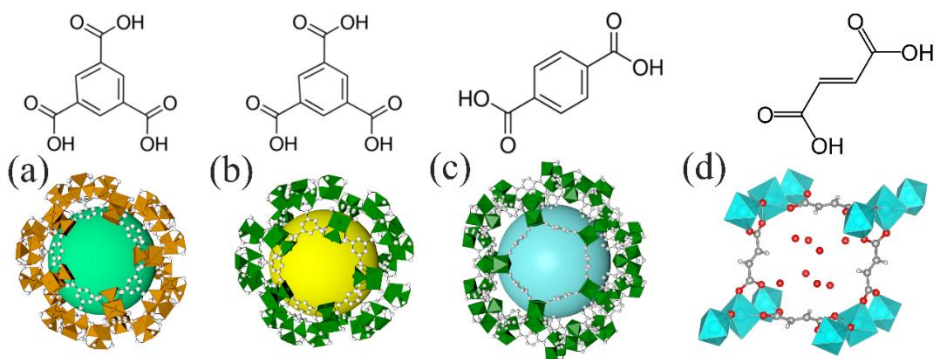

Fig. 5.1. Illustration of the structure and corresponding organic linkers of (a) MIL-100 (Fe), (b) MIL-100 (Cr), (c) MIL-101 (Cr) and AlFu MOFs. Iron, chromium, aluminum, carbon and oxygen atoms are denoted in orange, green, blue, grey and red colors, respectively.

5.2 Experimental sections

5.2.1 Synthesis and Characterization

MIL-100 (Cr), MIL-100 (Fe), MIL-101 (Cr) and aluminum fumarate (AlFu) MOFs were synthesized according to previous literature [30-33]. The details of the synthesis are shown in the supporting information.

Powder X-ray diffraction patterns of the synthesized MOFs were obtained by a PANalytical X'Pert Pro pw3040/60 diffractometer with Cu Kα radiation operating at 45 kV and 40 mA. Brunauer-Emmett-Teller (BET) surface area of the samples was collected on a Micromeritics Tristar II at 77 K and all samples were pretreated at 200 °C for 15 h before measurement. Fourier transform infrared spectra (FTIR) of powder samples was directly measured by a PerkinElmer Spotlight 400 FT-IR spectrometer with a range of 650~2500 cm^{-1}. The morphology and particle size of the samples were determined by scanning electron microscopy (SEM, JEOL, JSM-IT100). X-ray photoelectron spectra (XPS) was collected using a ThermoFisher Al K-alpha apparatus and scans were performed by a 400 µm spot size with an energy step size of 0.2 eV. The thermal stability of four MOFs was investigated by Thermogravimetric analysis (TGA) using a Mettler-Toledo/STDA 851e apparatus with a heating rate of 5 °C/min.

5.2.2 Gamma irradiation

The gamma source (GC220) is an irradiation cell using the radionuclide ^{60}Co (as shown in Figure S5.1), which was used to study the effects of gamma irradiation on the selected MOFs. The cobalt-60 (1.17, 1.33 MeV) source has a half-life of 5.272 years. ~0.2 g of powder of each sample was packed in Posthumus plastic capsules in air and irradiated for different times to achieve different doses. The gamma dose was calculated according to the following equation:

$$D=\int_0^{\dot{D}} \dot{D}(t)dt=D_0\int_0^T e^{-\lambda t}dt=\frac{\dot{D}}{\lambda}(1-e^{-\lambda T})$$

Where D and $\dot{D}$ are dose and dose rate respectively. The initial dose rate was 0.65 kGy/h and λ (3.6×10^{-4} d^{-1}) is the decay constant of ^{60}Co. The radiation time (T) was 32.8 days (0.5 MGy), 66 days (1.0 MGy), 99 days (1.5 MGy), 133 days (2.0 MGy), 199 days (3.0 MGy), 269 days (4.0 MGy) and 340.5 days (5.0 MGy), respectively.

5.3 Results

To evaluate the radiation stability, the structure changes or the loss of crystallinity of the synthesized MOFs were monitored through XRD, SEM, FT-IR and nitrogen adsorption after exposure to a cobalt-60 source at different doses of gamma radiation. Figure 5.2 shows the XRD patterns of MIL-100 (Fe), MIL-100 (Cr), MIL-101 (Cr) and AlFu MOFs before and after the irradiation at different gamma radiation doses. Their diffraction peaks are consistent with the simulated patterns for each material. After exposure to different gamma radiation doses, the diffraction peaks of MIL-100 (Fe) (Figure 5.2 (a)), MIL-100 (Cr) (Figure 5.2 (b)) and MIL-101 (Cr) (Figure 5.2 (c)) maintained the same diffraction patterns. The full-width half-maximum (FWHM) of the most intense peak in XRD patterns was analyzed and shown in Figure S5.2. There is a small variation in the values of FWHM for MIL-100 (Fe) and MIL-100 (Cr). The values of FWHM for MIL-101 (Cr) increased slightly at relatively low radiation dose (from 0 to 4 MGy) and the value increased significantly (22%) when exposed to 5 MGy, showing severe loss of crystallinity. The diffraction peaks of AlFu MOF became broader as the gamma dose increased (Figure 5.2 (d)). When the gamma radiation dose was lower than 1 MGy, the FWHM of AlFu MOF remained stable. The value of FWHM increased from 0.4 to 0.51 after receiving 2 MGy of gamma irradiation, resulting in broader diffraction peaks.

The surface area of the four materials was determined by N_2 adsorption at 77 K. Figure 5.3 (a) shows the N_2 adsorption-desorption isotherms of MIL-100 (Fe) after exposure to the different gamma doses. MIL-100 (Fe) possessed type I adsorption isotherm and had a surface area of 1574 m^2/g. After exposure of 1 and 2 MGy, its surface area was 1527 and 1528 m^2/g (having a 3% drop), respectively. When MIL-100 (Fe) was exposed to higher irradiation doses (between 3 and 5 MGy) its surface area decreased to 1513 m^2/g, 1498 m^2/g and 1507 m^2/g (as shown in Table S5.1). The SEM images in Figure S5.3 show that MIL-100 (Fe) exhibited a rod-like shape with inhomogeneous size. There were no detectable changes observed to the particle morphology and size after the different radiation exposures. The FT-IR spectrum of MIL-100 (Fe) can be found in Figure S5.4. The spectrum displays two peaks at 1625 cm^{-1} and 1382 cm^{-1} that are attributed to asymmetric and symmetric vibrations of carboxyl groups [34], respectively. The peak at around 1445 cm^{-1} is assigned to stretching

vibrations of the O-C-O group [35]. No obvious changes can be observed in the FT-IR spectra, which is consistent with the XRD analysis.
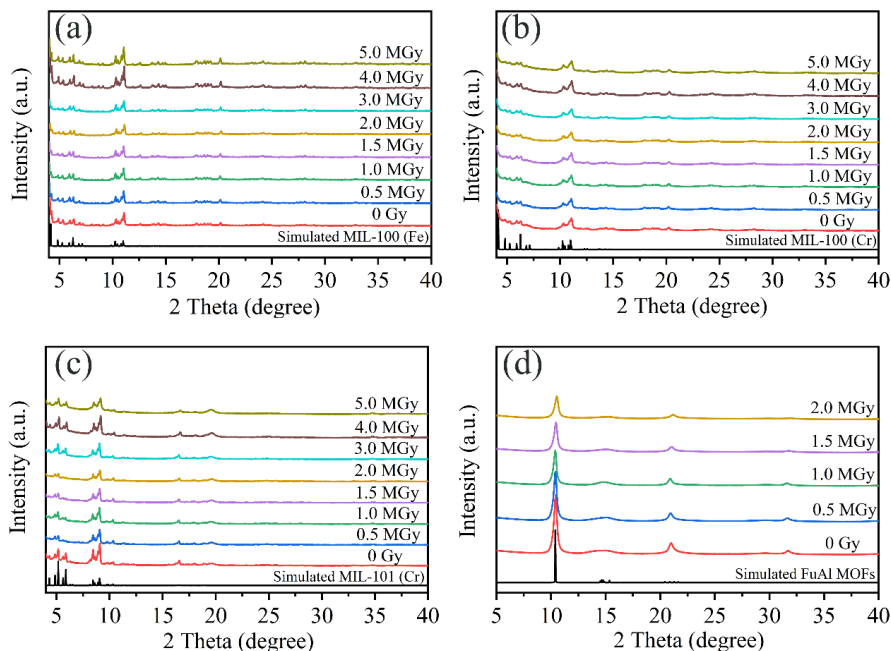

Fig. 5.2. XRD patterns of (a) MIL-100 (Fe), (b) MIL-100 (Cr), (c) MIL-101 (Cr) and (d) FuAl MOFs exposed to different gamma doses.

Figure 5.3 (b) shows the N_2 adsorption isotherms of MIL-100 (Cr) after different gamma irradiation doses. The BET surface area of MIL-100 (Cr) calculated from nitrogen adsorption isotherm was 1862 m^2/g before gamma irradiation. The shape of the adsorption isotherms was the same as that of fresh MIL-100 (Cr), but they were found to decrease gradually in adsorption capacity. Correspondingly, their surface area decreased by 3.2% (1802 m^2/g), 6.3% (1744 m^2/g,) 10.8% (1660 m^2/g), 14.1% (1600 m^2/g) and 18.9% (1510 m^2/g) after receiving gamma doses of 1 MGy, 2 MGy, 3 MGy, 4 MGy and 5 MGy, respectively, where there was an approximately 4% decrease in surface area for each gamma dose. SEM images (Figure S5.5) showed that the morphology of MIL-100 (Cr) was unchanged. But the crystal size decreased a little after high gamma radiation exposure (4 MGy and 5 MGy). The FT-IR spectrum of MIL-100 (Cr) was measured (as shown in Figure S5.6) and no obvious changes could be observed with gamma radiation up to 5 MGy.
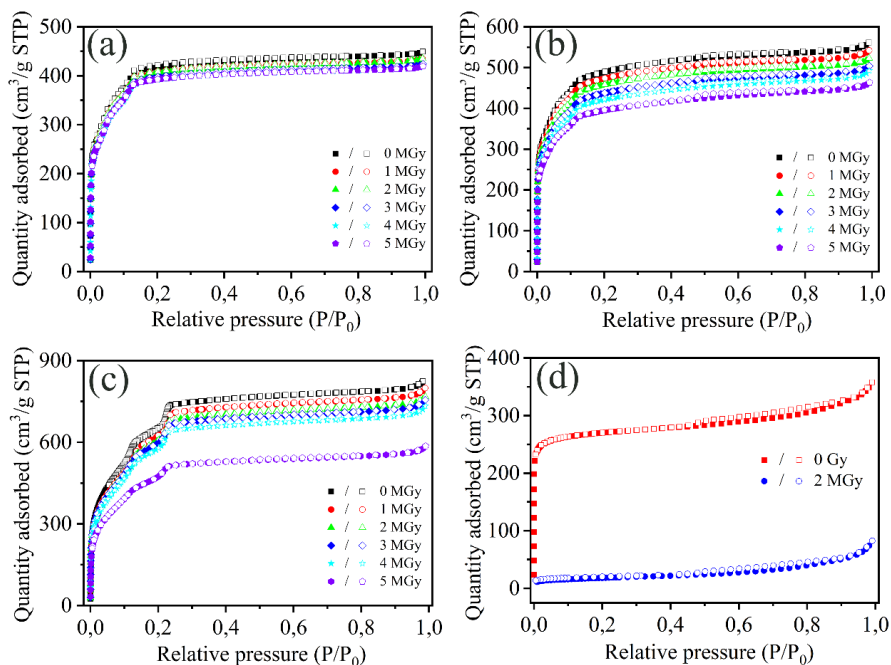
Fig. 5.3. N_2 adsorption isotherms of (a) MIL-100 (Fe), (b) MIL-100 (Cr), (c) MIL-101 (Cr) and (d) FuAl MOFs exposed to different gamma doses.

Nitrogen adsorption isotherms of MIL-101 (Cr) after exposure to the different gamma doses are shown in Figure 5.3 (c). The BET surface area of the fresh sample was 2203 m^2/g. After receiving gamma doses of 1 MGy, 2 MGy, 3 MGy and 4 MGy, the BET surface area of MIL-101 (Cr) decreased from 2203 m^2/g to 2159 m^2/g, 2101 m^2/g, 2072 m^2/g and 2099 m^2/g, respectively (Table S5.1). The BET surface area of MIL-101 (Cr) was reduced by only 4.7 % when exposed to a gamma dose of 4 MGy. When the gamma dose reached 5 MGy, MIL-101 (Cr) decreased by 20.0% in surface area (1762 m^2/g). Its micropore volume decreased from 1.0715 cm^3/g to 0.7508 cm^3/g (30% reduction, as shown in Table S5.2). Additionally, the microstructure and morphology of MIL-101 (Cr) particles were examined by SEM, as shown in Figure S5.7. The images show that the MIL-101 (Cr) particles are irregular spheres with a relatively uniform distribution. The morphology and size of the particles did not show any obvious changes after exposure to different gamma doses.

Figure 5.3 (d) shows the N_2 adsorption isotherms of AlFu MOFs. The surface area of AlFu MOFs at 2 MGy had a significant decrease (63 m^2/g) when compared to the original surface area of 1070 m^2/g. SEM images in Figure S5.9 showed that the morphology of MIL-100 (Cr)

was unchanged. The damage to the structure of AlFu MOFs was further confirmed by FT-IR spectra (see Figure S5.10). The C=C vibrations at 1600 cm^{-1} and O-H bending vibrations of the aluminum clusters at 998 cm^{-1} could not be observed after 1 MGy radiation [36, 37].
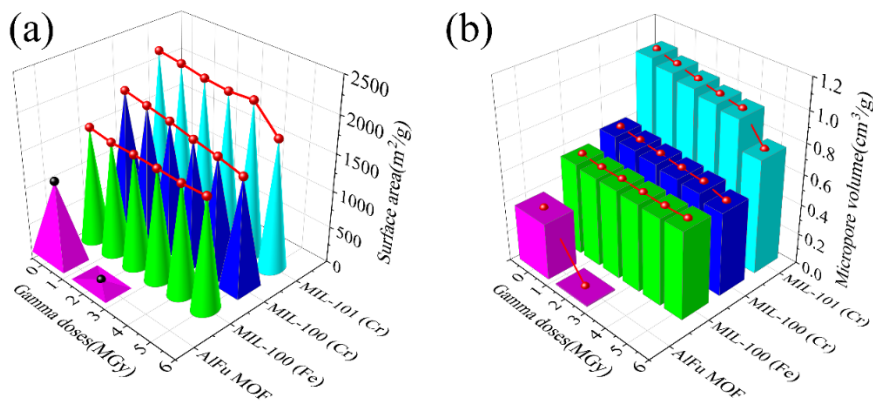

Fig. 5.4. 3D representations of the four MOFs (a) surface area and (b) micropore volume as function of the gamma radiation dose. Red lines represent the observed trend with increasing gamma dose.

5.4 Discussion

The radiation stabilities of four MOFs were explored by determining their most important characteristics (e.g. crystallinity). The small fluctuation value of FWHM and the lack of significant reduction in BET surface area (Figure 5.4a) after receiving gamma radiation of 5 MGy indicate that MIL-100 (Fe) has excellent radiation stability towards gamma radiation. After exposure to a gamma radiation dose of 5MGy, the XRD pattern and FWHM of MIL-100 (Cr) did not have obvious changes, suggesting that it kept good crystallinity. Although a small decrease in surface area and micropore volume (Figure 5.4b) could be observed with increasing gamma doses, MIL-100 (Cr) showed tenacious resistance to gamma irradiation, exhibiting as good radiation stability as MIL-100 (Fe). The TGA curves also demonstrated that they still kept good thermal stability after receiving 5 MGy of gamma irradiation (see in Figure S5.11). Furthermore, MIL-101 (Cr) showed the same performance as MIL-100 (Cr) when it was irradiated by gamma rays at doses of 1, 2, 3, and 4 MGy. Its surface area and micropore volume had a slight decrease, but it also demonstrated that this MOF is highly resistant up to 4 MGy of a gamma dose. Subsequently, its surface area decreased significantly

(20%) and the FWHM value also increased visibly, suggesting that the structure of MIL-101 (Cr) started decomposing at a gamma dose of 5 MGy, causing lower decomposing temperature (see the Figure S5.11 (c)). In addition, the crystallinity of AlFu MOF began to degenerate after receiving 1 MGy of gamma radiation and its pore structure characteristics completely disappeared at a gamma dose of 2 MGy, exhibiting much lower radiation stability, which could also be proved by the TGA curve (Figure S5.11 (d)). Why the different MOFs react differently when exposed to gamma radiation is not clear but there seem to be certain clues that can explain why one material is more stable than another.

Three main processes rule the interaction of gamma-ray with matter, namely the photoelectric effect, the Compton effect, and the pair production. The probability of these interactions strongly depends on the atomic number (Z) and the energy of gamma-ray [38]. The Compton effect is expected to be the most dominant based on the gamma energy ($E\gamma$=1.17, 1.33 MeV) and the Z of the elements comprising the MOFs. The Compton process consists in a partial transfer of energy to an electron in the MOF resulting in the energy loss of the gamma radiation, which can then further interact with other electrons, accompanied by the second Compton effect or photoelectric effect, and thus generating recoil electrons (Figure 5.5 (a)). Some of the Compton electrons could travel to air without collision and the other electrons can collide with the orbital electrons of surrounding atoms in the MOFs by incoherent scattering, causing ionizations or excitations (Figure 5.5 (b)). Finally, the energy of the excited atoms can be dissipated through the emission of fluorescence or Auger electrons, and, in the last instance, through vibration (heat dissipation).

As discussed above, the structure of the MOF seems to affect its stability towards radiation. First, the mass-energy absorption coefficient is an effective index to measure the average fraction of photon energy absorbed by materials. Metal clusters of MOFs in this research consist of metal and oxygen atoms, which have a much higher total attenuation coefficient than organic linkers, suggesting that metal clusters can act as radiation antennas. As shown in Table 5.1, Al metal atom had the lowest photon cross-section, but AlFu MOF had the worse radiation stability compared with the other three MOFs, which could be attributed to the lack of aromaticity of the organic linkers. The aromatic linkers can promote delocalization and migration of excitations based on high energy delocalization [39, 40]. Therefore, the aromaticity of the linker has a significant impact on the radiation stability of MOFs under gamma-ray environment. Second, MIL-100 (Fe) and MIL-100 (Cr), which have the same

linker and crystal structure, showed good irradiation stability. The surface area of MIL-100 (Cr) reduced a little bit more (16%), although Cr has a lower photon cross-section. The larger FWHM value of MIL-100 (Cr) indicated that it had a worse crystallinity compared with MIL-100 (Fe). The formed defects could be not beneficial for the energy transfer and dissipation [41], resulting in low tolerance ability for gamma radiation, which could be the reason for the better stability of MIL-100 (Fe).
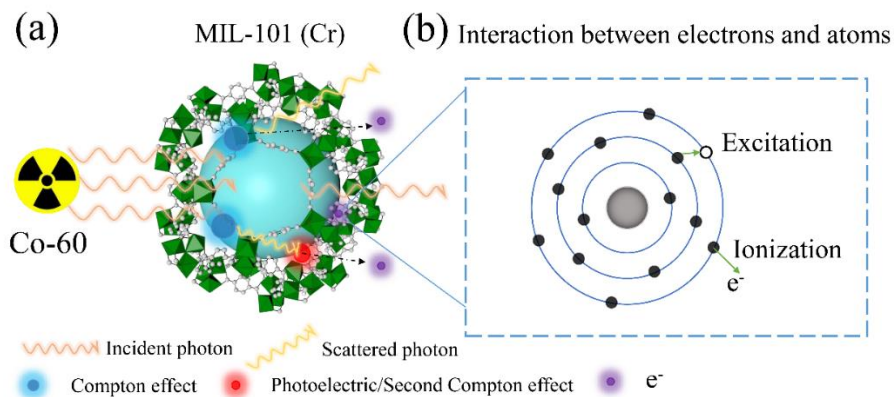

Fig. 5.5. Schematic illustration (a) of interactions between MIL-101 (Cr) with gamma-rays (b) interaction of traveled electrons with atoms in the framework of MOFs.

Table 5.1. Total photon cross sections (barns) of different metals, 1 barn = 10^{-24} cm^2

Metal	Energy (MeV)	Total Attenuation (barns/atom)
Al	1.17	2.55
	1.33	2.39
Cr	1.17	4.74
	1.33	4.44
Fe	1.17	5.51
	1.33	4.82
C	1.17	1.17
	1.33	1.09
O	1.17	1.56
	1.33	1.46
H	1.17	0.19
	1.33	0.18

Figure 5.6 shows the XPS spectra of MIL-100 (Cr) before and after a gamma radiation dose of 5 MGy. It can be seen that the sample contains Cr, O and C elements according to the XPS survey (Figure 5.6a). The Cr 2p spectrum is shown in Figure 5.6 (b) and two peaks at 577.6 eV and 587.2 eV are ascribed to Cr $2p_{3/2}$ and Cr $2p_{1/2}$, respectively [42]. The binding energy shifts cannot be observed suggesting that the metal clusters in MIL-100 (Cr) maintain integrity after exposure to a gamma dose of 5 MGy. The C 1s XPS (Figure 5.6 (c)) spectrum of MIL-100 (Cr) before irradiation could be deconvoluted into four peaks at binding energies of 284.8 eV, 286.2 eV, 288.5 eV and 290.6 eV, which were attributed to C-C/C-H, C-O, C=O and O-C=O/π-π, respectively [43]. The peaks ascribed to O-C=O/π-π and C-O positively shift to the binding energy of 291.6 eV and 286.3 eV, implying the decrease of electron density of the carboxyl groups [44]. The O1s spectrum of MIL-100 (Cr) (Figure 5.6 (d)) could be deconvoluted into three peaks at 531.9 eV, 534.2 eV and 536.1 eV, which were ascribed to Cr-O-Cr, Cr-O-C and O-C=O, respectively [45]. After gamma irradiation, the two peaks of Cr-O-C and O-C=O shift to higher binding energies by 0.2 and 0.1 eV, which were attributed to decreased electron density of the junction of metal clusters and organic linkers, indicating that the bonds between Cr-O clusters and the carboxylate of H_3BTC linkers could be partly broken during irradiation, resulting in the formation of defects. Third, MIL-100 (Cr) and MIL-101 (Cr), which have the same metal clusters but different connecting linkers, had good radiation stability under gamma radiation of 4 MGy. However, MIL-101 (Cr) started to decompose with increasing gamma dose, which is related to the linker connectivity. Since each linker in MIL-100 (Cr) is connected with three metal clusters and the structure can still be kept when one or two connection sites are broken, causing this material to exhibit better stability. Another possible explanation could be that the metal nodes concentration per volume unit of MIL-100 (Cr) is slightly higher than that of MIL-101 (Cr), indicating that closer metallic atoms might attenuate more the generated electrons, which is instrumental in stabilizing the structure of MOFs.

To better understand the relationship between structural characteristics and radiation stability of the MOFs, more systematic experiments need to be carried out to explore other possible factors that determine the stability of MOFs. In addition, more studies should be carried out to determine the maximum radiation dose that the MOFs can tolerate without loss of their characteristic properties.
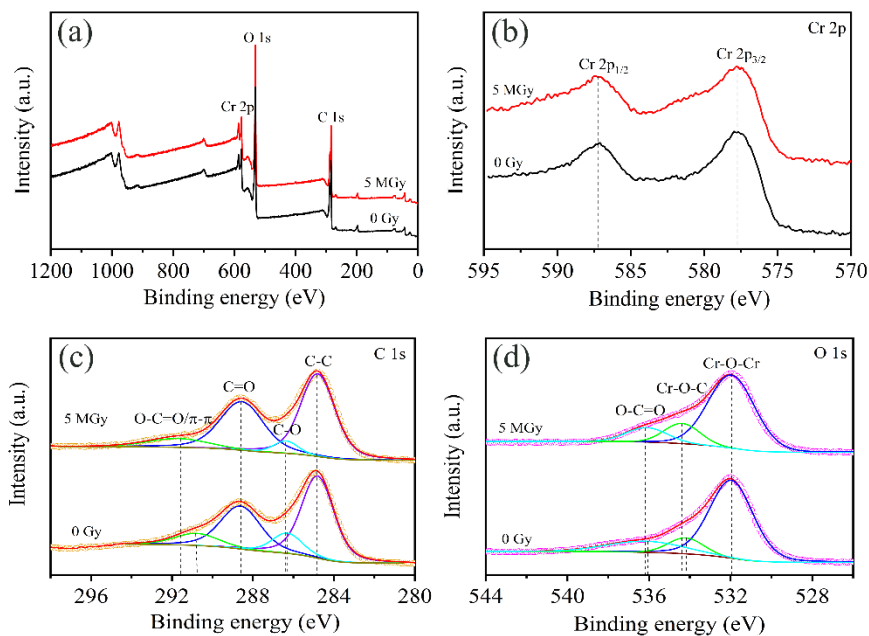
Fig. 5.6. XPS spectra of MIL-100 (Cr) before and after (5 MGy) gamma irradiation; (a) XPS survey, (b) Cr 2p, (c) C 1s and (d) O 1s

5.5 Conclusion

In conclusion, MIL-100 (Fe), MIL-100 (Cr), MIL-101 (Cr) and AlFu MOFs were prepared and irradiated using gamma rays at doses ranging from 0 Gy to 5 MGy. The structure of all materials was characterized by XRD, BET, SEM and FT-IR. The MIL-100 (Fe) and MIL-100 (Cr) presented outstanding stability when exposed to radiation of high doses (5 MGy). MIL-101 (Cr) exhibited good radiation stability when the material was subjected to gamma doses within a range of 0~4 MGy. A sudden decrease in the surface area demonstrated that MIL-101 (Cr) started to be damaged with increasing gamma dose. Meanwhile, the XRD results of AlFu MOF proved that the crystallinity of AlFu MOFs suffered a severe loss after receiving 1 MGy gamma dose. The BET and FI-IR results indicated that the structure of AlFu MOFs collapsed after exposure to high radiation dose. According to the structural analysis, the linker aromaticity plays an important role in the radiation stability of the MOFs. Additionally, high linker connectivity and good crystallinity of MOFs can also strengthen their radiation stability. To fully examine the potential of MOFs in nuclear applications their

resistance to even higher doses should be assessed in the future.

References

[1] H.C. zur Loye, T. Besmann, Amoroso, K. Brinkman, A. Grandjean, C. H. Henager, S. Hu, S. T. Misture, S. R. Phillpot, N. B. Shustova, H. Wang, R. J. Koch, G. Morrison, E. Dolgopolova, Hierarchical Materials as Tailored Nuclear Waste Forms: A Perspective. Chem. Mater. 30 (14) (2018) 4475-4488.

[2] S. Qaim, Nuclear data for production and medical application of radionuclides: Present status and future needs. Nucl. Med.Biol. 44 (2017) 31-49.

[3] S. Rojas, P. Horcajada, Metal-Organic Frameworks for the Removal of Emerging Organic Contaminants in Water. Chem. Rev. 120 (16) (2020) 8378-8415.

[4] Y. Bai, Y. Dou, L. H. Xie, W. Rutledge, J. R. Li, H. C. Zhou, Zr-based metal-organic frameworks: design, synthesis, structure, and applications. Chem. Soc. Rev. 45 (8) (2016) 2327-67.

[5] S. Yuan, L. Feng, K. Wang, J. Pang, M. Bosch, C. Lollar, Y. Sun, J. Qin, X. Yang, P. Zhang, Q. Wang, L. Zou, Y. Zhang, L. Zhang, Y. Fang, J. Li, H. C. Zhou, Stable Metal-Organic Frameworks: Design, Synthesis, and Applications. Adv. Mater. 30 (37) (2018) e1704303.

[6] H. C. Zhou, J. R. Long, O. M. Yaghi, Introduction to metal-organic frameworks. Chem. Rev. 112 (2) (2012) 673-4.

[7] S. J. Lee, T. U. Yoon, A. R. Kim, S. Y. Kim, K. H. Cho, Y. K. Hwang, J. W. Yeon, Y. S. Bae, Adsorptive separation of xenon/krypton mixtures using a zirconium-based metal-organic framework with high hydrothermal and radioactive stabilities. J. Hazard Mater. 320 (2016) 513-520.

[8] D. Banerjee, C. M. Simon, A. M. Plonka, R. K. Motkuri, J. Liu, X. Chen, B. Smit, J. B. Parise, M. Haranczyk, P. K. Thallapally, Metal-organic framework with optimally selective xenon adsorption and separation. Nat. Commun. 7 (1) (2016) 11831.

[9] H. Xu, C. S. Cao, H. S. Hu, S. B. Wang, J. C. Liu, P. Cheng, N. Kaltsoyannis, J. Li, B. Zhao, High Uptake of $ReO_4^{(-)}$ and CO_2 Conversion by a Radiation-Resistant Thorium-

Nickle [Th$_{48}$Ni$_6$] Nanocage-Based Metal-Organic Framework. Angew. Chem. Int. Ed. 58 (18) (2019) 6022-6027.

[10] S. C. Nandanwar, K. Coldsnow, V. Utgikar, P. Sabharwall, D. E. Aston, Capture of harmful radioactive contaminants from off-gas stream using porous solid sorbents for clean environment-A review. Chem. Eng. J. 306 (2016) 369-381.

[11] J. Liu, P. K. Thallapally, D. Strachan, Metal–Organic Frameworks for Removal of Xe and Kr from Nuclear Fuel Reprocessing Plants. Langmuir 28 (31) (2012) 11584-11589.

[12] Q. Sun, B. Aguila, J. Perman, A. S. Ivanov, V. S. Bryantsev, L. D. Earl, C. W. Abney, L. Wojtas, S. Ma, Bio-inspired nano-traps for uranium extraction from seawater and recovery from nuclear waste. Nat. Commun. 9 (1) (2018) 1644.

[13] L. Chen, Z. Bai, L. Zhu, L. Zhang, Y. Cai, Y. Li, W. Liu, Y. Wang, L. Chen, J. Diwu, J. Wang, Z. Chai, S. Wang, Ultrafast and Efficient Extraction of Uranium from Seawater Using an Amidoxime Appended Metal-Organic Framework. ACS Appl. Mater. Interfaces, 9 (38) (2017) 32446-32451.

[14] Q. Gao, J. Xu, X. H. Bu, Recent advances about metal–organic frameworks in the removal of pollutants from wastewater. Coord. Chem. Rev. 378 (2019) 17-31.

[15] J. Li, X. Wang, G. Zhao, C. Chen, Z. Chai, A. Alsaedi, T. Hayat, X. Wang, Metal-organic framework-based materials: superior adsorbents for the capture of toxic and radioactive metal ions. Chem. Soc. Rev. 47 (7) (2018) 2322-2356.

[16] Y. Peng, H. Huang, D. Liu, C. Zhong, Radioactive Barium Ion Trap Based on Metal-Organic Framework for Efficient and Irreversible Removal of Barium from Nuclear Wastewater. ACS Appl. Mater. Interfaces, 8 (13) (2016) 8527-35.

[17] N. Zhang, L. Y. Yuan, W. L. Guo, S. Z. Luo, Z. F. Chai, W. Q. Shi, Extending the Use of Highly Porous and Functionalized MOFs to Th(IV) Capture. ACS Appl. Mater. Interfaces, 9 (30) (2017) 25216-25224.

[18] Z. Q. Bai, L. Y. Yuan, L. Zhu, Z. R. Liu, S. Q. Chu, L. R. Zheng, J. Zhang, Z. F. Chai, W. Q. Shi, Introduction of amino groups into acid-resistant MOFs for enhanced U(VI) sorption. J. Mater. Chem. A 3 (2) (2015) 525-534.

[19] B. Li, X. Dong, H. Wang, D. Ma, K. Tan, S. Jensen, B. J. Deibert, J. Butler, J. Cure, Z. Shi, T. Thonhauser, Y. J. Chabal, Y. Han, J. Li, Capture of organic iodides from nuclear waste by metal-organic framework-based molecular traps. Nat. Commun. 8 (1) (2017) 485.

[20] M. Zha, J. Liu, Y. L. Wong, Z. Xu, Extraction of palladium from nuclear waste-like acidic solutions by a metal–organic framework with sulfur and alkene functions. J. Mater. Chem. A 3 (7) (2015) 3928-3934.

[21] S. K. Elsaidi, M. H. Mohamed, A. S. Helal, M. Galanek, T. Pham, S. Suepaul, B. Space, D. Hopkinson, P. K. Thallapally, J. Li, Radiation-resistant metal-organic framework enables efficient separation of krypton fission gas from spent nuclear fuel. Nat. Commun. 11 (1) (2020) 3103.

[22] C. Volkringer, C. Falaise, P. Devaux, R. Giovine, V. Stevenson, F. Pourpoint, O. Lafon, M. Osmond, C. Jeanjacques, B. Marcillaud, J. C. Sabroux, T. Loiseau, Stability of metal-organic frameworks under gamma irradiation. Chem. Commun. 52 (84) (2016) 12502-12505.

[23] E. A. Gendy, D. T. Oyekunle, J. Ali, J. Ifthikar, A. M. Ramadan, Z. Chen, High-performance removal of radionuclides by porous organic frameworks from the aquatic environment: A review. J. Environ. Radioact. 238 (2021) 106710.

[24] K. Vellingiri, K. H. Kim, A. Pournara, A. Deep, Towards high-efficiency sorptive capture of radionuclides in solution and gas. Prog. Mater. Sci. **2018**, 94 (2018) 1-67.

[25] C. Ma, A. Vasileiadis, H. T. Wolterbeek, A. G. Denkova, P. Serra Crespo, Adsorption of molybdenum on Zr-based MOFs for potential application in the ^{99}Mo/^{99m}Tc generator. Appl. Surf. Sci. 572 (2022) 151340.

[26] S. E. Gilson, M. Fairley, P. Julien, A. G. Oliver, S. L. Hanna, G. Arntz, O. K. Farha, J. A. LaVerne, P. C. Burns, Unprecedented Radiation Resistant Thorium-Binaphthol Metal-Organic Framework. J. Am. Chem. Soc. 142 (31) (2020) 13299-13304.

[27] S. L. Hanna, D. X. Rademacher, D. J. Hanson, T. Islamoglu, A. K. Olszewski, T. M. Nenoff, O. K. Farha, Structural Features of Zirconium-Based Metal–Organic Frameworks Affecting Radiolytic Stability. Ind. Eng. Chem. Res. 59 (16) (2020) 7520-7526.

[28] B. Aguila, D. Banerjee, Z. Nie, Y. Shin, S. Ma, P. K. Thallapally, Selective removal of cesium and strontium using porous frameworks from high level nuclear waste. Chem. Commun. 52 (35) (2016) 5940-2.

[29] K. Vimalnath, A. Rajeswari, S. Chakraborty, A. Dash, Large scale production of ^{51}Cr for medical application in a medium flux research reactor: A comparative investigation of Szilard–Chalmers process and direct (n, γ) route. Appl. Radiat. Isot. 91 (2014) 104-108.

[30] Y. Mao, H. Qi, G. Ye, L. Han, W. Zhou, W. Xu, Y. Y. Sun, Green and time-saving synthesis of MIL-100(Cr) and its catalytic performance. Microporous Mesoporous Mater. 274 (2019) 70-75.

[31] Y. K. Seo, J. W. Yoon, J. S. Lee, U. H. Lee, Y. K. Hwang, C. H. Jun, P. Horcajada, C. Serre, J. S. Chang, Large scale fluorine-free synthesis of hierarchically porous iron(III) trimesate MIL-100(Fe) with a zeolite MTN topology. Microporous Mesoporous Mater. 157 (2012) 137-145.

[32] T. Zhao, F. Jeremias, I. Boldog, B. Nguyen, S. K. Henninger, C. Janiak, High-yield, fluoride-free and large-scale synthesis of MIL-101(Cr). Dalton Trans. 44 (38) (2015) 16791-16801.

[33] Y. Wang, Q. T. Qu, G. Liu, V. S. Battaglia, H. H. Zheng, Aluminum fumarate-based metal organic frameworks with tremella-like structure as ultrafast and stable anode for lithium-ion batteries. Nano Energy, 39 (2017) 200-210.

[34] S. Li, J. Cui, X. Wu, X. Zhang, Q. Hu, X. Hou, Rapid in situ microwave synthesis of Fe_3O_4@MIL-100(Fe) for aqueous diclofenac sodium removal through integrated adsorption and photodegradation. J Hazard Mater. 373 (2019) 408-416.

[35] P. Horcajada, C. Serre, M. Vallet-Regí, M. Sebban, F. Taulelle, G. J. Férey, Metal-organic frameworks as efficient materials for drug delivery. 118 (36) (2006) 6120-6124.

[36] S. Karmakar, J. Dechnik, C. Janiak, S. De, Aluminium fumarate metal-organic framework: A super adsorbent for fluoride from water. J Hazard Mater. 303 (2016) 10-20.

[37] R. Azhdari, S. M. Mousavi, S. A. Hashemi, S. Bahrani, S. Ramakrishna, Decorated graphene with aluminum fumarate metal organic framework as a superior non-toxic agent for efficient removal of Congo Red dye from wastewater. J. Environ. Chem. Eng. 7 (6) (2019) 103437.

[38] S. R. Cherry, J. A. Sorenson, M. E. Phelps, Physics in nuclear medicine e-Book. Elsevier Health Sciences: 2012, chapter 6, pp 74-84.

[39] S. B. Dhiman, G. S. Goff, W. Runde, J. A. LaVerne, Gamma and heavy ion radiolysis of ionic liquids: A comparative study. J. Nucl. Mater. 453 (1-3) (2014) 182-187.

[40] C. Wang, O. Volotskova, K. Lu, M. Ahmad, C. Sun, L. Xing, W. Lin, Synergistic assembly of heavy metal clusters and luminescent organic bridging ligands in metal-organic frameworks for highly efficient X-ray scintillation. J. Am. Chem. Soc.136 (17) (2014) 6171-6174.

[41] S. Dissegna, K. Epp, W. R. Heinz, G. Kieslich, R. A. Fischer, Defective Metal-Organic Frameworks. Adv. Mater. 30 (37) (2018) e1704501.

[42] D. Wang, Y. Ke, D. Guo, H. Guo, J. Chen, W. Weng, Facile fabrication of cauliflower-like MIL-100 (Cr) and its simultaneous determination of Cd^{2+}, Pb^{2+}, Cu^{2+} and Hg^{2+} from aqueous solution. Sens. Actuators B: Chem. 216 (2015) 504-510.

[43] X. Ma, W. Wang, C. Sun, H. Li, J. Sun, X. Liu, Adsorption performance and kinetic study of hierarchical porous Fe-based MOFs for toluene removal. Sci. Total Environ. 793 (2021) 148622.

[44] B. Han, Z. Duan, J. Xu, Y. Zhu, Q. Xu, H. Wang, H. Tai, J. Weng, Y. Zhao, The art of integrated functionalization: super stable black phosphorus achieved through metal-organic framework coating. Adv. Funct. Mater. 30(27) (2020) 2002232.

[45] Z. Li, X. Liu, W. Jin, Q. Hu, Y. Zhao, Adsorption behavior of arsenicals on MIL-101 (Fe): the role of arsenic chemical structures. J. Colloid Interface sci. 554 (2019) 692-704.

Supporting Information

S 1. Synthesis

1.1 Material

1,3,5-benzenetricarboxylic acid (H$_3$BTC, 95%), 1,4-benzene dicarboxylic acid (H$_2$BDC, 98%) and sodium hydroxide (NaOH, $\geq$ 98%) were purchased from Sigma-Aldrich. Chromium chloride hexahydrate (CrCl$_3$·6H$_2$O, $\geq$ 96%), chromium nitrate nonahydrate (Cr(NO$_3$)$_3$·9H$_2$O, $\geq$ 98%), fumaric acid (>98%) and aluminum sulfate octahydrate (Al$_2$(SO$_4$)$_3$·18H$_2$O, 98%) were provided by Merck. Ferric nitrate nonahydrate (Fe(NO$_3$)$_3$·9H$_2$O, $\geq$99%) was provided by Fluka. All chemical reagents were used without any purification.

1.2 Synthesis of MIL-100 (Cr)

1.05 g of CrCl$_3$·6H$_2$O and 0.42 g H$_3$BTC were mixed in a mortar and grounded using hand for 1 h at room temperature. Then the powder was transferred to a Teflon lined-autoclave and heated at 220 °C for 15 h in an electric oven. The obtained powder was washed with deionized water at 70 °C and ethanol at 60 °C for 3 h, respectively. The final collected product was dried at 150 °C for 12 h under vacuum.

1.3 Synthesis of MIL-101 (Cr)

Typically, 1.6 g of Cr(NO$_3$)$_3$·9H$_2$O and 664 mg of H$_2$BDC were added into 19.2 ml of deionized water. Then 0.177 ml of HNO$_3$ was added to the mixture, which was further sonicated to obtain a homogeneous solution. Finally, the solution was transferred to a Teflon lined-autoclave and heated at 220 °C for 8 h. To remove the unreacted reagents, the obtained precipitation was washed with DMF at 65 °C for 2 h and EtOH at 80 °C for 24 h. Then the powder was washed with hot water at 80 °C for 5 h and finally dried at 120 °C overnight.

1.4 Synthesis of MIL-100 (Fe)

3.03 g of Fe(NO$_3$)$_3$·9H$_2$O and 1050.7 mg of H$_3$BTC were mixed and grounded by hand for half an hour. The mixture was transferred to a Teflon lined-autoclave and heated at 160 °C for 4 h. The collected product was washed with deionized water and ethanol for three times, respectively. The final sample was dried at 150 °C for 12 h under vacuum.

1.5 Synthesis of AlFu MOF

Aluminum fumarate MOF was synthesized using the hydrothermal method. 14.728 g of $Al_2(SO_4)_3 \cdot 18H_2O$ was dissolved in 70 ml of deionized water and the solution was heated at 60 °C for one hour. Another solution containing NaOH (5.32 g) and fumaric acid (5.104 g) was added to 70 ml of water and heated under 60 °C for one hour, which was then pumped into the above solution within 15 min. The suspension was kept at 60 °C for 30 min. the final product was washed with deionized water and ethanol three times, respectively. The sample was dried at 80 °C for 12 h.

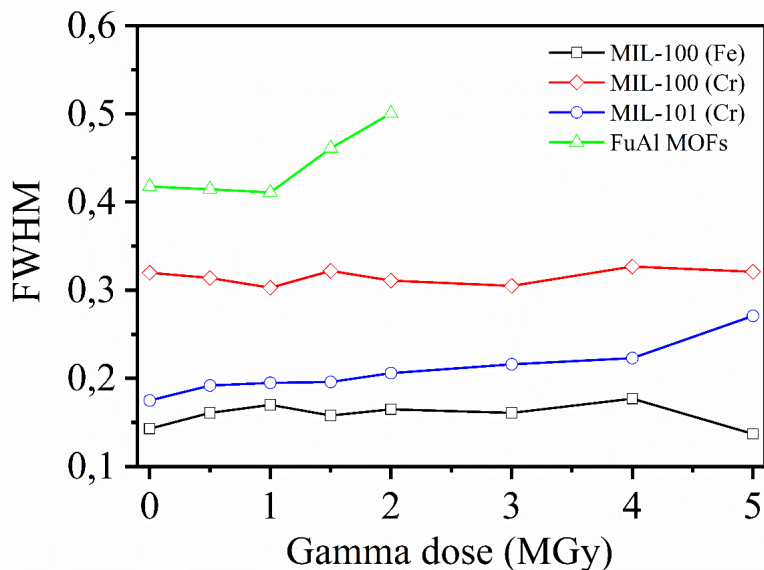**Figure S5.1.** The facility of Cobalt-60 sources.

Figure S5.2. Fluctuations of full width at half maxima (FWHM) for all MOFs under different gamma doses.

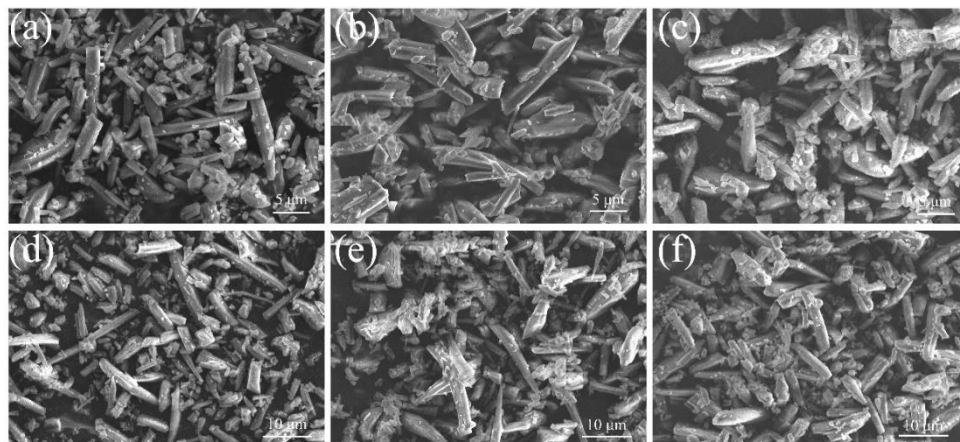**Figure S5.3.** SEM images of MIL-100 (Fe) under different gamma doses: (a) 0 Gy, (b) 1.0 MGy, (c) 2.0 MGy, (d) 3.0 MGy, (e) 4.0 MGy and (f) 5.0MGy.
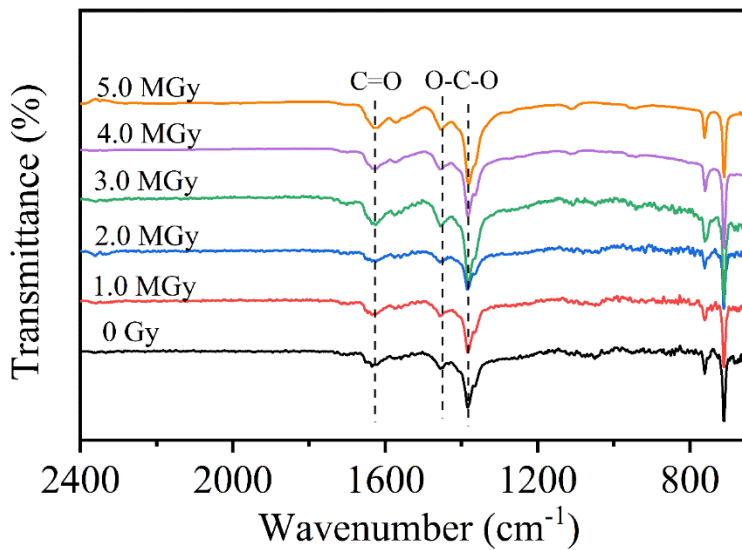
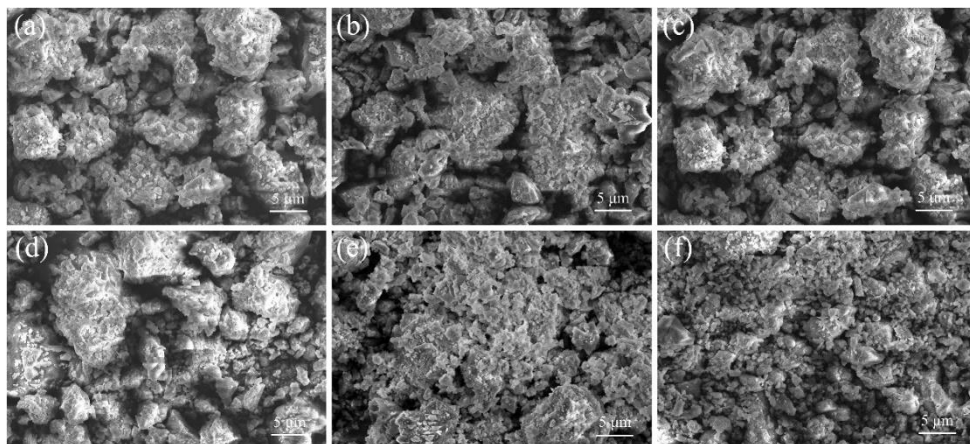**Figure S5.4.** FT-IR spectra of MIL-100 (Fe) under different gamma doses.

Figure S5.5. SEM images of MIL-100 (Cr) under different gamma doses: (a) 0 Gy, (b) 1.0 MGy, (c) 2.0 MGy, (d) 3.0 MGy, (e) 4.0 MGy and (f) 5.0MGy.

Figure S5.6. FT-IR spectra of MIL-100 (Cr) under different gamma doses.

Figure S5.7. SEM images of MIL-101 (Cr) under different gamma doses: (a) 0 Gy, (b) 1.0 MGy, (c) 2.0 MGy, (d) 3.0 MGy, (e) 4.0 MGy and (f) 5.0MGy.
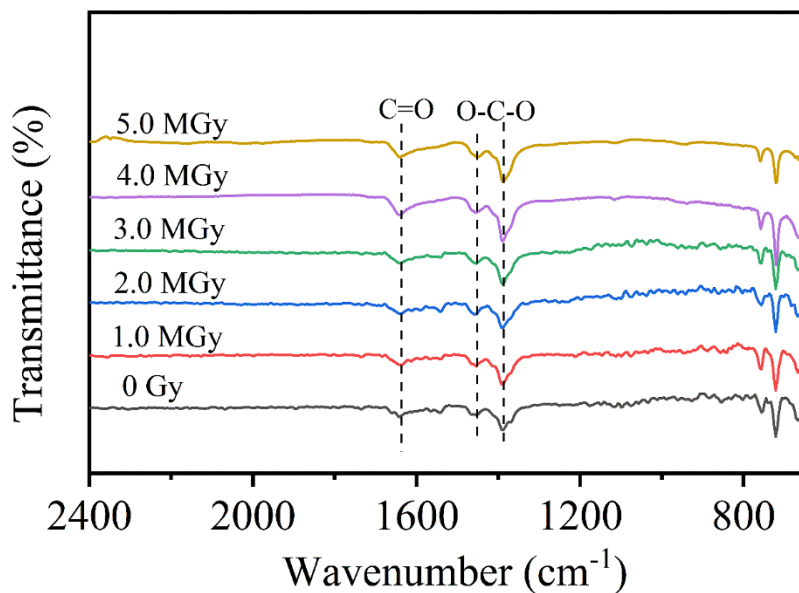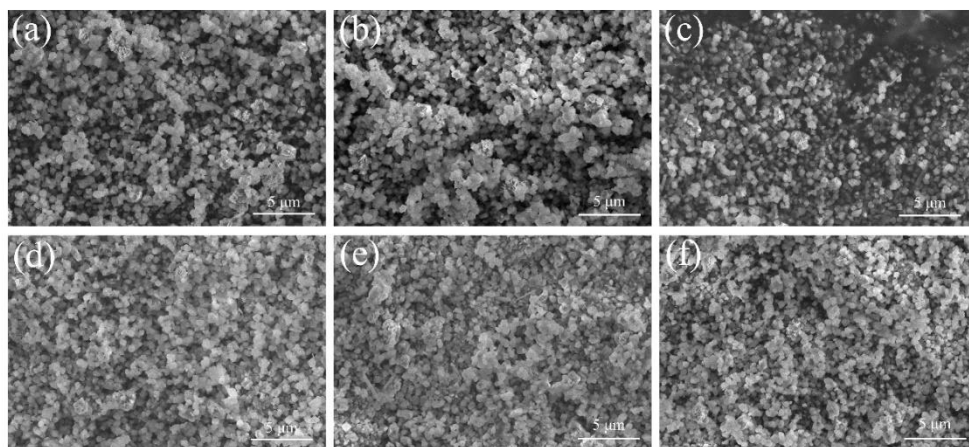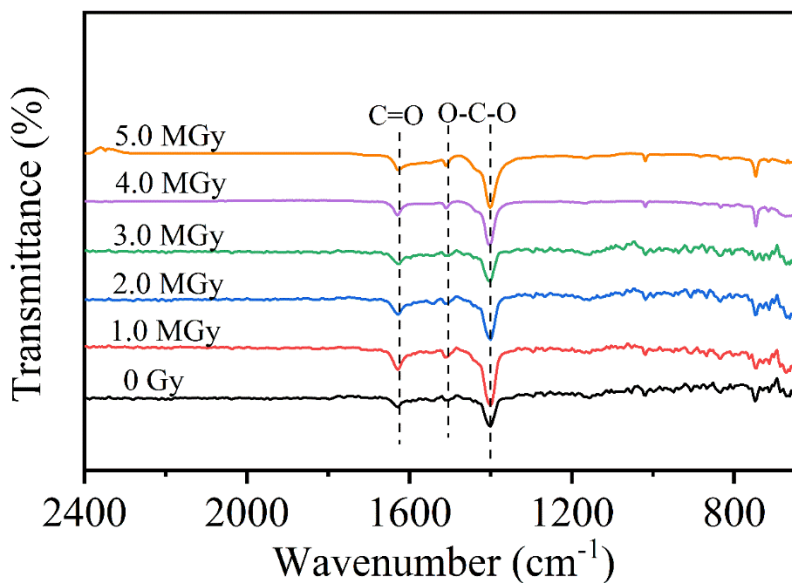
Figure S5.8. FT-IR spectra of MIL-101 (Cr) under different gamma doses.
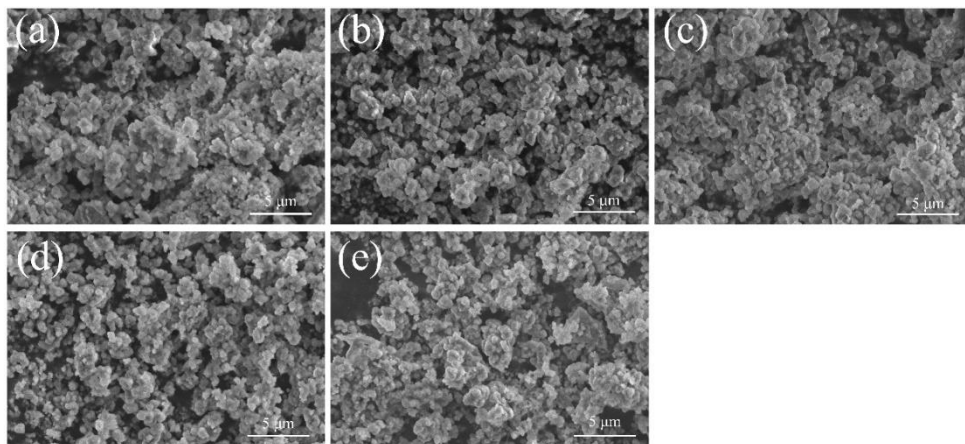

Figure S5.9. SEM images of AlFu MOFs under different gamma doses: (a) 0 Gy, (b) 0.5 MGy, (c) 1.0 MGy, (d) 1.5 MGy and (e) 2 MGy.
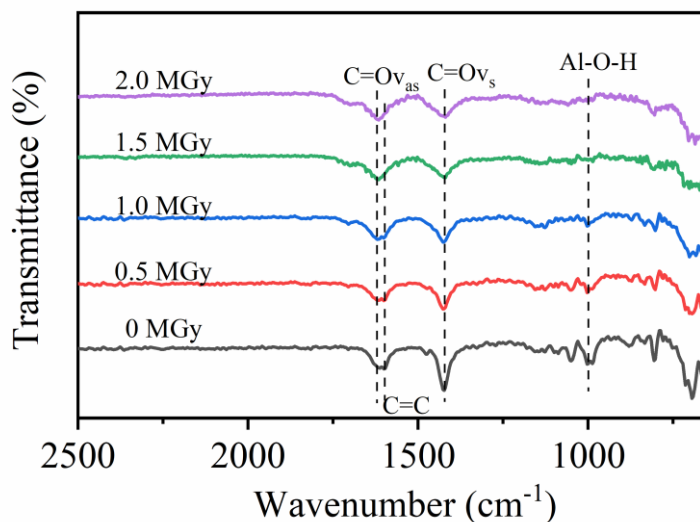
Figure S5.10. FT-IR spectra of AlFu MOFs under different gamma doses.
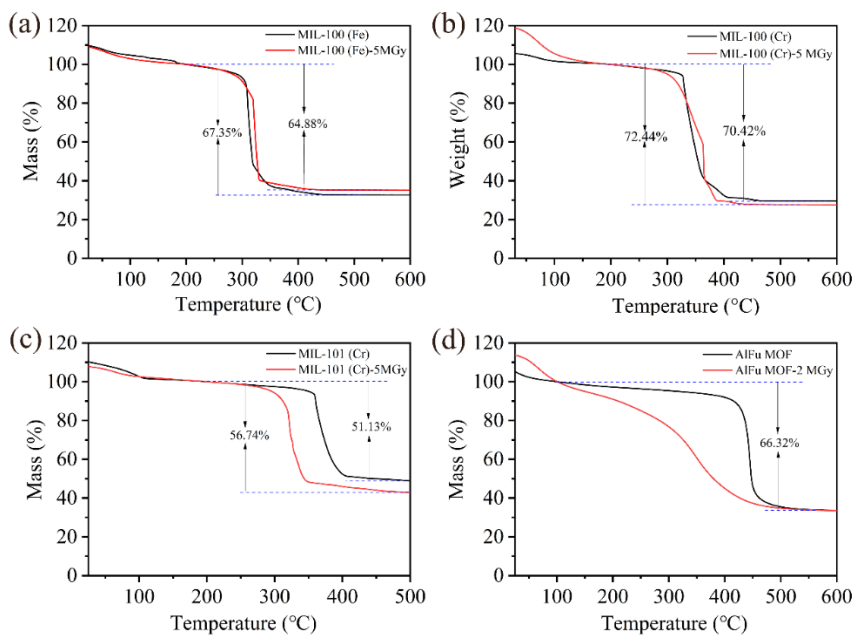

Figure S5.11. The TGA curves of (a) MIL-100 (Fe), (b) MIL-100 (Cr), (c) MIL-101 (Cr) and (d) AlFu MOFs before and after gamma radiation (5 MGy)

Production of high specific activity ^{51}Cr using MIL-100 (Cr) and MIL-101 (Cr) and the Szilard-Chalmers effect

6

Abstract

Chromium-51 (^{51}Cr) is an attractive radionuclide that is applied for red cells and platelet radiolabelling. However, commercially available ^{51}Cr produced in nuclear reactors via neutron activation requires long irradiation times and a complex separation method. In this work, two chromium-based metal-organic frameworks (MIL-100 (Cr) and MIL-101 (Cr)) were synthesized for the production of ^{51}Cr. The chromium-based MOFs were neutron activated according to the (n, γ) reaction and the produced ^{51}Cr was separated by solid-liquid extraction based on the Szilard-Chalmers effect. HCl and H_2SO_4 were applied to extract the produced ^{51}Cr from irradiated MIL-100 (Cr) and MIL-101 (Cr), as well as aqueous solutions containing different concentrations of the chelator ethylenediaminetetraacetic acid (EDTA). The influence of extraction time and pH on the ^{51}Cr separation was studied. The results showed that enrichment factor between 400 and 700 could be obtained when HCl and H_2SO_4 were used as extraction agents. The most promising results were achieved when using irradiated MIL-101 (Cr) and EDTA as extractant reaching an enrichment factor of 1132±50.

6.1 Introduction

A wide variety of radionuclides are applied for diagnostic and therapeutic procedures in nuclear medicine. Chromium-51 (^{51}Cr) is one attractive radionuclide because of its low photon yield (10%). ^{51}Cr decays through a branched decay, i.e., 90% of ^{51}Cr decays directly to the ground state of Vanadium-51 via electron capture, while 10% of ^{51}Cr decays to the excited state of ^{51}V via electron capture and further to the ground state by emitting gamma-ray with an energy of 320 keV. ^{51}Cr is widely used to radiolabel red blood cells and platelets allowing to assess their life span or to determine the blood volume of patients as well as to diagnose gastrointestinal bleeding [1].

^{51}Cr can be produced by neutron activation in nuclear reactors based on the ^{50}Cr(n, γ)^{51}Cr reaction. The specific activity of ^{51}Cr needed for clinical application must be at least 1.85 TBq/g. In order to produce ^{51}Cr with such high specific activity, expensive enriched ^{50}Cr target, high neutron flux and long irradiation are needed. These conditions restrict the production of high specific activity ^{51}Cr to a few research reactors. An alternative method to produce ^{51}Cr with high specific activity is using the Szilard-Chalmers effect. The Szilard Chalmers method is based on the principle that upon the emission of high energy prompt gammas when neutron activated, the resulting atom can receive sufficiently high energy to break the chemical bonds in the target material so that it can be released from its initial chemical structure [2]. Provided that the produced radionuclide can be separated from its original chemical structure, radionuclides with high specific activity can be produced via this method.

In the past few decades, ^{51}Cr produced via the Szilard-Chalmers method was mainly obtained based on the irradiation of K_2CrO_4 targets [3-5]. For example, Bag. et al. [6] studied how ^{51}Cr could be separated using alumina carrier based on a coprecipitation method at different temperatures, showing that a ~72% elution efficiency with an enrichment factor of 180 could be achieved. Vimalnath et al [5]. also utilized the same precipitation method to separate the produced ^{51}Cr, obtaining high specific activity of ^{51}Cr (5.5 GBq/mg). However, the precipitation separation process requires extra experimental steps, which are time-consuming and can lead to the introduction of impurities. In this work, we propose a novel material using metal-organic frameworks (MOFs), which can facilitate a very simple separation method without compromising the quality of the obtained product.

MOFs are attractive materials due to their diverse topologies, high porosity and surface area, finding various applications [7], including drug delivery [8, 9], separation of radionuclides [10, 11] and radioactive gas storage [12, 13]. However, so far, no reports can be found in the application of MOFs as target materials for the production of radionuclides. MIL-100 (Cr) and MIL-101 (Cr) (MIL is a material of Institute Lavoisier) are trivalent metal carboxylate systems, which have high surface area and large pores [14]. They also have excellent thermal, chemical, mechanical and radiation stability [15, 16]. Therefore, in this study, they were selected as the target materials to produce ^{51}Cr with high specific activity utilizing the Szilard Chalmers effect. Different conditions were investigated including extraction time, different extractants and pH values.

6.2 Experimental

6.2.1 Materials

Sulfuric acid (H_2SO_4, 95~97%), Ethylenediaminetetraacetic acid disodium salt dihydrate (EDTA-Na$_2$, >99%), 1,3,5-benzenetricarboxylic acid (H_3BTC, 95%) and 1,4-benzene dicarboxylic acid (H_2BDC, 98%) were purchased from Sigma-Aldrich. Hydrochloric acid (HCl, 30%), Chromium chloride hexahydrate (CrCl$_3$·6H$_2$O, ≥96%) and chromium nitrate nonahydrate (Cr(NO$_3$)$_3$·9H$_2$O, ≥98%) were provided by Merck. All chemical reagents were used without any purification.

6.2.2 Synthesis of MIL-100 (Cr) and MIL-101 (Cr)

The MIL-100 (Cr) was prepared based on the work from Mao et al. [17] Briefly, CrCl$_3$·6H$_2$O (1.05 g) and H$_3$BTC (0.42 g) were well mixed in a mortar and pestled for 1 h at room temperature. The homogeneous powder was then moved to a Teflon-lined autoclaved and heated at 220 °C for 15 h. The final solid was washed three times using deionized water and ethanol and dried at 150 °C for 12 h in vacuum.

MIL-101 (Cr) was prepared by the hydrothermal method as reported by Seo et al. [18] Cr(NO$_3$)$_3$·9H$_2$O (1.6 g), H$_2$BDC (664 mg) and HNO$_3$ (0.177 mL) were dissolved in 19.2 ml of deionized water. The solution was then transferred to a Teflon-lined autoclave and heated at 220 °C for 8 h. The resulting precipitates were washed three times with both DFM and ethanol. Finally, the obtained powder was dried at overnight 120 °C.

6.2.3   Characterization

The X-ray diffraction patterns (XRD) of the samples were collected by a PANalytical X'Pert Pro pw3040/60 diffractometer using Cu Kα radiation (λ=1.541 Å). The thermalgravimetric analysis (TGA) of the two MOFs was determined by a Mettler-Toledo/STDA 851e apparatus under air environment at a heating rate of 5°C/min. The activity of all chromium solutions (320 keV for ^{51}Cr) was measured using a Wallac gamma counter (Wizard 2480, PerkinElmer). The total chromium content was measured by inductively coupled plasma optical emission spectroscopy (ICP-OES, Optima 4300, Perkin Elmer).

6.2.4   Neutron irradiation

The synthesized MIL-100 (Cr) and MIL-101 (Cr) were irradiated for 10 h at the Hoger Onderwijs Reactor (HOR) of the Reactor Institute Delft, the Netherlands. The thermal neutron flux and epithermal neutron flux of the irradiation facility used were 3.11×10^{16} n/(s·m^2) and 7.2×10^{14} n/(s·m^2), respectively. 5±0.1 mg of MOFs was sealed in Posthumus PE (polyethylene) capsules and then packaged in Posthumus Plastic PE rabbits for irradiation. All experiments were conducted in triplicate.

6.2.5 ^{51}Cr extraction with EDTA

The irradiated sample was put into a glass tube containing 10 mL of EDTA (1 mM, pH 5). The mixture was shaken for various time intervals (1 h, 3 h, 6 h, 24 h) at room temperature and then 5 ml of the solution was transferred to a centrifuge tube and centrifuged for 10 min at 4000 rpm. Finally, 3 ml of the supernatant was taken and the counts of ^{51}Cr originating from the 321 keV were measured by gamma spectrometry (Wallac Wizard).

10 ml of EDTA solution having different concentrations (1mM, 100 mM and 250 mM, pH 5) and different pH values (1, 5 and 8) were used to extract ^{51}Cr at room temperature. After shaking for 1 h, 5 ml of the mixture was put in a centrifuge tube followed by 10 min centrifugation at 4000 rpm. Finally, 3 ml of the supernatant was transferred to a glass bottle and the count of ^{51}Cr originating from the 321 keV was measured by gamma spectrometry (Wallac Wizard).

6.2.6 ^{51}Cr extraction with HCl and H_2SO_4

HCl (30%) and H_2SO_4 (15%) were used for ^{51}Cr extraction from irradiated MIL-100 (Cr) and MIL-101 (Cr). The irradiated samples were dispersed in a glass tube containing 10 ml of one of the acids. 5 ml of solution was added to a plastic centrifuge tube and shaken for 1 h and centrifuged for 10 min at 4000 rpm. Finally, 3 ml of the supernatant was transferred to a glass bottle and the counts of ^{51}Cr originating from the 321 keV gamma emission were measured by gamma spectrometry (Wallac Wizard).

6.2.7   Calculation of extraction efficiency and enrichment factor

The enrichment factor (EF) can be calculated by the following equation:

$$EF=\eta*m_o/m_s$$

Where m_o is the chromium mass of the irradiated sample and m_s is the chromium mass left in the supernatant after extraction. η is the extraction efficiency and it can be determined by the following equation:

$$\eta=A_1/A_0$$

Where A_0 is the activity of the irradiated sample and A_1 is the activity of the extracted sample. The specific activity (SA) of extracted ^{51}Cr can be estimated using the formula:

$$SA=A/m$$

A is the activity of extracted ^{51}Cr and m is the mass of Cr in solution.

6.3 Results and discussion

6.3.1   Characterization of MOFs

The synthesized MIL-100 (Cr) and MIL-101 (Cr) were characterized by XRD, as shown in Fig. 6.1 (a). It can be observed that the diffraction peak positions of the synthesized MIL-100 (Cr) and MIL-101 (Cr) were consistent with the simulated XRD patterns, indicating successful synthesis. Fig. 6.1 (b) shows the TGA curves of MIL-100 (Cr) and MIL-101 (Cr). The weight loss of adsorbed water moisture appeared from 25 °C to 100 °C. Then, the weight loss of two MOFs did not show a significant decrease from 100 °C to 300 °C, showing good stability. After 300 °C, the MOFs decomposed quickly, which is due to the combustion of the organic linkers, resulting in weight loss of 72.9% and 59.25% for MIL-100 (Cr) and MIL-101 (Cr), respectively.
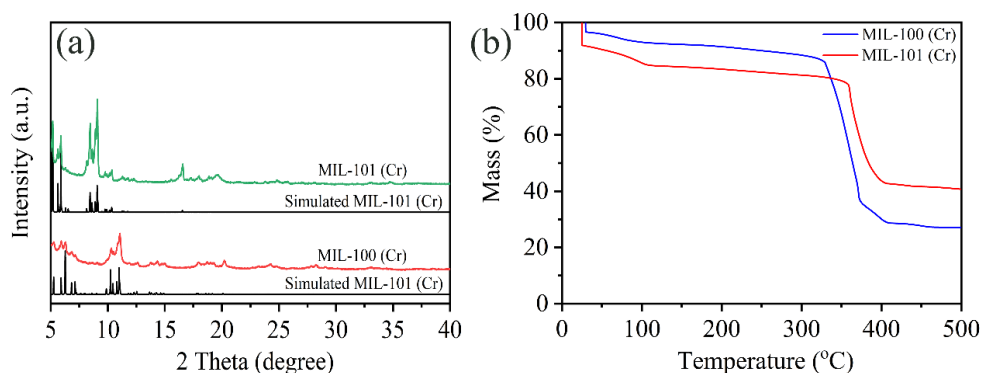
Fig. 6.1. (a) XRD patterns and their simulated patterns and (b) TGA curves of the synthesized MIL-100 (Cr) and MIL-101 (Cr) before irradiation

6.3.2 ⁵¹Cr extraction from irradiated MIL-100 (Cr)

EDTA optimized extraction of MIL-100 (Cr)

To find the optimized extraction conditions of ⁵¹Cr for MIL-100 (Cr) using EDTA, the extraction based on the Szilard-Chalmers effect was performed at different extraction times, EDTA concentration and pH of the solution. The effect of extraction time on the separation efficiency of ⁵¹Cr is shown in Fig. 6.2 (a). The extraction efficiency of ⁵¹Cr increased from $22\pm0.02\%$ to $33\pm0.02\%$ by increasing the extraction time from 1 h to 24 h. However, the enrichment factor (Fig. 6.2 (b)) and SA of ⁵¹Cr (Fig. 6.2 (c)) decreased with increasing extraction time. The optimum extraction time appears to be one hour, which resulted in an enrichment factor of 321. The influence of EDTA concentrations on extraction efficiency was also evaluated, as shown in Fig. 6.2 (d). When the EDTA concentration increased from 1 mM to 100 mM, the extraction efficiency of ⁵¹Cr doubled from $22\pm0.02\%$ to $46\pm0.05\%$. Further increasing the EDTA concentration to 250 mM did not lead to improvement of the yield ($45\pm0.04\%$). The corresponding enrichment factor of ⁵¹Cr was found to be the highest at 1 mM EDTA. As EF is another important factor, 1 mM was determined to be the optimum EDTA concentration although the extraction efficiency was just $22\pm0.02\%$. Furthermore, the influence of pH on the separation yield and enrichment factor was investigated, as shown in Fig. 6.2 (g). The extraction efficiency of ⁵¹Cr decreased from $38\pm0.08\%$ to $21\pm0.02\%$ with the increasing pH value from 1 to 8. The enrichment factor of ⁵¹Cr was also found to be the highest at the lower pH value, reaching an enrichment factor of 564 ± 140. Based on the

analysis mentioned above, the optimized extraction condition is using EDTA with a concentration of 1 mM at pH 1 and extraction time of 1 h.
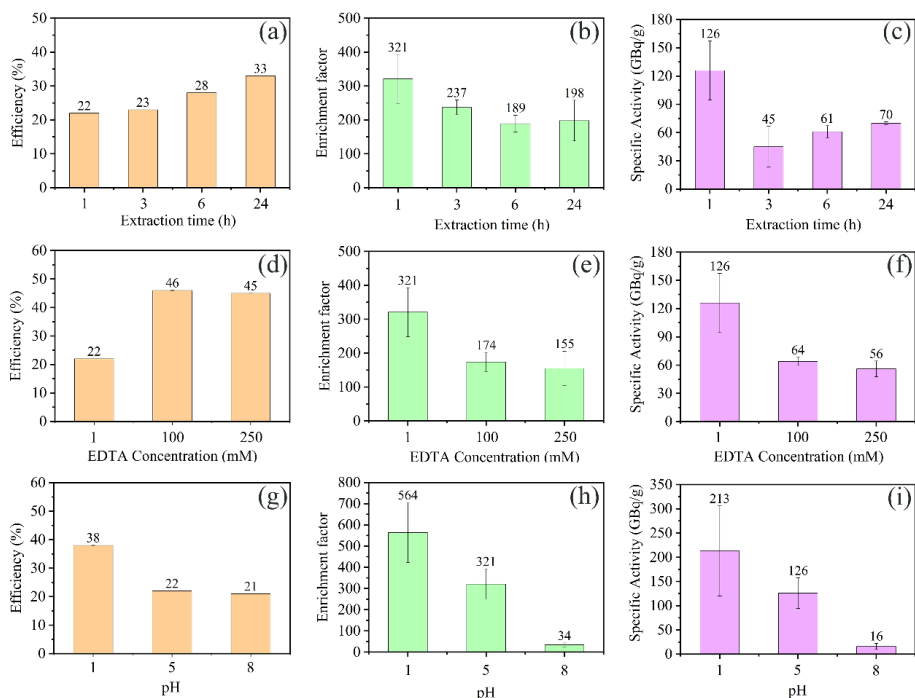

Fig. 6.2. Extraction efficiency (a), enrichment factor (b) and specific activity (c) of ^{51}Cr for MIL-100 (Cr) using EDTA (1 mM, pH=5) as function of extraction time; Extraction efficiency (d), enrichment factor (e) and specific activity (f) of ^{51}Cr for MIL-100 (Cr) using EDTA (extraction time 1 h, pH=5) as function of the EDTA concentration; Extraction efficiency (g), enrichment factor (h) and specific activity (i) of ^{51}Cr for MIL-100 (Cr) using EDTA (1 mM, extraction time 1 h) as function of the pH.

Acid extraction applied to MIL-100 (Cr)

The influence of using two acids as extractants as well as the extraction time was evaluated for the irradiated MIL-100 (Cr). Fig. 6.3 (a) shows that $82\pm0.02\%$ of ^{51}Cr could be extracted using HCl versus $57\pm0.2\%$ when applying H_2SO_4 at a fixed extraction time of 1 h. The corresponding enrichment factor were 458 ± 30 and 428 ± 195, respectively. Extending the extraction time to 24 hours, the extraction efficiency decreased to $54\pm0.01\%$ and $51\pm0.02\%$ for HCl and H_2SO_4 respectively. The EF for HCl was also found to decrease from 458 ± 30 to 207 ± 9 after 24 hours of extraction. Using speciation calculation, it appears that $CrCl^{2+}$ and

$Cr(SO_4)^+$ are the main chromium species under these conditions. HCl is volatile which can lead to loss after long extraction time, which will influence the formation of chromium species resulting in a significant reduction of separation efficiency and enrichment factor.
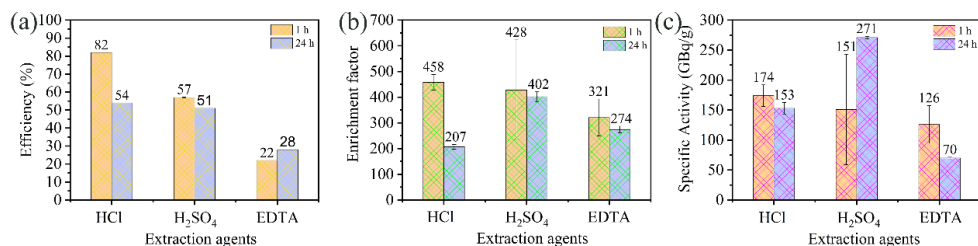

Fig. 6.3. (a) Efficiency, (b) enrichment factor and (c) specific activity of ^{51}Cr extracted with different chemical reagents at different times from irradiated MIL-100 (Cr).

6.3.3 ^{51}Cr extraction from irradiated MIL-101 (Cr)

Fig. 6.4 (a) displays the extraction efficiency of MIL-101 (Cr) using three different chemical reagents at 1 h. It can be observed that $57\pm0.05\%$ of ^{51}Cr can be extracted using HCl and H_2SO_4, while a relatively higher enrichment factor of 670 ± 121 can be achieved using H_2SO_4 compared with that of HCl (552 ± 116). When EDTA was applied for ^{51}Cr extraction, a much higher enrichment factor (1132 ± 50) could be obtained although it has a lower separation efficiency ($22\pm0.04\%$). This high enrichment factor is similar to the one previously reported that has an enrichment factor of 1150 [3], but this separation method is simpler and faster. Considering the practical application of ^{51}Cr in nuclear medicine, higher specific activity of ^{51}Cr needs to be produced. So, the MOFs will be irradiated for a longer time to produce ^{51}Cr with higher specific activity in the following process.
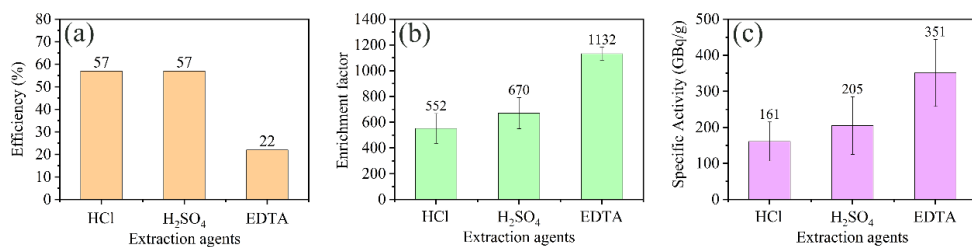

Fig. 6.4. (a) Efficiency, (b) enrichment factor and (c) specific activity of ^{51}Cr extracted with different chemical reagents for 1 h from irradiated MIL-101 (Cr).

6.4 Conclusion

MIL-100 (Cr) and MIL-101 (Cr) were synthesized and applied to produce ^{51}Cr using the Szilard-Chalmers method. Different conditions were explored to separate the produced ^{51}Cr using EDTA, HCl and H_2SO_4. For irradiated MIL-100 (Cr), the optimum conditions appear to be using 1 mM EDTA at pH 1 after extraction time of 1 h. When HCl and H_2SO_4 were applied to separate ^{51}Cr, high extraction efficiency (>50%) and enrichment factor (200~500) could be obtained. For irradiated MIL-101 (Cr), high extraction efficiency (>50%) and enrichment factor (500~700) could be obtained when HCl and H_2SO_4 were used to separate [51]Cr. Although ^{51}Cr separation had relatively lower separation efficiency (~22%) using EDTA, a high enrichment factor (~1132±50) and specific activity (~351 GBq/g) were achieved.

References

[1] P.L. Mollison, N. Veall, The use of the isotope ^{51}Cr as a label for red cells, Br J Haematol. 1 (1955) 62-74.

[2] B.S. Tomar, O.M. Steinebach, B.E. Terpstra, P. Bode, H.T. Wolterbeek, Studies on production of high specific activity [99]Mo and ^{90}Y by Szilard Chalmers reaction, Radiochimica. Acta, 98 (2010) 499-506.

[3] N. Shibata, K.J. Yoshihara, Preparation of Chromium-51 of a High Specific Activity by the Szilard-Chalmers Process, 32 (1959) 422-423.

[4] G. Harbottle, A.G. Maddock, The Preparation of Chromium-51 of High Specific Activity, 21 (1953) 1686-1687.

[5] K.V. Vimalnath, A. Rajeswari, S. Chakraborty, A. Dash, Large scale production of ^{51}Cr for medical application in a medium flux research reactor: a comparative investigation of Szilard-Chalmers process and direct (n, γ) route, Appl. Radiat. Isot. 91 (2014) 104-108.

[6] D. Brune, Separation of ^{51}Cr by Means of the Szilard-Chalmers Effect from Potassium Chromate Irradiated at Low Temperature, in, Sweden, 1967, pp. 20.

[7] Z.J. Lin, J. Lu, M. Hong, R. Cao, Metal-organic frameworks based on flexible ligands (FL-MOFs): structures and applications, Chem. Soc. Rev. 43 (2014) 5867-5895.

[8] I. Abánades Lázaro, R.S. Forgan, Application of zirconium MOFs in drug delivery and biomedicine, Coord. Chem. Rev. 380 (2019) 230-259.

[9] M.X. Wu, Y.W. Yang, Metal-Organic Framework (MOF)-Based Drug/Cargo Delivery and Cancer Therapy, Adv. Mater. 29 (2017) 1606134.

[10] J. Li, X. Wang, G. Zhao, C. Chen, Z. Chai, A. Alsaedi, T. Hayat, X. Wang, Metal-organic framework-based materials: superior adsorbents for the capture of toxic and radioactive metal ions, Chem. Soc. Rev. 47 (2018) 2322-2356.

[11] N. Shen, Z. Yang, S. Liu, X. Dai, C. Xiao, K. Taylor-Pashow, D. Li, C. Yang, J. Li, Y. Zhang, M. Zhang, R. Zhou, Z. Chai, S. Wang, $^{99}TcO_4^-$ removal from legacy defence nuclear waste by an alkaline-stable 2D cationic metal organic framework, Nat. Commun. 11 (2020) 5571.

[12] S.K. Elsaidi, M.H. Mohamed, A.S. Helal, M. Galanek, T. Pham, S. Suepaul, B. Space, D. Hopkinson, P.K. Thallapally, J. Li, Radiation-resistant metal-organic framework enables efficient separation of krypton fission gas from spent nuclear fuel, Nat. Commun. 11 (2020) 3103.

[13] S.J. Lee, T.U. Yoon, A.R. Kim, S.Y. Kim, K.H. Cho, Y.K. Hwang, J.W. Yeon, Y.S. Bae, Adsorptive separation of xenon/krypton mixtures using a zirconium-based metal-organic framework with high hydrothermal and radioactive stabilities, J. Hazard Mater. 320 (2016) 513-520.

[14] G. Ferey, C. Mellot-Draznieks, C. Serre, F. Millange, J. Dutour, S. Surble, I. Margiolaki, A chromium terephthalate-based solid with unusually large pore volumes and surface area, Science, 309 (2005) 2040-2042.

[15] A. Celeste, A. Paolone, J.P. Itie, F. Borondics, B. Joseph, O. Grad, G. Blanita, C. Zlotea, F. Capitani, Mesoporous Metal-Organic Framework MIL-101 at High Pressure, J. Am. Chem. Soc. 142 (2020) 15012-15019.

[16] T.K. Vo, D.C. Hau, V.C. Nguyen, D.T. Quang, J. Kim, Double-solvent-assisted synthesis of bimetallic CuFe-incorporated MIL-101 (Cr) for improved CO-adsorption performance and oxygen-resistant stability, Appl. Surf. Sci. 546 (2021) 149087.

[17] Y. Mao, H. Qi, G. Ye, L. Han, W. Zhou, W. Xu, Y.Y. Sun, Green and time-saving synthesis of MIL-100(Cr) and its catalytic performance, Microporous Mesoporous Mater. 274 (2019) 70-75.

[18] Y.K. Seo, J.W. Yoon, J.S. Lee, U.H. Lee, Y.K. Hwang, C.H. Jun, P. Horcajada, C. Serre, J.S. Chang, Large scale fluorine-free synthesis of hierarchically porous iron(III) trimesate MIL-100(Fe) with a zeolite MTN topology, Microporous Mesoporous Mater. 157 (2012) 137-145.

Summary

7

Radionuclides are essential in nuclear medicine and therefore new and improved production methods continue to play an important role in ensuring sustainable availability. This thesis focuses on the production of two radionuclides (^{99m}Tc and ^{51}Cr) using metal-organic frameworks (MOFs). MOFs are novel porous materials and their potential to be utilized in radionuclide production has been explored for the first time in this thesis. Chapter 1 gives a general introduction to the current production of ^{99m}Tc and ^{51}Cr, and emphasizes the role that metal-organic frameworks can play based on their attractive properties.

In chapter 2, UiO-66 (Zr) and its derivatives were prepared and their molybdenum adsorption performance at different concentrations was studied. The maximum molybdenum adsorption capacity of UiO-66 (Zr) that could be reached was 335 mg/g. The interaction between adsorbents and molybdenum species was investigated by FT-IR, XPS and DFT. The results demonstrated that the molybdenum adsorption performance was influenced by the combination of Zr-O-Mo coordination, π-anions and hydrogen bonding. The Form-UiO-66 was selected as adsorbents for the preparation of ^{99}Mo/^{99m}Tc generator. When a molybdenum concentration of 10 mg/mL was applied, the practical adsorption capacity of 145 mg/g could be achieved and 60–70% separation efficiency of ^{99m}Tc could be obtained without Zr breakthrough, but showing higher ^{99}Mo breakthrough compared with that of the commercial alumina columns currently used.

Based on the results of chapter 2, it was suspected that the diffusion of molybdenum species with large sizes could be restricted by the micropores of UiO-66, resulting in limited adsorption capacity. In Chapter 3, in search of higher molybdenum adsorption capacity, two mesoporous porphyrin metal-organic frameworks (PCN-222 and PCN-224) were synthesized and their molybdenum adsorption performance was evaluated at different molybdenum concentrations and pH. The maximum adsorption capacity of PCN-222 and PCN-224 was 525 mg/g and 455 mg/g, respectively. The results demonstrated that MOFs with high surface area and mesoporous structure could prompt molybdenum adsorption capacity by electrostatic attraction, coordination and hydrogen bonds. The separation performance of ^{99}Mo/^{99m}Tc generator fabricated with PCN-222 was tested using saline solutions having different pH. 56% elution yield of ^{99m}Tc without zirconium breakthrough could be achieved, but still with relatively high ^{99}Mo breakthrough ~2%.

The results of chapter 3 showed that the molybdenum adsorption capacity of the prepared MOFs was improved a lot, but the elution efficiency of ^{99m}Tc from the fabricated generator was not ideal. To improve the elution efficiency, UiO-66 (Ce) as an adsorbent for ^{99}Mo/^{99m}Tc generator was evaluated in Chapter 4. The results showed that this adsorbent exhibited excellent radiation stability and the maximum molybdenum adsorption capacity of 475 mg/g could be obtained at pH 3. Then UiO-66 (Ce) was applied to fabricate a ^{99}Mo/^{99m}Tc generator that was eluted daily for two weeks. 92±3% of ^{99m}Tc elution yield could be obtained with negligible cerium breakthrough, showing that UiO-66 (Ce) as adsorbent for ^{99}Mo/^{99m}Tc generators has great potential to achieve eventual practical application.

In chapter 1, we have set the goals of this research and achieved them to a large extent:

✓ High molybdenum capacity adsorbents with excellent ^{99m}Tc elution performance were developed.

✓ Interaction between the molybdenum oxyanions and MOFs was uncovered.

✓ A radionuclide generator based on the best adsorbent (UiO-66 (Ce)) found during this research was designed and its performance can fulfill the European Pharmacopeia standards but requires further reduction of ^{99}Mo breakthrough.

Based on the results of Chapters 2, 3 and 4, we attempted to provide valuable insight into selecting new MOFs to serve as adsorbents in ^{99}Mo/^{99m}Tc generator. (1) In general, the selected MOFs should have excellent chemical and radiation stability. (2) The selected MOFs should have high IEPs. (3) The selected MOFs should have high surface area and large pore volume, which can promote molybdenum adsorption, achieving a high adsorption capacity (Fig. 7.1). (4) The selected MOFs containing defects, which can generate hydroxyl groups, are favorable for the development of adsorbents with high adsorption capacity. In addition, for the practical application and commercial availability using ^{99}Mo with low specific activity, the high elution efficiency (>80%) and low Mo breakthrough (<0.1%) must be achieved. It was shown that ^{99m}Tc elution efficiency of UiO-66 (Zr) and UiO-66 (Ce) of around 70% and 92%, respectively could be achieved. However, the PCN MOFs displayed relatively lower ^{99m}Tc elution efficiency, which could be caused by the pH value of the saline solution used for the elution. When the pH<IEP, some available adsorption sites can be generated after removing the loosely adsorbed Mo species and then the decayed ^{99m}Tc ions are anchored on those adsorption sites, causing the observed low elution efficiency. When the pH>IEP, the

weakly adsorbed Mo species by electrostatic attraction can be washed out and the produced decayed ^{99m}Tc will not be trapped by those available adsorption sites, leading to higher separation efficiency. Therefore, elution at the right pH is considered an important factor. Overall, to utilize the ^{99}Mo with low specific activity, more new adsorbents can be developed by employing MOFs-based material possessing high surface area, big pore volume and specified adsorption selectivity. In the future, more research should be carried out to achieve a perfect adsorbent to prepare a ^{99}Mo/^{99m}Tc generator, so that it can fulfill the European Pharmacopeia standards and be successfully utilized using low specific activity ^{99}Mo.
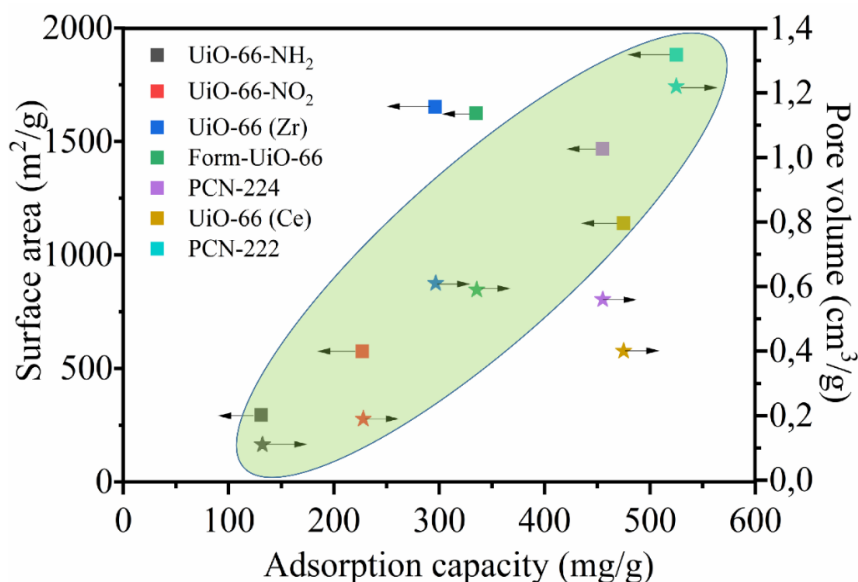

Fig. 7.1. Summary of molybdenum adsorption capacity of reported MOFs in this thesis as the function of surface area and pore volume.

In Chapter 5, the radiation resistance of chromium-based MOFs was studied which is essential to apply MOFs for the production of ^{51}Cr (Chapter 6). Therefore, MIL-100 (Cr) and MIL-101 (Cr) were irradiated using gamma rays at doses ranging from 0 Gy to 5 MGy. Meanwhile, the radiation stability of MIL-100 (Fe) and AlFu MOFs was also investigated by performing a systematic study so that we could explain how the structure of the MOFs can affect the radiation stability of the MOFs. The results showed that MIL-100 (Fe) and MIL-100 (Cr) exhibited outstanding radiation stability when exposed to radiation of high doses (5 MGy). MIL-101 (Cr) showed good radiation stability after exposure to gamma doses within a range of 0~4 MGy. The structure of AlFu MOFs suffered severe damage after receiving 2

MGy gamma dose. Structural analysis showed that the linker aromaticity plays a key role in the radiation stability of MOFs. Based on our results, it seems that the radiation stability could be enhanced for MOFs with high linker connectivity and good crystallinity. This work provides guidance to predict the radiation stability of other MOFs so that they can be utilized in various new nuclear-related applications.

MIL-100 (Cr) and MIL-101 (Cr) were then selected as radiation targets for the production of ^{51}Cr. ^{51}Cr was produced by neutron activation and separated by the solid-liquid method based on the Szilard-Chalmers effect. For the irradiated MIL-100 (Cr), the separation results showed that a high enrichment factor (~564) of ^{51}Cr could be obtained using EDTA (1 mM) at pH 1 after 1 h extraction. For the irradiated MIL-101 (Cr), a high enrichment factor (1132) could be acquired using EDTA. However, considering the practical application in the clinic, higher specific activity of ^{51}Cr (1850 GBq/g) should be produced. Therefore, longer irradiation will be carried out to increase the specific activity of produced ^{51}Cr in the future.

In summary, this thesis explores the potential application of MOFs in the production of radionuclides. It is proved that MOFs as molybdenum adsorbents showed great potential in ^{99}Mo/^{99m}Tc generator, achieving a high separation efficiency and low chemical impurity. A high enrichment factor for ^{51}Cr production could be obtained. Meanwhile, the structural factors of MOFs, including aromaticity of linkers, connections nodes, density and photon cross sections of metals, determined their radiation stability together. Based on the research results in this thesis, some fundamental guidance has been proposed to select MOFs, which could be applied for adsorption and separation, and production of other radionuclides in the future.

Samenvatting

Radionuclide zijn essentieel voor nucleaire geneeskunde en daarom blijven nieuwe en verbeterde productiemethodes een belangrijke rol spelen bij het waarborgen van duurzame beschikbaarheid. Deze thesis focust op de productie van twee radionuclide (^{99m}Tc en ^{51}Cr) met behulp van metal-organic frameworks (MOFs). MOFs zijn innovatieve poreuze materialen en hun potentieel om te worden gebruikt bij de productie van radionucliden is voor het eerst onderzocht in deze thesis. Hoofdstuk 1 geeft een algemene introductie over de huidige productie van ^{99m}Tc en ^{51}Cr, en benadrukt de rol die metal-organic frameworks kunnen spelen gebaseerd op hun aantrekkelijke eigenschappen.

In hoofdstuk 2, UiO-66 (Zr) en zijn derivaten waren voorbereid en hun molybdenum adsorptieprestaties bij verschillende concentraties zijn onderzocht. De maximale molybdenum adsorptie capaciteit van UiO-66 (Zr) dat behaald kon worden was 335 mg/g. De interactie tussen de adsorbentia en molybdeen soorten zijn onderzocht door FT-IR, XPS en DFT. De resultaten tonen aan dat de molybdenum adsorptieprestatie beïnvloed was door de combinatie van Zr-O-Mo coördinatie, π-anionen en waterstofbruggen. De Form-UiO-66 was geselecteerd als adsorbentia voor de voorbereiding van de ^{99}Mo/^{99m}Tc generator. Toen een molybdenum concentratie van 10 mg/ml was toegepast, kon de praktische absorptie capaciteit van 145 mg/g worden behaald en kon 60–70% scheidingsefficiëntie van ^{99m}Tc verkregen worden zonder Zr doorbraak, maar met een hogere ^{99}Mo doorbraak in vergelijking met dat van commerciële aluminium kolommen die momenteel gebruikt worden.

Op basis van de resultaten van hoofdstuk 2 werd vermoed dat de diffusie van molybdenum soorten met grote afmetingen beperkt zouden kunnen worden door de microporiën van UiO-66, resulterend in gelimiteerde adsorptiecapaciteit. In hoofdstuk 3, in zoektocht naar hogere molybdenum adsorptie capaciteiten, twee mesoporeuze porfyrine metal-organic frameworks (PCN-222 en PCN-224) werden gesynthetiseerd en hun molybdenum adsorptieprestaties werden geëvalueerd bij verschillende molybdenum concentraties en pH. De maximale adsorptie capaciteit van PCN-222 en PCN-224 waren respectievelijk 525 mg/g en 455 mg/g. De resultaten tonen aan dat MOF's met een groot oppervlak en mesoporeuze structuur molybdeenadsorptiecapaciteit kunnen stimuleren door elektrostatische aantrekking, coördinatie en waterstofbruggen. The scheidingsprestatie van de ^{99}Mo/^{99m}Tc generator

vervaardigd met PCN-222 is getest met zoutoplossingen met verschillende pH. 56% elutie-opbrengst van ^{99m}Tc zonder zirkonium doorbraak kon behaald worden, maar nog steeds met relatieve hoge ^{99}Mo doorbraak ~2%.

De resultaten van hoofdstuk 3 laten zien dat de molybdenum adsorptie capaciteit van de bereide MOF's sterk verbeterd is, maar de elutie-efficiëntie van ^{99m}Tc van de gefrabiceerde generator niet ideaal is. Om de elutie-efficiëntie te verbeteren, werd UiO-66 (Ce) als adsorbens voor de ^{99}Mo/^{99m}Tc generator geëvalueerd in hoofdstuk 4. De resultaten toonden aan dat dit adsorbens een uitstekende stralingsstabiliteit vertoonde en dat de maximale molybdeenadsorptiecapaciteit van 475 mg/g kon worden verkregen bij pH 3. Vervolgens werd UiO-66 (Ce) aangebracht voor de fabricatie van de ^{99}Mo/^{99m}Tc generator die gedurende twee weken dagelijks werd geëlueerd. 92±3% van ^{99m}Tc elutie-opbrengst kon behaald worden met verwaarloosbare cerium doorbraak, aantonend dat UiO-66 (Ce) als adsorbens voor ^{99}Mo/^{99m}Tc generators groot potentieel vertoond om uiteindelijke praktische toepassing te bereiken

In hoofdstuk 1 hebben we de doelen van dit onderzoek vastgesteld en deze voor een groot deel bereikt:

✓ Hoge molybdeen capaciteit adsorbens met excellente ^{99m}Tc elutie prestaties zijn ontwikkeld.

✓ Interactie tussen molybdeenoxyanionen en MOF's zijn ontdekt.

✓ Een radionuclide generator gebaseerd op de beste adsorbens (UiO-66 (Ce)) gevonden tijdens dit onderzoek was ontworpen en de prestaties daarvan kunnen voldoen aan de normen van de European Pharmacopeia maar vereisen een verdere vermindering van de doorbraak van ^{99}Mo.

Op basis van de resultaten van hoofdstukken 2,3 en 4 hebben we geprobeerd om waardevolle inzicht te geven in het selecteren van nieuwe MOF's om te dien als adsorbentia in de ^{99}Mo/^{99m}Tc generator. (1) In het algemeen moeten de geselecteerde MOF's uitstekende chemische stabiliteit en stralingsstabiliteit hebben. (2) De geselecteerd MOF's moeten hoge IEP's hebben. (3) De geselecteerde MOF's moeten een groot oppervlakte en een groot porievolume hebben, wat de adsorptie van molybdeen kan bevorderen, waardoor een hoge adsorptiecapaciteit wordt bereikt (Fig. 7.1). (4) De geselecteerde MOF's die defecten bevatten, die hydroxyl groepen kunnen generen, zijn gunstig voor de ontwikkeling van adsorbentia met hoge adsorptie capaciteit. Bovendien voor de praktische applicatie en

commerciële beschikbaarheid gebruik maken van ^{99}Mo met lage specifieke activiteit, moet hoge elutie-efficiëntie (>80%) en lage Mo doorbraak (<0.1%) bereikt worden. Er is aangetoond dat ^{99m}Tc elutie-efficiëntie voor UiO-66 (Zr) en UiO-66 (Ce) rond de 70% en 92% respectievelijk bereikt kan worden. Echter de PCN MOF's vertoonden een relatief lagere ^{99m}Tc elutie-efficiëntie, wat veroorzaakt zou kunnen worden door de pH-waarde van de zoutoplossing die gebruikt is voor de elutie. Wanneer de pH<IEP, kunnen sommige van de beschikbare adsorptie plaatsen gegenereerd worden na het verwijderen van zwak geabsorbeerde Mo soorten en dan zijn de vervallen ^{99m}Tc ionen verankerd op die absorptie plaatsen, zorgend voor de laag waargenomen elutie-efficiëntie. Wanneer de pH>IEP, kan de zwak geabsorbeerde Mo soorten door elektrostatische aantrekking worden uitgewassen en zal de geproduceerde vervallen ^{99m}Tc niet gevangen worden bij die beschikbare adsorptie plaatsen, zorgend voor een hogere scheidingsefficiëntie. Daarom wordt elutie bij de juiste pH als een belangrijke factor beschouwd. Over het algemeen kunnen, om gebruikt te kunnen maken van ^{99}Mo met lage specifieke activiteit, meer nieuwe adsorbentia ontwikkeld worden door gebruikt te maken van op MOF's gebaseerde materialen met een groot oppervlak, een groot porie volume en een gespecificeerd adsorptieselectiviteit. In de toekomst moet meer onderzoek gedaan worden om een perfecte adsorbens te verkrijgen voor het voorbereiden van een ^{99}Mo/^{99m}Tc generator, zodat deze kan voldoen aan de European Pharmacopeia normen en succesvol gebruikt kan worden met laag specifieke activiteit ^{99}Mo.

In hoofdstuk 5 is de stralingsbestendigheid van de op chroom gebaseerde MOF's onderzocht, wat essentieel is voor het toepassen van MOF's voor de productie van ^{51}Cr (Hoofdstuk 6). Daarom zijn MIL-100 (Cr) en MIL-101 (Cr) bestraald met gammastraling in dosis variërend van 0 Gy tot 5 MGy. Ondertussen zijn ook de stralingsstabiliteit van MIL-100 (Fe) en AlFu MOF's onderzocht door het uitvoeren van een systematische studie zodat we zouden kunnen verklaren hoe de structuur van de MOF invloed kan hebben op de stralingsstabiliteit van de MOF's. De resultaten toonden aan dat MIL-100 (Fe) en MIL-100 (Cr) uitstekende stralingsstabiliteit vertoonden bij blootstelling aan hoge dosis (5 MGy). MIL-101 (Cr) vertoonde goede stralingsstabiliteit na blootstelling aan gammadoses binnen een bereik van 0~4 MGy. De structuur van de AlFu MOF's liep ernstige schade op na ontvangst van 2 MGy gamma dosis. Structurele analyse toonde aan dat de aromatiteit van de linker een sleutelrol speelt in de stralingsstabiliteit van de MOF's. Op basis van onze resultaten lijkt het erop dat stralingsstabiliteit zou kunnen worden verbeterd voor MOF's met hoge linkerconnectiviteit

en goede kristalliniteit. Dit werk biedt richtlijnen voor het voorspellen van stralingsstabiliteit van andere MOF's, zodat ze gebruikt kunnen worden in verscheidene nieuwe nucleair gerelateerde toepassingen.
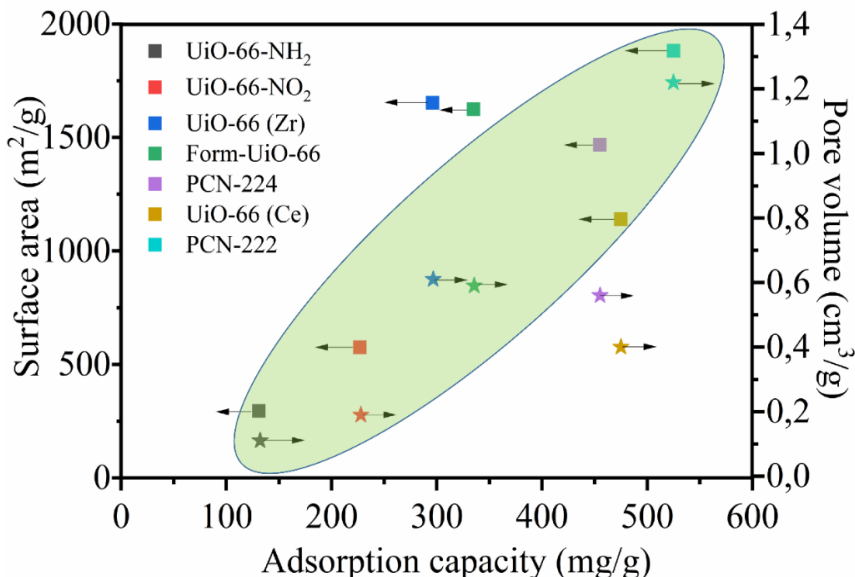

Fig. 7.1. Samenvatting van de molybdeen adsorptie capaciteit van gerapporteerde MOF's in deze thesis als de functie van oppervlakte en porievolume.

MIL-100 (Cr) en MIL-101 (Cr) werden vervolgens geselecteerd als stralingsdoelen voor de productie van ^{51}Cr. ^{51}Cr werd geproduceerd door neutron n activering en gescheiden door de solid-liquid methode gebaseerd op het Szilard-Chalmers effect. Voor de bestraalde MIL-100 (Cr) toonden de scheidingsresultaten aan dat een hoge verrijkingsfactor (~564) van ^{51}Cr behaald kon worden gebruik makend van EDTA (1 mM) bij pH 1 na 1 uur extractie. Voor het bestraalde MIL-101 (Cr) kon een hoge verrijkingsfactor (1132) verkregen worden met EDTA. Echter zou gezien de praktische toepassing in de kliniek een hogere specifieke activiteit van ^{51}Cr (1850 GBq/g) geproduceerd moeten worden. Daarom zullen langere bestralingen uitgevoerd worden voor het verhogen van de specifieke activiteit van ^{51}Cr in de toekomst.

Samenvattend onderzoekt dit proefschrift de mogelijke toepassing van MOF's bij de productie van radionucliden. Het is bewezen dat MOF's als molybdeenadsorptiemiddelen een groot potentieel vertoonden in de ^{99}Mo/^{99m}Tc generator, waarbij een hoge scheidingsefficiëntie en een lage chemische onzuiverheid werden bereikt. Een hoge

verrijkingsfactor voor ^{51}Cr-productie kon worden verkregen. Ondertussen bepaalden de structurele factoren van MOF's, waaronder aromaticiteit van linkers, verbindingsknooppunten, dichtheid en fotondoorsneden van metalen, hun stralingsstabiliteit samen. Op basis van de onderzoeksresultaten in dit proefschrift zijn er fundamentele richtlijnen voorgesteld voor het selecteren van MOF's, die in de toekomst kunnen worden toegepast voor adsorptie en scheiding, en de productie van andere radionucliden.

List of publications

Publications

1. **<u>C. Ma</u>**, H. T. Wolterbeek, A. Denkova, P. S. Crespo, Effects of high gamma doses on the structural stability of metal-organic frameworks, Langmuir**, 2022**, 38 (29), 8928-8933.

2. **<u>C. Ma</u>**, H. T. Wolterbeek, A. Denkova, P. S. Crespo, A cerium-based metal-organic framework as adsorbent for the ^{99}Mo/^{99m}Tc generator, Sep. Purif. Technol., **2022**, 295, 121218.

3. **<u>C. Ma</u>**, A. Vasileiadis, H. T. Wolterbeek, A. Denkova, P. S. Crespo, Adsorption of molybdenum on Zr-based MOFs for potential application in the ^{99}Mo/^{99m}Tc generator, Appl. Surf. Sci., **2022**, 572, 151340.

4. **<u>C. Ma</u>**, H. T. Wolterbeek, A. Denkova, P. S. Crespo, Porphyrinic metal-organic frameworks as molybdenum adsorbents for ^{99}Mo/^{99m}Tc generator, Inorg. Chem. Front. **2022** (under review).

5. **<u>C. Ma</u>**, H. T. Wolterbeek, A. Denkova, P. S. Crespo, Production of high specific activity ^{51}Cr by chromium-based metal-organic frameworks and Szilard-Chalmers effect (in preparation).

Oral presentations

<u>C. Ma</u>, H. T. Wolterbeek, A. Denkova, P. S. Crespo, A cerium-based metal-organic framework as adsorbent for the ^{99}Mo/^{99m}Tc generator, Prague, Czech Republic. 16-20, May 2022, RadChem conference.

Posters

1. <u>**C. Ma**</u>, H. T. Wolterbeek, A. Denkova, P. S. Crespo, A cerium-based metal-organic framework as adsorbent for the ^{99}Mo/^{99m}Tc generator, Groningen, the Netherlands, June 24, 2022, 30th NKRV Workshop.

2. <u>**C. Ma**</u>, H. T. Wolterbeek, A. Denkova, P. S. Crespo, Production of high specific activity ^{51}Cr by chromium-based metal-organic frameworks and Szilard-Chalmers effect. Prague, Czech Republic. May 16-20, 2022, RadChem conference.

3. <u>**C. Ma**</u>, H. T. Wolterbeek, A. Denkova, P. S. Crespo, Zr-based MOFs as adsorbents for the ^{99}Mo/^{99m}Tc generator. the Netherlands, December 7-8, 2021, Chemistry as Innovating Science (online).

4. <u>**C. Ma**</u>, H. T. Wolterbeek, A. Denkova, P. S. Crespo, Adsorption of molybdenum on Zr-based MOFs for potential application in ^{99}Mo/^{99m}Tc generator. France, March17-18, 2021, 1st International Workshop on Radiobiology of Molecular Radiotherapy (online).

Acknowledgments

Time is flying. I have an unforgettable period and friendly working environment in the past four years at Reactor Institute of Delft. Therefore, I would like to take this opportunity to express my gratitude to those people who have helped and supported me during my Ph.D.

First and foremost, I would like to express my deepest appreciation to my daily supervisor, Pablo Serra Crespo and my promoter, Antonia Denkova and Hurbert T. Wolterbeek. Thank you for giving me this opportunity to study in this warm group, although I do not have a background in nuclear chemistry. Dear Antonia, very special thanks for your careful guidance and assistance during my Ph.D. journey. When I had a meeting with you in my first year, I worried that I did not have much progress or good results to present. You always show an empathetic and understanding attitude toward me. When I sent you my paper draft and other documents, you always reply me quickly and work untill late to send me your comments. When I faced obstacles during research, you always encourage me and help me find a solution to solve problems. There are so many things and warm moments that I want to appreciate you from the bottom of my heart. Without you, I cannot finish my dissertation. Dear Pablo, I think I am lucky to meet you. I am very grateful to you for providing this research topic and for supporting me over the past four years. I still remember that you wrote a summary of the key points we discussed for me after our first meeting so that I could better understand this research. I never forget that because it made me feel you are empathetic and I very appreciate your consideration at that time. In the following several years, you always provide patient guidance and deep insights when my experiments failed or we need to reply to reviewer comments. I am glad to work with you. Dear Bert, you can always find the crux of my research and provide unique insights during our meeting. You taught me to think differently and catch the salient issues. I hope I could be a researcher like you in the future. In addition, I would like to thank Kristina Djanashvili. Thanks for your suggestions and knowledge about TUD-1 preparation and NMR measurement. I would like to express my thanks to Robin de Kruijff for your nice suggestions during our small group meeting.

Next, I would like to thank all technicians who gave me support and help during my research. Baukje, thank you very much for training me on how to use ICP and irradiating samples. You always have a kind attitude when I disturb you frequently. I learned a lot of experience from

you. Astrid, thanks for helping me solve problems when SEM had an issue and INAA measurement. You still can find time to help me irradiate samples even when you were very busy. I appreciate your attitude and support for me. Folkert, thanks for your help about how to use Wallac and your explanation when I had questions to ask. Anouk, thanks for your help in arranging everything. You are a very awesome lady and can provide very detailed information to help me solve problems. Eline, thanks for your help in the Lab and your support in my research. Mehmet, thank you so much for help us seal glass tubes and irradiate samples. Furthermore, I appreciate Willy Rook for your help with the N_2 adsorption measurements. I also appreciate Bart van der Linden for the help with the TGA measurement. I gratefully acknowledge Bart Boshuizen for the XPS measurement. I also want to express my thanks to Henk for training me on how to use the Co-60 source. I also want to thank all staff in SBD for your help and tolerance when I had contamination in the Lab, including Henk, Josette, Coos, Radboud, Erwin and Misja. Thanks a lot for all your help.

Then, I would like to thank all my colleagues from the Applied radiation and isotopes section. Huanhuan, thank you for introducing me to this great group and discussing the problems I faced in my research and life. Retna, thank you help me measure zeta potential and inviting me to celebrate your birthday. Rogier, thank you for teaching me Dutch and inviting me to have dinner at your home. I never forget that I have a friendly and enthusiastic Dutch friend. Wish you everything the best in the future. Runze, thank you for spending those years with me. We help each other and share happy times. There are so many unforgettable moments and I wish you success in the Netherlands and see you in China in the future. Robin, thank you for the dinner party at your home and for sharing happy moments. Alexandra and Svenja, thanks for your valuable suggestions in the group meeting. Hu, Juncheng, Bing and Qi, thank you for our fantastic dinner event. We have developed a deep friendship although we have known each other for a short time. Furthermore, I also want to thank some other people in our group, including Jan Willem, Adrie, Marc, Adarsh, Wout, Anthonie, I am glad working with you.

In addition, I want to thank Guotai and Chuncheng in the 58 building who help me do material characterization during my research. I want to thank all my Chinese friends in the reactor, Liu Ming, Li Zhaolong, Huang Bowei, Zhao Chenglong, You Xinmin, Fu Yifan, Wang Chao, Zhang Fengqi, Ziying, Shen Qi, Ha Mutu, Hanggai, Li Yueer, Zhang Shengnan. Thanks for lunch and dinner time with you. It is my pleasure to become friends with you. To all of my

basketball team friends, Yan Yunpeng, Yan Rui, Fu Mingyan, Liu Hanqing, Zhang Jian, Cao Liqi, Zhu Baozhou, Cui Zhen, Peng Zhiqiang, Luo Ding, Zhu jianing, Lu tianqi, dawei and Chen Qianyi. Thank you for playing basketball with me.

I also would like to express my gratitude to my dear friends, Yang Bingquan, Li Longnan, Li Wei, Feng Huayang, Li Yaya, Lang Lengxiao, Zhang Shuo, Sun Yiqun, Wu Miao, Chen Xianfeng, Wu Ziyi. Thanks for your support and help during my Ph.D. life. I hope our friendship lasts forever.

Finally, I want to thank my parents, who support and encourage me at every important stage of my life. You created a good environment for me so that I can pay attention to finish my schoolwork and achieve my goals without too many worries. Ma Yue, my younger brother, thank you for accompanying and taking care of our parents. I wish you success in your academics. I want to express gratitude to my parents-in-law. Without your trust and support, I cannot focus on my research. Thank you for everything you do for us. I want to show my deepest gratitude and love to my wife, Dai Qiaofei. You have been supporting in work and spiritual. Thank you for giving us a lovely baby and taking care of her by yourself. Thanks for your efforts to make me finish the Ph.D. smoothly.

Chao Ma

马 超

Curriculum Vitae

Chao Ma was born on the 3rd of July 1991 in Henan province, China. In 2015, he obtained the bachelor's degree in Material Processing and Control Engineering from the Faculty of Mechanical and Electrical Engineering at the Zhengzhou University of Aeronautics in China. In 2018, he received MSc. degree in Material Science from Zhengzhou University, China. He conducted his Master's thesis "Investigation of Electrical Properties and Temperature Sensing Features of Polymer Derived SiAlCN Ceramics" under the supervision of Prof. dr. Rui Zhang and Prof. dr. Gang Shao.

In October 2018, he started his Ph.D. project at the Delft University of Technology (The Netherlands). He worked in the Applied Radiation and Isotopes section of the Reactor Institute of Delft and was supervised by Dr. Pablo Serra Crespo, Prof. Antonia Denkova and Prof. dr. Bert Wolterbeek. His research focused on the fabrication of a radionuclide generator to produce ^{99m}Tc radionuclide. During his Ph.D. period, he synthesized different metal-organic frameworks as molybdenum adsorbents to separate ^{99m}Tc, achieving a performance that can fulfill the European Pharmacopeia standards.